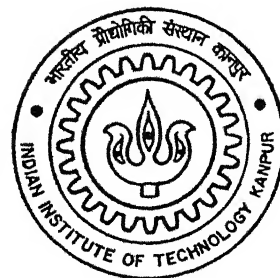# Studies on the Nanocrystalline 80Ni-15Fe-5Co Prepared via A Powder Metallurgy Route Involving Mechanical Alloying and Explosive Compaction

By

## Sanjay Kumar Vajpai

**DEPARTMENT OF MATERIALS AND METALLURGICAL ENGINEERING**

## INDIAN INSTITUTE OF TECHNOLOGY KANPUR

**AUGUST, 2003**

# Studies on the Nanocrystalline 80Ni-15Fe-5Co Prepared via A Powder Metallurgy Route Involving Mechanical Alloying and Explosive Compaction

*A Thesis Submitted*

In Partial Fulfillment of the Requirements

For the Degree of

**MASTER OF TECHNOLOGY**
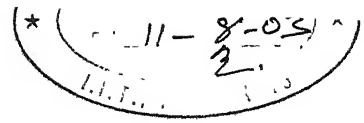
By

**Sanjay Kumar Vajpai**

**(Roll No. Y110615)**

*to the*

**DEPARTMENT OF MATERIALS AND METALLURGICAL ENGINEERING**

**INDIAN INSTITUTE OF TECHNOLOGY, KANPUR**

# CERTIFICATE

This is to certify that the thesis titled **"Studies on the Nanocrystalline 80Ni-15Fe-5Co Prepared via A Powder Metallurgy Route Involving Mechanical Alloying and Explosive Compaction"** by Sanjay Kumar Vajpai (Roll Number Y110615) has been carried out under my supervision and to the best of my knowledge this work has not been submitted elsewhere for a degree.

Dr. R.K. Dube
Professor

Department of Materials and Metallurgical Engineering
Indian Institute of Technology
Kanpur – 208016, INDIA

Date: August 11, 2003

# *ABSTRACT*

A mixture of 80 wt% carbonyl Nickel powder, 15 wt% electrolytic Iron powder and extra fine powder grade Cobalt powder was milled in a Planetary Ball Mill for different periods of time ranging from 15 min.-170 hr in order to prepare nanocrystalline 80Ni-15Fe-5Co powder. The crystallite size of the resulting powder was studied using XRD line broadening technique. It has been observed that the crystallite size decreases with the milling time. The crystallite size decreases very rapidly between 15 min-12 hr milling time. Beyond 12 hr of milling time, the crystallite size remains unchanged. The crystallite size of the 80Ni-15Fe-5Co powder, milled for 125 hr, was found to be 9 nm. TEM analysis of the milled powder shows that the crystallite size is in the range between 10-50 nm. TEM analysis also indicates the dynamic recrystallization during milling operation.

The low temperature grain growth kinetics conducted at $500^0C$ for 125 hr milled MA nanocrystalline 80Ni-15Fe-5Co powder shows that the grain growth occurs very rapidly in the first 10 minutes of isothermal annealing and the crystallite size increases to 40 nm after 10 minutes of annealing. Beyond this point, the grain growth becomes sluggish and a level off trend has been observed. It has been shown that mechanically alloyed nanocrystalline 80Ni-15Fe-5Co powder can be compacted by explosive compaction technique without any significant grain growth. The density achieved after the explosive compaction in the present study was about 90% of the theoretical density.

The final mean grain size of the explosive compacted MA nanocrystalline 80Ni-15Fe-5Co was found to be 15 nm by XRD line broadening technique. The bright field TEM images show that the crystallite size is in the range of 10-50 nm, which is in agreement with the results found by the XRD technique. The magnetic properties of the explosive compacted MA nanocrystalline 80Ni-15Fe-5Co were determined using Vibrating Sample Magnetometer (VSM). The explosive compacted MA nanocrystalline 80Ni-15Fe-5Co shows improved soft magnetic properties such as high Curie temperature, high saturation magnetization, high initial permeability, low coercivity, low remanence and low core loss which make it an excellent soft magnetic material.

# *Acknowledgements*

Sanjay Kumar Vajpai

# TABLE OF CONTENTS

# CHAPTER 1

## 1. NANOSTRUCTURED MATERIALS

### 1.1 INTRODUCTION

In recent years, the nano-technology has been identified as a new wave towards millennium innovations in the materials science and engineering. With reduction of a characteristic length such as the grain size or the cluster or molecular size, the normal properties of materials were reported to be drastically changed [Nihara 1999, Wakai et al 1986]. Nano-structured materials can be represented as "a broad class of materials, with microstructures modulated in zero to three dimensions on length scales less than 100nm" or in other words "materials with atoms arranged in nano sized clusters, which become the constituent grain or building blocks of the materials". The emerging fields of nanoscale science, engineering and technology – the ability to work at the molecular level, atom by atom, to create large structures with fundamentally new properties and functions – are leading to unprecedented understanding and control over the basic building blocks and properties of natural and man made things.

Scientists have opened a broad net of discoveries that does not leave any major research area untouched in physical, biological, and engineering sciences. The importance and potential of nanotechnology is quite visible in the words of "Roco" as he predicts "As the 21st century unfolds, nanotechnology's impact on the health, wealth, and security of the world's people is expected to be at least as significant as the combined influences in this century of antibiotics, integrated circuits, and other advanced materials" [Roco 2002]. In 2001, virtually all developed countries have initiated programs in this area or had national programs in advanced planning [Roco 2001]. As shown in Table 1.1, the world wide nanotechnology R&D investment reported by government organizations including Japan, Western Europe, and the USA has increased approximately five times in the last 5 years, between 1997 & 2002 [Roco et al 2003].

**Table 1.1: Estimated Government nanotechnology R&D expenditure (all in $ millions/year)**

| Area | Year | | | | | | |
|---|---|---|---|---|---|---|---|
| | 1997 | 1998 | 1999 | 2000 | 2001 | 2002 | 2003 |
| | Amount in million dollars ($) per year | | | | | | |
| W. Europe | 126 | 151 | 179 | 200 | 225 | 400 | |
| Japan | 120 | 135 | 157 | 245 | 465 | 750 | -------- |
| U.S.A.* | 116 | 190 | 255 | 270 | 422 | 604 | 770 |
| Others** | 70 | 83 | 96 | 110 | 380 | 520 | ------- |
| Total | 432 | 559 | 687 | 825 | 1502 | 2274 | ------- |
| % of 1997 | 100 | 129 | 159 | 191 | 348 | 526 | -------- |

* A financial year begins in the U.S.A. on October 1st of the previous year, and in most other countries on March 1st or April 1st of the respective year.

** "Others" include Australia, Canada, China, Eastern Europe, FSU, Korea, Singapore, Taiwan, and other countries with nanotechnology R&D.

Source: www.nano.gov

In the coming years, it can be predicted that the convergence of nano-technology with information technology, modern biology, and social sciences will reinvigorate discoveries and innovations in almost all the areas of the economy.

## 1.2 DEFINITIONS AND CLASSIFICATION OF NsM

The basic question, which arises during the discussion, is what nano-structured materials are at all. In what way these materials should be defined? A number of Researchers and Scientists have defined them in different ways. In this section, we will have an overview of these materials including various definitions, their classification and a brief introduction of each of the class/type.

### 1.2.1 Definitions

About nanocrystalline materials, the pioneering Gleiter says,
" Nanocrystalline solids are polycrystals, the crystal size of which is a few (typically 1 to 10) nanometers" [Gleiter 1991].

According to R.W.Siegel,
"Nano phase materials are three dimensionally modulated, synthetic materials with average grain size, phase or other structural domain sizes below 100nm" [Siegel 1993].

At another place Gleiter defined NsM as,
"NsM are solids composed of structural element – mostly crystallites – with a characteristic size (in at least one direction) of a few nanometers" [Gleiter 1995].

The designation "nano powder" is usually used to describe powders with a particle diameter less than 1 micrometer (1000 nm) [Eifert et al 2000]. Some more definitions of NsM are as follows:
(i) According to Lu et al: "Nanostructured Materials have a characteristic length scale of a few (typically 1-10) nanometers" [Yulin and Liaw 2001].

(ii) According to McHenry and Laughlin: "The term nanocrystalline alloy is used to describe those alloys that have majority of grain diameters in the typical range from 1 to 50 nanometers" [McHenry et al 2000].

(ii) According to R.Birringer: "Nanocrystalline Materials are single-phase or multiphase polycrystals, the crystal size of which is of the order of a few (typically 1-10) nanometers, so that about 50 volume % of the material consists of grain or interphase boundaries" [Birringer 1989].

In a recent review, Gleiter has again summarized NsM as,
"NsM are materials with a microstructure, the characteristic length scale of which is on the order of a few (typically 1-10) nanometers" [Gleiter 2000].

On the basis of above information NsM can be defined as follows:
"NsM are single phase or multiphase polycrystals having the crystal size of the order of a few (typically 1-100) nanometers in at least one dimension".

## 1.2.2 Classification on the basis of Dimensionality

Nano-Structured Materials can be classified on the basis of dimensionality (in which length scale is in nanometer) as follows:
(a) Nano particles
(b) Layered or lamellar structure
(c) Filamentary structure
(d) Bulk nano-structured materials

Nano particles are atom clusters and can be considered zero dimensional (0-D) in nature [Siegel 1994]. A layered or lamellar structure is a one dimensional (1-D) nano structure in which the magnitudes of length and width are much greater than the thickness that is only a few nanometers in size. A two dimensional (2-D) nano-structure can be termed as filamentary and in this the length is substantially larger than width or diameters, which

are of the nanometer dimensions [Suryanarayana 1995]. The most common of the nano-structure is basically equiaxed (all the 3-dimensions are in nm size) and are termed nanostructured crystallites or 3-D nanostructures [Suryanarayana and Koch 1999].

The NsM may contain crystalline, quasicrystalline, or amorphous phases and can be metals, ceramics, polymers or composites. If grains are made up of crystals, the material is called nano-crystalline. On the other hand if they are made up of quasicrystalline or amorphous (glassy) phases, they are termed nano-quasi-crystals or nano-glasses [Suryanarayana 1995]. A detailed classification of NsM is shown in Figure 1.1a & 1.1b and Table 1.2.

## 1.3 Parameters Controlling the Properties of NsM

As the properties of solids depend on size, atomic structure and chemical composition, NsM exhibit new properties due to one or several of the following effects:

### 1.3.1: Size Effects:

Size effects result if the characteristic size of the building blocks of the microstructure (e.g. crystallite size, figgure1.2) is reduced to the point where critical length scales of physical phenomena (e.g. the mean free paths of electrons or phonons, a coherency length, a screening length, etc.) become comparable with the characteristic size of the building blocks of the microstructure [Gleiter 1998].

For example, if the thickness of the layers of a superlattice is comparable with the wavelength of the electrons at the fermi edge, discrete energy levels for electrons and holes are formed in quantum wells (Figure 1.3) [Grossard 1979]. Such size effects modifying the mechanical and optical properties are displayed in Figure1.4a and 1.4b [Gleiter 1995].
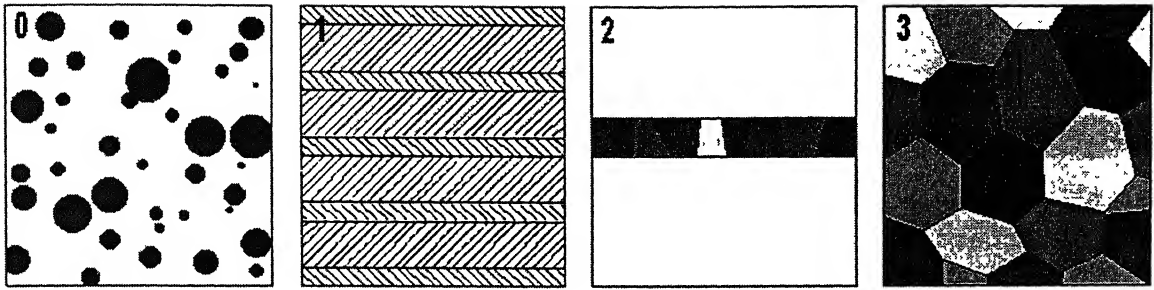
Figure 1.1a    Schematic representation of four types of nanocrystalline materials [Siegel 1994].
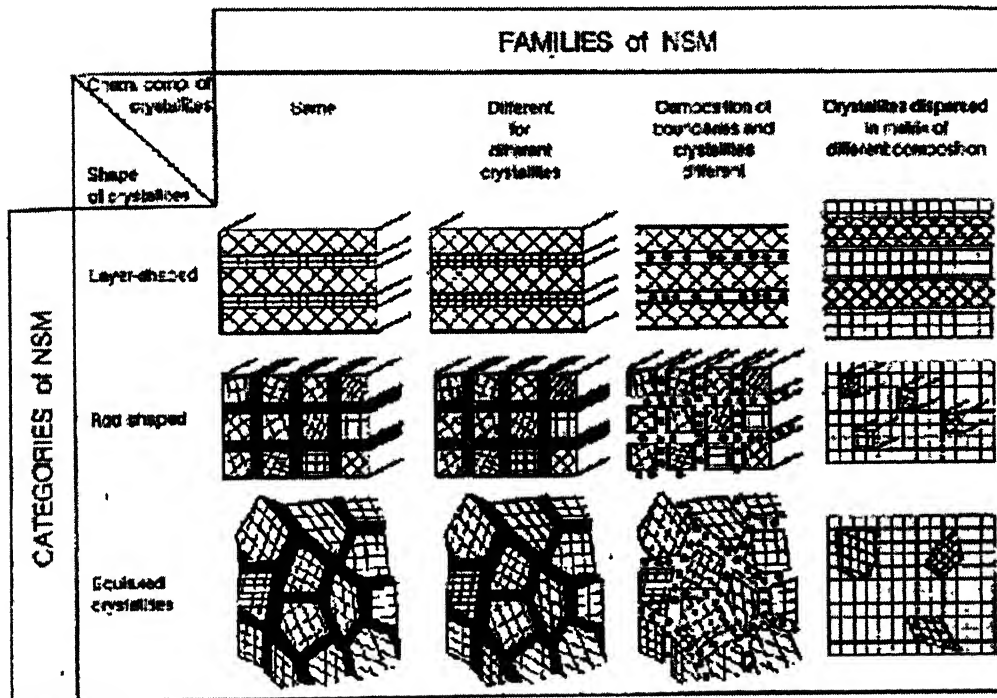


Figure 1.1b Classification scheme for NsM according to their chemical composition and the dimensionality (shape) of the crystallites (structural elements), forming the NsM [Gleiter 2000].

# TABLE 1.2: CLASSIFICATION OF NANOCRYSTALLINE MATERIALS

[Suryanayana and Koch 1999]

| DIMENSIONALITY | DESIGNATION | TYPICAL METHODS OF SYNTHESIS |
|---|---|---|
| Zero-Dimensional (0-D) | Clusters | Sol-Gel method |
| One-Dimensional (1-D) | Layered (lamellar) | Vapor deposition Electro-deposition |
| Two-Dimensional (2-D) | Filamentary | Chemical Vapor deposition |
| Three-Dimensional (3-D) | Crystallites (equiaxed) | Gas condensation Mechanical Alloying |
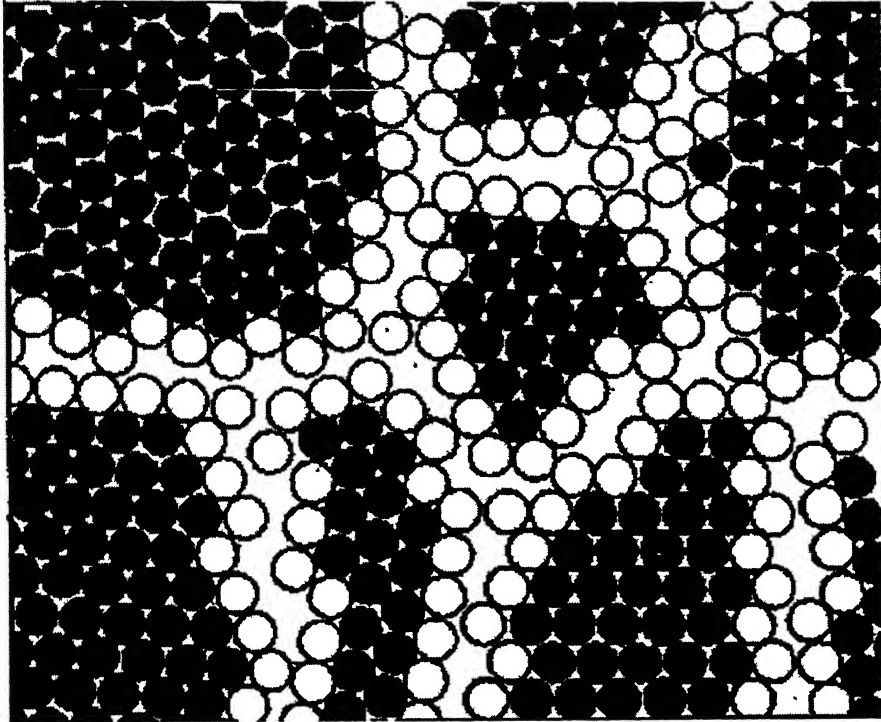
**Figure 1.2 Two-dimensional model of a nanostructured material. The atoms in the centers of the crystals are indicated in black. The ones in the boundary core regions are represented as open circles [Gleiter 1998].**
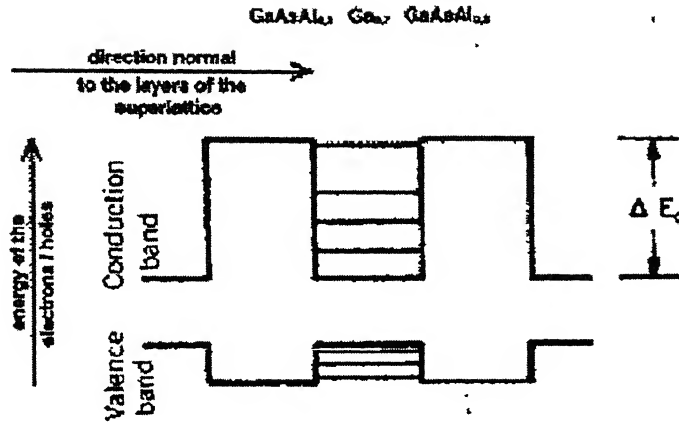
Figure 1.3 Energy-band diagrams for undoped GaAs-Al$_x$Ga$_{1-x}$As superlattices showing conduction and valence-band edges with heterostructure potential wells at x = 0.3, $\Delta E_c \approx$ 300 meV. The horizontal lines represent quantum-well discrete energy levels for electrons and holes confined in the GaAs layers [Grossard 1979].



(a)                                      (b)
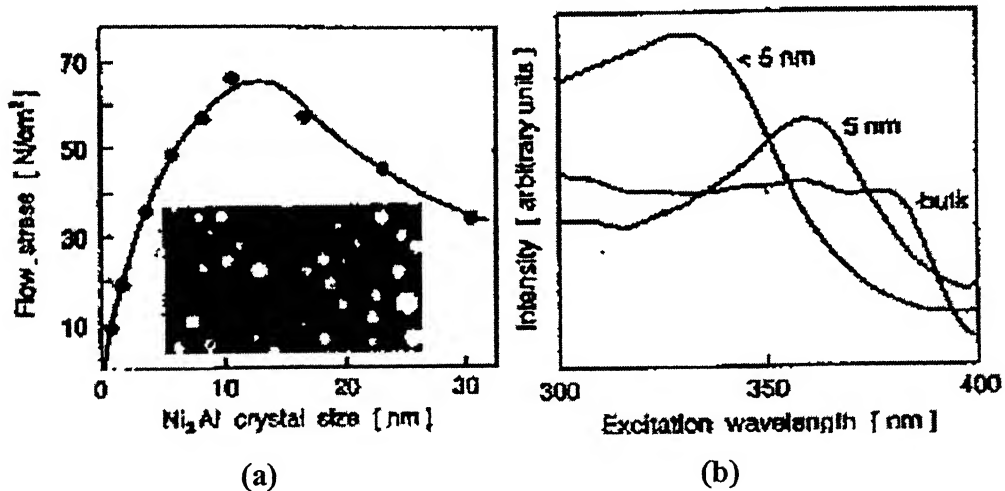
Figure 1.4. (a) Flow stress of Ni at.% Ni alloys as a function of the size of the Ni$_3$Al precipitates. (b) Photoluminescence spectra of nanocrystalline ZnO with different crystal size in comparison with the bulk material. The detection wavelength was 550 nm [Gleiter 1995].

## 1.3.2 Change of the Dimensionality of the System

If an NsM consists of thin needle-shaped or flat, two-dimensional crystallites (Figure 1.1a & 1.1b), only two or one dimension of the building blocks becomes comparable with the length scale of a physical phenomenon. In other words, in these cases the NsM becomes a two or one-dimensional system with respect to this phenomenon [Gleiter 2000].

## 1.3.3 Change of Atomic Structure

Change in the atomic structure results if a high density of incoherent interface (Figure 1.2) or other lattice defects such as dislocations, vacancies etc, are incorporated. The cores of lattice defects represent a constrained state of solid matter differing structurally from (unconstrained) crystals and/or glasses. As a consequence, a solid containing a high density of defect cores differs structurally from a defect-free solid with the same (average) chemical composition [Gleiter 2000].

The boundaries in the Figure 1.2 represent an example of this effect. The misfit between adjacent crystallites changes the atomic structure (e.g. the average atomic density, the nearest-neighbor coordination, etc.) in the boundary region relative to the perfect crystal. At high defect densities the volume fraction of defect cores becomes comparable with the volume fraction of the crystalline region. In fact, this is the case if the crystal diameter becomes comparable with the thickness of the interface, i.e. for crystal sizes on the order of one or a few nanometers, as is the case in NsM.

## 1.3.4 Alloying of Components that are immiscible in the solid or the molten State

Solute atoms (Figure 1.5) with little solubility in the lattice of the crystallites frequently segregate to the boundary cores (e.g. the free energy of the system in several alloys is reduced if large solute atoms segregate to the boundary core). Another type of nanostructured alloys results if the crystallites of an NsM have different chemical compositions. Even if the constituents are immiscible in the crystalline and/or molten

state (e.g. Fe & Ag), the formation of solid solution in the boundary regions of the NsM has been noticed (Figure1.6) [Herr et al 1990].

## 1.4 METHODS OF SYNTHESIS

In recent times, numerous methods have been developed to prepare Nano-structured Materials. Any method capable of producing very fine grain-size polycrystalline materials can be adopted to produce Nano-crystalline materials. The grain size, morphology, and texture can be varied by suitably modifying/controlling the process variables in these methods (Table1.3).

If a phase transformation is involved, e.g. liquid to solid, or vapor to solid, then steps are needed to increase the nucleation rate and to decrease the growth rate during formation of the product phase. We will now describe the different methods of preparing NsM starting from vapor, liquid or solid phases.

### 1.4.1 Inert Gas Condensation

This method consists of evaporating a metal (by resistive heating, radio frequency heating, sputtering, electron beam, laser plasma heating, or ion sputtering) inside a chamber that is evacuated to a very high vaccum of about $10^{-7}$ torr and then backfilled with a low-pressure inert gas, typically a few hundred Pascal of He. The evaporated atoms collide with the gas atoms inside the chamber, lose their kinetic energy, and condense in the form of small, discrete crystals of loose powder.

Convection currents, generated due to the heating of the inert gas by the evaporation source and cooled by the liquid nitrogen-filled collection device (cold finger), carry the condensed fine powders to the collector device, from where they can be stripped off by moving an annular Teflon ring down the length of the tube into a compaction device.

11
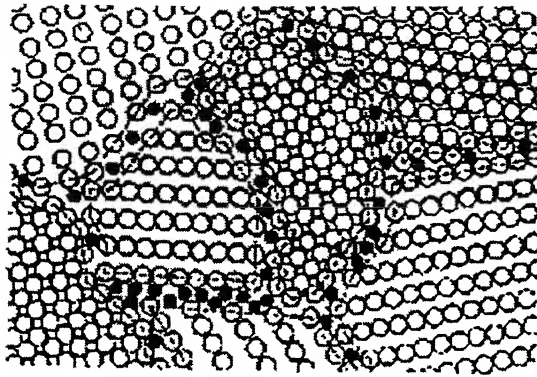
Figure 1.5 Schematic m odel of the structure of nanostructured Cu-Bi and W-Ga alloys. The open circles represent the Cu or W atoms, respectively, forming the nanometer-sized c rystals. T he b lack c ircles a re t he B i o r G a a toms, r espectively, incorporated in the boundaries at sites of enhanced local free volume. The atomic structure shown was deduced from EXAFS and X-ray and diffraction measurements [Gleiter 1993].
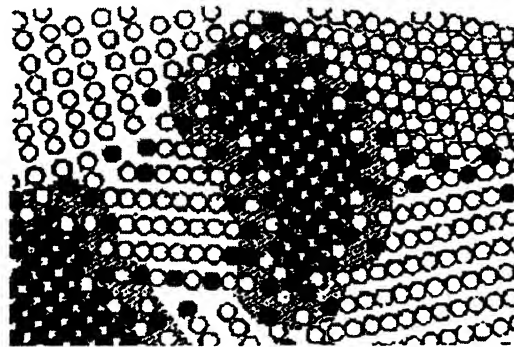


Figure 1.6 Schematic model of nanocrystalline Ag-Fe alloys according to the data of Mossbauer spectroscopy. The alloys consist of a mixture of nanometer sized Ag and Fe crystals (represented by open and full circles, respectively). In the (strained) interfacial regions between Ag and Fe crystals, solid solutions of Fe atoms in Ag crystallites, and Ag atoms in the Fe crystallites are formed although both components are immiscible in the liquid as well as in the solid state. Similar effects may occur in the grain boundaries between adjacent Fe and Ag crystals [Herr et al. 1990].

**TABLE 1.3: METHODS TO SYNTHESIZE NANOCRYSTALLINE MATERIALS**

[Suryanarayana and Koch 1999]

| STARTING PHASE | TECHNIQUE | NATURE OF PRODUCT |
|---|---|---|
| **Vapor** | Inert gas condensation | 3-D |
| | Physical vapor deposition | 1-D |
| | Plasma processing | 3-D |
| | Chemical vapor deposition | 3-D, 2-D |
| **Liquid** | Rapid solidification | 3-D |
| | Electro-deposition | 1-D, 3-D |
| | Chemical reactions | 3-D |
| **Solid** | Mechanical alloying | 3-D |
| | Devitrification | 3-D |
| | Spark erosion | 3-D |
| | Sliding Wear | 3-D |

This method produces typically equiaxed (3-D) crystallites. The crystal size of the powder is a few nanometers and size distribution is narrow. The crystal size is dependent upon the inert gas pressure, the evaporation rate, and the gas composition. Extremely fine particles c an b e p roduced b y d ecreasing either t he gas p ressure i n t he c hamber o r t he evaporation rate by using lighter gas, such as He, rather than heavier inert gas, such as Xe [Siegel 1990, Eifert 2000].

Ping et al. (1995) successfully prepared nanocrystalline Pd by this method. Wunderlich et al. (1990) and Sattler et al. (1994) also prepared Nanocrystalline Pd via this route and found average grain size varying in the range of 10-20 nm. Since this method of preparation is expensive in nature, hence it has not been used extensively for commercial purposes. The advantage of this method is the cleanliness of the process and better control on the grain size of the final product by controlling various parameters involved in the process. The size of the clusters, which upon consolidation become the grains of the nanocrystalline material, can be easily controlled by variation of type, pressure, and temperature of the inert condensing gas and very small clusters, which often exhibit particularly interesting mesoscopic physical and chemical behavior, can be obtained by specific design of the cluster source [Sattler et al. 1994].

## 1.4.2 Rapid Solidification

It i s p ossible t o i ncrease t he n ucleation r ate and d ecrease t he growth rate o f t he s olid phase if the cooling (or the under cooling) during rapid solidification of metallic melts is increased to high value. As a consequence, the grain size of the resultant product will be in the nanometer range. Nanocomposites have been produced by this method during rapid solidification of metallic melts or during devitrification of metallic glasses produced by rapid solidification .A single-phase $HfNi_5$ nanocrystalline alloy has been produced directly by rapid solidification [Lu et al 1995]. The rapid solidification technique is usually applied at the place where the small grain size distribution range is required i.e. uniform distribution of grain size is required. This method is preferred for bulk production of nanocrystalline materials for industrial use due to its easy processing route

and c ost e ffectiveness. Most o f t he c ommercial n anocrystalline m agnetic m aterials a re prepared via this method nowadays.

### 1.4.3 Electro-Deposition

Multilayered metals can be obtained by electro-deposition route by using either two separate electrolytes or from one electrolyte by appropriate control of agitation and the electrical conditions (particularly voltage). These processes can be applied to the synthesis of pure metals, alloys and composites. These processes have high production rates, little size and shape limitations and require a low initial capital investment. Three dimensional nanostructured crystallites can be obtained using this method [Erb 1995].

Rofgha et al. (1991, 1993) studied nanocrystalline Ni-P alloys produced by the electrodeposition techniques for their corrosion behavior and found that alloys produced by this method exhibited uniform corrosion behavior rather than excessive intergranular corrosion, as shown by coarse grained Ni. . Karimpoor et el. (2002) prepared fully dense, porosity free, nanocrystalline cobalt of grain size 12 nm and found considerable increase in yield strength and ultimate tensile strength as compared to conventional polycrystalline cobalt.

### 1.4.4 Spray Conversion Processing

In this technique, aqueous solution precursors are used. The solution mixture is aerosolized and rapidly spray dried to give extremely fine mixture of complex compounds. To prevent g rain g rowth, inhibitors a re a dded during sintering a s binders. WC-Co nanocrystalline composites have been produced on a commercial basis using the "spray conversion processing method" starting from aqueous solution precursors such as ammonium metatungstate $[(NH_4)_6(H_2W_{12}O_{40})_4H_2O]$ and $CoCl_2$, $(Co(CH_3COO)_2)$, or cobalt nitrate $(Co(NO_3)_2)$ [Kear 1993]. As compared to gas condensation techniques, this process requires less production cost as gas condensation techniques require ultra high vaccum during processing which increases the cost of production. Mechanical alloying is

a method of mass production of nanocrystalline powders but the problem of contamination restricts its widespread application. This problem can be overcome by spray conversion processing method.

## 1.4.5 Devitrification

Controlled crystallization of amorphous alloys, produced by other methods, leads to the synthesis of nanostructured materials. In fact, the most common method to produce nanocrystalline materials has been to obtain an amorphous phase by rapidly solidifying the melt of appropriate composition and then crystallizing the glassy phase at a relatively low temperature. This simple devitrification method has been commonly employed to study the magnetic properties of nano-crystalline materials because it can produce porosity free samples and samples with different grain sizes by controlling the crystallization parameters and large quantities of materials [Lu 1996].

A particular class of Magnetic materials, known as FINEMET, were first developed and investigated by Yoshizawa et al. (1988) and this method has now become an established practice to study the structure and properties of nanocrystalline magnetic materials [Lu et al. 1996]. Very recently Yoshizawa (2001) successfully prepared nanostructured FeCuNbSiB alloys, which is known as a typical nanocrystalline soft magnetic material, via Devitrification method.

## 1.4.6 Mechanical Alloying

Mechanical alloying produces nano structured materials by the structural decomposition of coarse-grained structure as a result of severe plastic deformation using high-energy ball mill. This process has produced nanocrystalline structures in pure metals, intermetallic compounds and immiscible alloy systems [Koch 1997]. Mechanical alloying has been dealt in detail in section 2.1.

## 1.4.7 Physical Vapor Deposition

Physical vapor deposition (PVD) refers to coating processes where the transport of material to the substrate is effected by a physical driving mechanism. Such mechanisms include evaporation, sputtering, ion plating, and ion assisted sputtering [Collingon 1999]. Coatings stability and performance is enhanced if they are fully dense and defect free. A nanostructured multilayer coating of TiN/C-N was produced using reactive sputtering with so called side-side configuration [Jassen et al 1999].

Recent improvements in PVD techniques, in particular the use of plasmas and the unbalanced magnetron for the deposition process, have led to its wide application in industry. S uch c oatings are u sed f or c orrosion p rotection, t o p rovide h ard s urfaces f or engineering applications, to form decorative coatings on a range of household and industrial products, for energy saving window glass, for media storage systems such as compact discs and for a range of microelectronics applications. For example, for corrosive coatings film density and tensile stress developed in the coatings during processing are very important factors affecting the corrosion behavior of coatings. It has been found that stress can be reduced via this process. Novelty of energy assisted PVD is that new combinations of the materials can be prepared.

## 1.4.8 Sol Gel Method

Nanometer sized ceramic structures have been generated by means of a sol-gel technique. Both structural and compositional nanometer structures are obtained by "seeding "of a ceramic precursor with crystalline sols of the final equilibrium phase to catalyze nucleation [Roy et al. 1982, 1983, 1984-JAC, 1984-ML, Suwa et al 1985, 1986-JMSL, 1986-MSE, Roy and Roy 1984].

A significant advantage of this method in comparison to methods involving high temperatures (e.g. calcinations, evaporation ) is the low temperature of the method. The

preparation of stoichiometric compounds containing one or more components with a high vapor pressure, e.g. Pb in (BaPb)TiO$_3$ ferroelectrics, poses serious problems due to the Pb loss. This difficulty can be avoided by the sol-gel approach. In fact, the specific surface area of (BaPb)TiO$_3$ sol-gel derived powders have been found to be about 50 m$^2$/g in comparison to 4 m$^2$/g for powders prepared by calcined mixed oxides [Jo and Yoon, 1989].

CoFe$_{2-x}$Mn$_x$O$_4$ (x = 0 − 2.0) nanocrystalline thin films and powders were prepared by sol-gel process by Zhou et al. (2002). Ferrites are well known magnetic materials used as recording media. Cobalt ferrite, CoFe$_2$O$_4$, is one of the good candidates for high density recording media because of its high coercive force, moderate saturation magnetization, better chemical stability and mechanical hardness. For high density recording media, small grain size is very much required. Such a kind of nanostructured material is often prepared by the sol-gel synthesis, which could offer the advantages of lowering annealing temperature for the crystallization process and controlling the grain size by varying the annealing temperature.

## 1.5 STRUCTURE

In order to understand the interrelationship between structure and properties, nanocrystalline materials need to be characterized on both atomic and nanometer scales. The microstructural features of importance include (a) Grain size, grain size distribution and morphology, (b) the nature and morphology of grain boundaries and interphase interfaces, (c) the perfection and nature of intra-grain defects, (d) composition profile across grains and interfaces, and (e) identification of residual trapped species from processing.

There is a gamut of experimental techniques that can yield structural information on nanocrystalline materials. These include 'direct; microscopic techniques such as transmission electron microscopy (TEM), scanning tunneling microscopy (STM)[Higgins 1996, Gao 1993], atomic force microscopy (AFM) [Binnig et al.1986, Bhushan 1995,

Hansma 1996], field ion microscopy (FIM), and less direct electron, X-ray and neutron diffraction techniques. Indirect spectroscopic tools, such as EXAFS, nuclear magnetic resonance, Raman and Mossbauer spectroscopies, and positron annihilation spectroscopy, have also been used. Owing to the Ultrafine scale of nanocrystalline materials, traditional characterization tools such as TEM and X-Ray diffraction technique are both necessary and useful to understand the structure of nanocrystalline materials [Gleiter 1989, Brundle et al 2002].

A nanocrystalline metal contains typically a large number of interfaces with random orientation relationship, and consequently a substantial fraction of the atoms lies in the interfaces (Figure 1.7). Assuming that grains have the shape of spheres or cubes, the volume fraction of atoms associated with the boundaries can be calculated as follows [Andrievski 2001]:

$$V_f = 3s/D \tag{1}$$

where,

S= average grain boundary thickness

D= average grain diameter

It has been observed that volume fraction of atoms in the grain boundaries can be about 50% for 5 nm grains, decrease upto30% for 10 nm grains and 3% for 100 nm grains. Nanocrystalline metals can be considered to consist of two structural components – the numerous small crystallites with long range order and different crystallographic orientations constituting the "crystalline" component and a network of intercrystalline regions, the structure of which differs from region to region: which is referred as the "interfacial" component [Koch 1999].
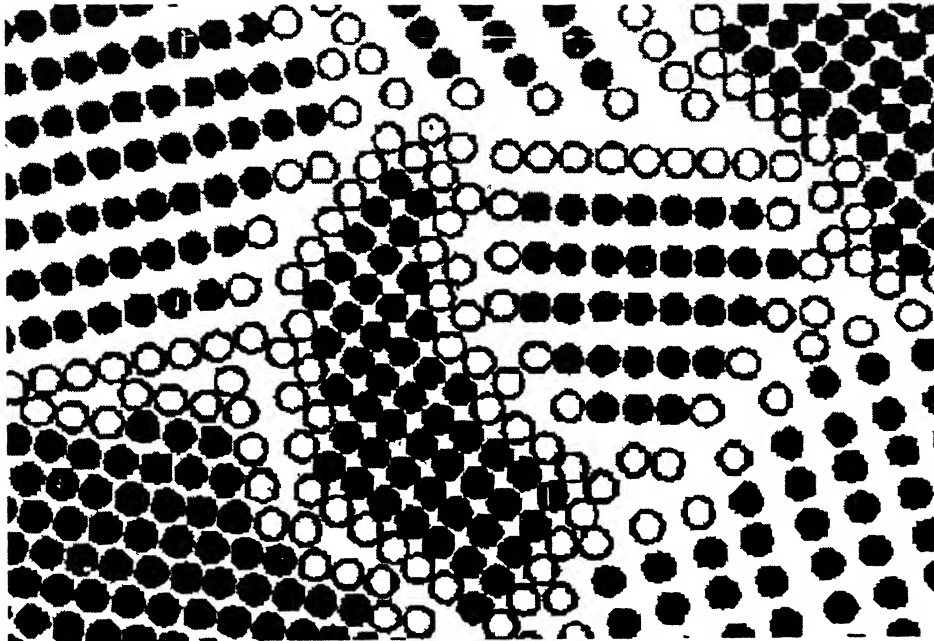
**Figure 1.7 Schematic arrangements of atoms in an equiaxed nanocrystalline metal [Suryanarayana and Koch 1999].**

### 1.5.1 Atomic Structure of the Crystal Lattice

The structure of the grains (crystallites) in nanocrystalline materials has been accepted to be the same as in a coarse-grained materials i.e. long range ordered atomic structure [Haubold et al 1989, Birringer 1989, Gleiter 2000, Siegel 1992].

### 1.5.2 Atomic Structure of the Grain Boundary

Initially it was suggested that nanocrystalline grain boundary atomic structure has "gas like" disorder. But after exhaustive studies on the nature of grain boundary structure, it has been established in most of the cases that interface structures are remarkably close, structure-wise, to those in conventional crystalline materials with micron-sized grains [Siegel 1992, Rangnathan et al 2001, and Horita et al 1996].

For example, molecular dynamics computer simulation, based on experiments, gives clear evidence that grain boundaries in FCC nanocrystalline metals have similar short-range structure of grain boundaries as found in conventional polycrystalline materials [Swygenhoven 2001].

### 1.5.3 Triple Junction and Higher Order Grain Junction

In ultrafine-grained (nanocrystalline) materials, triple junctions and higher order junctions become an important component of the microstructure. The total inter crystalline region consisting of grain boundaries, triple junctions and four-grain points is more important than just the grain boundary.

The grain boundary area is inversely proportional to the grain size while the triple line length is proportional to the inverse square of the grain size. Thus the contribution of triple junction and higher order grain junction becomes important at very small grain size [Koch 1997].

## 1.6 STABILITY

The thermal stability is important for consolidation of nano-crystalline powders without coarsening the microstructure. Grain growth occurs in polycrystalline materials to decrease the system energy by decreasing total grain boundary energy. Grain growth can be measured by the following expression [Gleiter 2000]:

$$D^{1/n} - D_0^{1/n} = kt \qquad (2)$$

where,

D=length scale or mean grain diameter

n=empirical constant =< 0.5

$D_0$ = length scale or mean grain diameter at t=0

k= temperature dependent rate parameter, t= Annealing time

By applying, $k=k_0 \exp(-Q/RT)$, activation energy Q can be calculated and which in turn can be used to deduce the grain growth mechanism.

Nanocrystalline metals exhibit crystal growth at elevated temperatures. In metals with a crystal size of about 10 nm, significant crystal growth (doubling of the crystal size in about 24 hours) was noticed at ambient temperature or below if the equilibrium melting temperature, $T_m$, was lower than about $600^0$C. However, if $T_m$ was higher, the stability against grain growth seems to be enhanced [Gleiter 1989]. The grain growth in mechanically alloyed solid solution has been found to decrease with increasing solute concentration, and the heat release upon annealing indicates that solute segregates to the grain boundaries, thereby reducing the specific grain boundary energy and impeding grain growth [Krill et al 1995].

# 1.7 PROPERTIES OF NANOCRYSTALLINE MATERIALS

Due to presence of very fine grain size structure, nanocrystalline materials have unique properties that are different and considerably improved in comparison with those of conventional coarse grained polycrystalline materials. These include increased strength and hardness, enhanced diffusivity, improved ductility and toughness, reduced density, reduced elastic modulus, higher electrical resistivity, increased specific heat, higher thermal expansion coefficient, lower thermal conductivity, and better soft magnetic properties in comparison with conventional coarse-grained materials.

## 1.7.1 Diffusion and Sinterability

Since nanocrystalline materials contain a very large fraction of atoms at the grain boundaries, the numerous interfaces provide a high density of short circuit paths for diffusion. As a consequence, they exhibit an enhanced diffusivity in comparison to with single crystal or conventional coarse-grained polycrystalline materials with the same chemical composition [Schumacher et al.1989, Hofler 1993].

This enhanced diffusivity can have a significant effect on mechanical properties such as creep and superplasticity, ability to dope efficiently nanocrystalline materials with impurities at relatively low temperatures, and synthesis of alloy phases in immiscible metals and at much lower than those usually required in other systems. The enhanced self and impurity diffusivities in nanocrystalline materials appear to be strongly linked to the porosity present in the samples. However, in the light of recent results, the difference in diffusion coefficients seems to be caused by differences in relaxation states rather than by porosity [Hofler 1993].

Solid solubility limits are usually enhanced when the material is in the nanocrystalline state and this has been explained on the basis of elastic strains at the interfaces. The high diffusivity results in alloying, by diffusion along grain boundaries resulting in the

formation of stable and metalstable phases at relatively low temperatures. Another important consequence of the increased diffusivity is that sintering of nanocrystalline powders can occur at temperatures lower than those required for coarse-grained polycrystalline powders.

## 1.7.2 Mechanical Properties

The elastic constants of nanocrystalline materials have been found to be reduced by 30% or less. The presence of extrinsic defects e.g. pores and cracks, was suggested as the possible reason for low values of Young's modulus in nanocrystalline materials compacted from powders [Krstic 1993].

The Hall-Petch relationship for conventional coarse-grained polycrystalline materials suggests that the yield strength (or hardness) of a material increases with a decreasing grain size according to the relationship,

$$\sigma = \sigma_0 + k_H\, d^n \qquad\qquad (3)$$

where, d= grain size, $\sigma$ = 0.2% yield strength (or hardness),

$\sigma_0$ = lattice friction stress to move individual dislocations (or the hardness of a single crystal specimen, d $\rightarrow$ infinity)

n = the grain size exponent (generally -1/2), $k_H$ = Hall-Petch intensity parameter

At extremely fine grain sizes, e.g. in the nanometer regime, the individual grains cannot support more than one dislocation; and thus, the Hall-Petch relationship may not be valid. The deviation from the Hall-Petch relationship in nanocrystalline materials may be due to the following reasons:

a) Since in nanocrystalline materials, pile-ups can not form when the grain size is less than a critical value $d_c$, weakening mechanisms (e.g. viscous type flow) operate and leads to a decrease in hardness with decreasing grain size, i.e. a negative value for the slope $k_H$.

b) A large number of triple junctions may be a reason for negative slope in nanocrystalline materials as an increased triple junction volume fraction leads to softening and enhanced bulk ductility in polycrystalline materials [Palumbo et al. 1990, Nieh et al. 1991].

Summery of the mechanical properties of nanocrystalline materials can be given as follows [Suryanarayana and Koch 1999]:

(i)     Except for very small grain nanocrystalline samples (<5 nm) the elastic properties are essentially identical to those of coarse-grained materials.

(ii)    High hardness and yield strength values are observed for nanocrystalline materials.

(iii)   Ductile coarse-grained materials are less ductile, perhaps brittle as nanocrystalline materials.

(iv)    Brittle coarse-grained materials may exhibit slight ductility when nanocrystalline.

(v)     Superplasticity has not been observed at low temperatures (<0.4 to 0.5 Tm) for nanocrystalline materials, although it has been observed at somewhat lower temperatures and higher strain rates as grain size decreases.

(vi)    Shear banding and perfectly plastic behavior have been seen in some nanocrystalline materials analogous to plastic deformation in amorphous materials.

## 1.7.3 Electrical Properties

The electrical resistivity of nanocrystalline materials has been found to be higher than that in both coarse-grained polycrystalline and amorphous alloys. The increased volume fraction of atoms lying at grain boundaries is considered responsible for the increase in electrical resistivity. The phenomenon of giant magnetoresistance (GMR) (decrease in electrical resistance of materials when exposed to a magnetic field) has been reported in number of multilayer systems. Whereas the resistance drop is only 1-2% in conventional

coarse-grained materials, the drop is as large as 50-80% in the case of nanocrystalline materials [Baibich et al 1988].

## 1.7.4 Specific Heat

The specific heat in the nanocrystalline state is much higher than that in the coarse grained material (by as much as 50% in some cases) and even in the amorphous material. The specific heat of a material is closely related to its vibrational and c onfigurational entropy, which is significantly affected by the nearest neighbor configurations. Thus, the increase in specific heat of nanocrystalline materials has been attributed to the small crystal size (and consequent large interfacial component).

## 1.7.5 Magnetic Properties

Different magnetic properties of nanoscale ferromagnetic materials, as compared to conventional one, can be attributed to their small volume. It means that they are typically single domain, and a large fraction of atoms are associated with the grain boundaries/interfaces. If the single domain nanoscale ferromagnetic particles (e.g., Fe, Co, or Ni) are put in a non-magnetic matrix such that their magnetic interaction is negligible, a superparamagnetic material is obtained. If the grain size is small enough, the structural distortions associated with the surfaces or interfaces can lower the Curie temperature, Tc, and reduce the magnitude of the saturation magnetization Ms.

While the very low losses of the nanocrystalline soft magnetic materials (FINEMET or Nanoperm) are dependent on the nanometer grain size for their properties, the hard magnetic nanocrystalline alloys with remanence enhancement provide flexibility in processing, especially with powder materials. These remanence enhanced nanocrystalline hard m agnetic a lloys m ay find m any applications a s p ermanent m agnetic c omponents. Two important requirements for alloys to exhibit remanence enhancement are a nanocrystalline grain size and a degree of coherence across interphase boundaries sufficient to enable adjacent phases to be exchanged coupled.

The magnetocaloric effect is another magnetic property that can be enhanced in nanocrystalline microstructures. Small magnetic particles in a non-magnetic matrix exhibit alignment of the magnetic spins in a magnetic field. This increase in magnetic order lowers the magnetic entropy of the spin system. If this process is performed adiabatically the reduction in spin entropy is offset by an increase in lattice entropy and the specimen temperature will rise. This temperature rise $\Delta T$ is reversible – the specimen cools down on removal of the magnetic field- and is known as the magnetocaloric effect.

### 1.7.6 Chemical Properties

A majority of the processing methods produce the nanocrystalline materials in the form of powder, and therefore the total surface area available can be accurately tailored by controlling the particle and grain sizes through the processing parameters. Most important evidence of chemical reactivity of such material is demonstrated by their enhanced catalytic activity [Beck and Siegel 1992]. Recently, it has been emphasized that such catalytic activity is evolved in the environmental problems due to enhancement in the activity of aerosols due to their fine size.

The effect of particle size on gas-metal interaction has been utilized in the development of nanocrystalline materials for hydrogen storage application. Moreover, enhanced diffusion mechanism in nanocrystalline materials may also be included in the novel chemical properties. Hydrogen absorbing alloys (FeTi, $LaNi_5$, $Mg_2Ni$, and other Mg-based materials) in the nanocrystalline form show much better hydrogen sorption properties than their polycrystalline counterparts.

### 1.8 APPLICATIONS: PRESENT AND POTENTIAL

Being the new area, a lot of research is going on for potential use of nanostructured materials. Based on the properties of these materials, so many applications of these materials have been suggested. At present, bulk nanostructured soft magnetic iron based alloys and WC-Co composites have found industrial use.

## 1.8.1 Structural Applications

Higher hardness, strength and deformation than the conventional materials provide ground for wide application of nanocrystalline materials.

## 1.8.1.1 Cutting Tools

It has been shown that the hardness and strength of nanocrystalline materials is 4-5 times higher than that of coarse-grained materials of same composition. For example, in WC-Co composites it has been found that hardness of WC-Co composites, with WC grains in nanometer size range, increases with decreasing grain size reaching values as high as 2,200 VHN. Scratch test suggests that higher hardness in nanograined WC-Co is also accompanied by increased toughness. Thus, the abrasive wear resistance of nanostructured WC-Co is higher than that of conventional WC-Co when comparison is made at equal hardness. Thus, nanocrystalline WC-Co cutting tools are expected to have more than doubled the lifetime than conventional coarse-grained composite. These materials could be used as fine drill bits for drilling holes in PCBs and as rotary cutting tools [McCandlish et al. 1994].

## 1.8.1.2 Nanocomposites

Nanocomposites are those materials in which either the reinforcement or the matrix or both are on a nanometer scale. Further, Nanocomposites may be such that the nanoreinforcement may be distributed either in the grain boundaries or inside the grains. It has been known that dispersing a second phase on a microscopic scale can considerably enhance the fracture toughness of ceramics. Since reducing the grain size to nanometer dimensions can provide increased strength and hardness, it is suggested that fabrication of micro/nanohybrids will lead to class of supertough and superstrong ceramics. In these hybrids, a Nanocomposite matrix is reinforcement with sub micron sized particles like whiskers, platelets, and long fibers and these hybrids show enhanced fracture toughness

and strength up to very high temperatures, where the properties of coarse grained composites normally degrade.

Further, nanoreinforcements increase creep resistance by suppressing grain boundary sliding. Consequently, nanoreinforcements are now being used to boost the performance of a growing number of composites. Nanocrystalline fibers also are used to reinforce composites [Bhaduri and Bhaduri 1998]. While high hardness and strength are usually associated with low ductility, it has been shown that a uniform dispersion of about 20 vol% of a Nanocrystalline phase in an amorphous matrix increases the strength of the material significantly while maintaining an adequate level of ductility in the composite [Inoue et al. 1994].

## 1.8.1.3 Superplastic Materials

Materials in the Nanocrystalline state show tendencies of Superplastic deformation at temperatures lower and strain rates higher than conventional coarse-grained materials. Since ceramics and conventionally brittle intermetallics can be rendered ductile at elevated temperatures (at least in some cases) by nanostructure processing, these materials can be formed to near-net shapes by means of deformation processing methods previously applicable only to produce ductile metal parts.

## 1.8.1.4 Coatings

As we have seen earlier that Nanocrystalline materials have high hardness and strength than that of conventional ones, these properties can be utilized to produce wear resistance coatings. Thermal barrier coatings of a metallic bond coat, usually MCrAlY, a thermally grown $Al_2O_3$ film, and s ceramic layer, usually yttria stabilized zirconia. These coatings reduce superalloy metal temperatures by as much as 300F, and thereby provide durability to combustors, transition ducts, and turbine vanes. With the gas turbine industry's demand for higher operating temperatures to provide enhanced fuel efficiency, thermal barrier c oatings w ith r educed t hermal c onductivity p rovide t he h ighest p ay-off c oating

application. One can also deposit Nanocrystalline coatings to improve the wear resistance while retaining a tough interior for low-temperature application.

## 1.8.2 Magnetic Applications

The exceptional soft magnetic properties of the "FINEMET" and "Nanoperm" Nanocrystalline/amorphous Fe-base alloys promise applications in transformer cores for power frequencies, saturable reactors, high frequency transformers, and magnetic heads. Additional probable applications are for data communication interface components, sensors, and common mode choke coils and magnetic shielding.

Magnetic recording materials to some extent already use nanostructured materials. Magnetic materials are used in both the information storage media and in the "write" and "read" heads. It is predicted that in the future essentially all media and heads will contain nanostructured materials. There is now a large market for strong rare-earth based permanent magnets in a wide variety of applications, and flexibility in manufacturing and lower materials costs (less expensive rare earth metals needed in remanence enhanced magnets) should encourage use of nanostructured materials.

## 1.8.3 Electronic Applications

"Functional" electronic and optical nanostructures are typically fashioned from single crystal semiconductor materials using a variety of possible pattern formation (e.g., electron beam lithography) and pattern transfer processes (e.g., reactive ion etching), which can create structures at the nanoscale. By replacing inks with nanoparticles solutions, it is also conceivable that we could print structures onto surfaces e.g., printing electronic circuits. This is large area of research and development of importance to the microelectronics industry for future directions such as quantum circuits and systems, massive memory, architecture and interconnected systems.

## 1.8.4 Catalysis and Hydrogen Storage Materials

When a sample is divided into small portions, high specific surface area is obtained. A lot of studies show that catalytic activity and selectivity can be dependent on particle size that is why finely dispersed materials are used in catalysis. Metal hydrides are the best option available for storage of hydrogen for use as a fuel. It was believed that a way to enhance their properties is to produce the materials in Nanocrystalline form. The high density of grain boundaries/interfaces might increase diffusion. Nanocrystalline Mg2Ni inclusions in a two phase Mg/Mg2Ni alloy showed improved hydrogen storage behavior in term of Mg2Ni catalyzing the decomposition of the molecular hydrogen, greatly increasing the hydrogen absorption/desoprtion kinetics.

## 1.8.5 Bio-Medical Applications

Magnetic nanoparticles are being used in biomedical research on cell separation, for magnetically targeted drug delivery, for protein and DNA purification, and for contrast enhancement in magnetic resonance imaging (MRI). Functionalization of the nanoparticle surface could enable the selective attachment to particular type of cells. Magnetic nanoparticles for selective tag could someday be used in HIV immune therapy or the treatment of blood diseases.

If magnetic nanoparticles were attached to cancer cells, they could be for hypothermia, raising the local temperature about 420C increases their sensitivity to radiation and chemotherapy, and heating above 420C causes a significant amount of cell death. Nanoparticles additions can be used in suns creams and cosmetics to protect our skin against UV rays in plastics for out door applications to prevent UV-induced weathering and in bottle coatings to protect beer, wine and olive oil against photo degradation.

## 1.9 CONSOLIDATION STRATEGY FOR NANOCRYSTALLINE MATERIALS

The potential application of nanoscale materials as novel structural or functional engineering materials largely depends on the consolidation of powders into bulk nanoscale solids. The retention of metastable microstructure in the course of this consolidation process is essential for preserving the often superior mechanical, magnetic, or catalytic properties of the material [Gleiter 2000]. Consolidation of the nanocrystalline powders has been achieved by **electro-discharge compaction; plasma activated sintering, explosive consolidation, hot isostatic processing, hydrostatic extrusion, strained powder rolling** and **sinter forging** [Suryanarayana 1999, Siegel 1994, Groza 1999, ].

Optimization of consolidation parameters is important because retention of nanostructures requires use of low consolidation temperatures while achieving full (theoretical) density requires use of high temperatures [Ma and He 2000]. However, it should be noted that because of the increased diffusivities in nanocrystalline materials, sintering takes place at a temperature much lower than in coarse-grained materials. This is likely to reduce the grain growth. It is typically difficult to obtain full density while retaining the nanoscale microstructure. The high driving force and enhanced kinetics due to large curvature facilitates full densification of nanocrystalline materials at temperatures below those of coarse grained materials of the same composition by few hundred degrees [Ma 2000, Ma and He 1996]. Retention of fine grain sizes and elimination of sintering aids are specific advantages of the lower processing temperatures [Liu 1998, Suryanarayana and Froes 1989, Hofler et al 1993].

## 1.9.1 Effect of Temperature on Consolidation

For conventional materials, pores are removed through sintering at high temperatures for long times, driven by the reduction in surface energy whereas for nanophase materials, consolidation temperature needs to be kept low to maintain nano scale grain sizes. Full densification is possible at some intermediate elevated temperatures because nanophase powders are expected to show increased sinterability compared with their conventional coarse-grained counterparts. A reduction in sintering temperature can reduce contamination and compositional changes, and stresses and cracking during cooling. A number of factors contribute to this possible processing advantage. For mechanically milled powder, particles with varying sizes may lead to easier filling of pores of different sizes. Fine grain sizes provide shorter diffusion paths and much increased densification rate during sintering [Ma 2000].

It is obvious that the diffusional processes that mediate sintering also lead to undesired grain growth. The driving force for grain growth also increases, as grain size decreases such that the advantage nanophase materials have in sinterability can be partly lost due to concomitant grain growth that destroys the desirable nanoscale grain size. Therefore, consolidation temperature needs to be maintained sufficiently low, and other mechanisms (such as stress assisted densification) must be invoked to allow full consolidation and retention of nanostructure.

## 1.9.2 Effect of Pressure on Consolidation

To compensate for the low consolidation temperature the strategy usually adopted is to use hot pressing and forging employing high pressure ( of the order of 0.5-1.0 GPa) to enhance the contribution of plastic deformation and bonding. The high stress enhances the plastic strain controlled pore closure. Also, the stress plays a significant role in stress assisted densification (diffusion) mechanisms. Possible stress effect on deformation and densification can be seen from the established formula for creep, in general,

$$\partial\varepsilon/\partial t = A\sigma^{n}/RTd^{q}*exp\,(-Q/RT)\,f\,(\rho) \qquad \cdots\cdots\cdots (4)$$

Where, $\sigma$ is the applied stress, d the grain size, $\partial\varepsilon/\partial t$ the strain rate, n= the stress exponent, q the grain size dependent exponent, A, a coefficient involving diffusivity prefactor, Burger vector, shear modulus etc., Q the activation energy for the accommodation process, $\rho$ the density, R the gas constant, and T the temperature. In this expression, A, n, q, and Q can have different values for different creep mechanisms (Nabarro-Herring creep, Coble creep, Dislocation climb power law creep etc.), and f $(\rho)$ accounts for density effects.

The equation indicates that the high pressure applied and the strong grain size dependence of creep deformation can contribute significantly to densification by plastic deformation at relatively low temperatures. In addition, the extensive plastic deformation under high stress results in disruption of any continuous surface oxides on powder particles, which may degrade bonding and properties. The high pressure applied may also have the beneficial effects of slowing down grain growth because of the reduction of free volumes in grain boundaries, which facilitate atomic jump across the boundary.

### 1.9.3 Effect of Contamination

Surface contamination is inevitable for any powder material and may become significant in nanopowders due to their large surface area. Metastable powders obtained by mechanical alloying or milling are special case. Their structure is either amorphous or nanocrystalline but the powder particle size is in the micron range. In this case, the surface area is less than for nanometer powder particles but contamination is due to large impurity intake during the milling process. Oxides, nitrides and other compounds are often found in consolidated parts made of attrition-milled nanopowders.

Studies show that ultra clean nanoparticles sinter very rapidly even at room temperature. The oxygen contamination decreases the surface energy and slows down the sintering kinetics. To reduce contamination, all the mechanical alloying and consolidation should

be performed under inert atmosphere. To reduce metallic impurities acquired during milling, milling media and materials being milled should match in composition.

## 1.9.4 Suppression of Grain Growth

Compared with the grain sizes in as milled powder, grain growth is observed in all consolidation techniques. There could be several possible ways for suppression of runaway grain growth during consolidation. First of all, sinter forging scheme allows full density processing at relatively low temperatures, significantly below $0.5Tm$, resulting in less grain growth than other consolidation methods, second, a minute amount of impurities picked up during milling, although often below the detection limit, may have also contributed to the success in suppressing grain growth through solute drag or Zener drag mechanism. These trace impurities are uniformly distributed by the milling action, reducing the possibility of abnormal grain growth.

Grain size stability is especially high when a second element, copper is added into iron. In this case, additional factors contribute to the retention of nanoscale grain sizes in consolidated composites. First of all, the powder after mechanical milling consists of a super saturated solid solution, with iron and copper alloyed on the atomic scale due to the non-equilibrium nature of the milling process. The solute drag effect, due to the solute atoms segregating to grain boundaries, retards grain growth. Second, upon heating during consolidation, phase separation into f.c.c. copper and b.c.c. iron occurs inside the nanograins or along the abundant grain boundaries. The new grains thus start out with sizes smaller or atleast similar to those in the nanocrystalline precursor phase. Third, the resultant two phase mixture configuration helps to isolate grains and/or domains of the same structure and thereby reduce grain growth boundary migration. In other words, incorporating a second phase or element helps to retain nano phase grain size when reaching full density.

## 1.10 KINETICS OF NANOCRYSTALLINE (METASTABLE) PHASE TRANSFORMATION

Many metastable phases are found in the nature and also have been produced by the recently developed novel materials processing techniques. According to the thermodynamics, there is a possibility for both stable and metastable phases to form [Ishihara 1999]. There are two reasons as to why metastable phases form. These are:

1) Metastable phases can nucleate before the stable phases can nucleate
2) The crystal growth rate of the metastable phase exceeds that of the stable phase.

### 1.10.1 Nucleation of the Metastable Phases

It is well known according to the Ostwald step rule (Ostwald 1897) that the first phase to appear will be a metastable phase which has a higher free energy than the stable phase. The excess free energy of critical nucleus ($\Delta G^*$) can be expressed as:

$$\Delta G^* = (16/13)*\pi*(0.065)^3 *\Delta H_f*[T_m^2/(T_m-T)^2] \qquad \ldots\ldots\ldots(5)$$

Where $\Delta G^*$ = the excess free energy of critical nucleus, $\Delta H_f$ = the enthalpy of fusion, $T_m$ and T are melting temperature and temperature of cooling ($T<T_m$).

Figure 1.8, shows a schematic illustration of excess free energy for critical nucleus for stable and metastable phases vs. temperature. The condition (B<1) should usually be satisfied because $\Delta H_f$ approaches $\Delta G$ at low temperatures and $\Delta G^*$ for the metastable phase is always less than that of the stable phase. Therefore, it may generally be expected the nucleation frequency of the metastable phases is larger than that of the stable phase if the under-cooling is large enough.

## 1.10.2 The Crystal Growth Rate of the Metastable Phase

There have been only a few schematic studies of the growth rate. In general, the growth rate can be expressed as a function of the undercooling by the equation (Jackson 1984):

$$S = S_0 (\Delta T)^{\beta} \qquad \dots\dots\dots\dots(6)$$

Where $S_0$ and $\beta$ ($1 < \beta < 2$) are constants, and $\Delta T$ is the degree of undercooling. $S_0$ and $\beta$ have no physical significance. However when $\beta$ of the metastable phase is larger than that of the stable phase, the growth rate of the metastable phase become larger than that of the stable phase at a undercooling as shown in the Figure 1.9. Such a situation can occur when the stable phase has a faceted solid liquid interface while the metastable phase has a molecularly rough interface. In this Figure, $\beta$ of stable and metastable phases is 1.4 and 2.0 respectively. For $S_0$, the value for the metastable phase is three times larger than that of the stable phase.
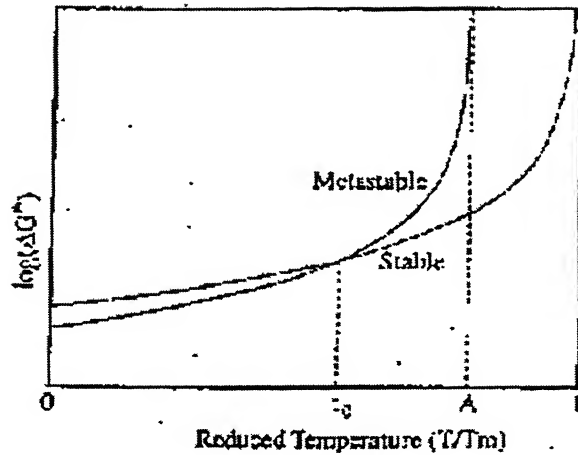
**Figure 1.8 Schematic illustration of excess free energy for critical nucleus for stable and metastable phases vs. temperature [Ishihara 1999].**
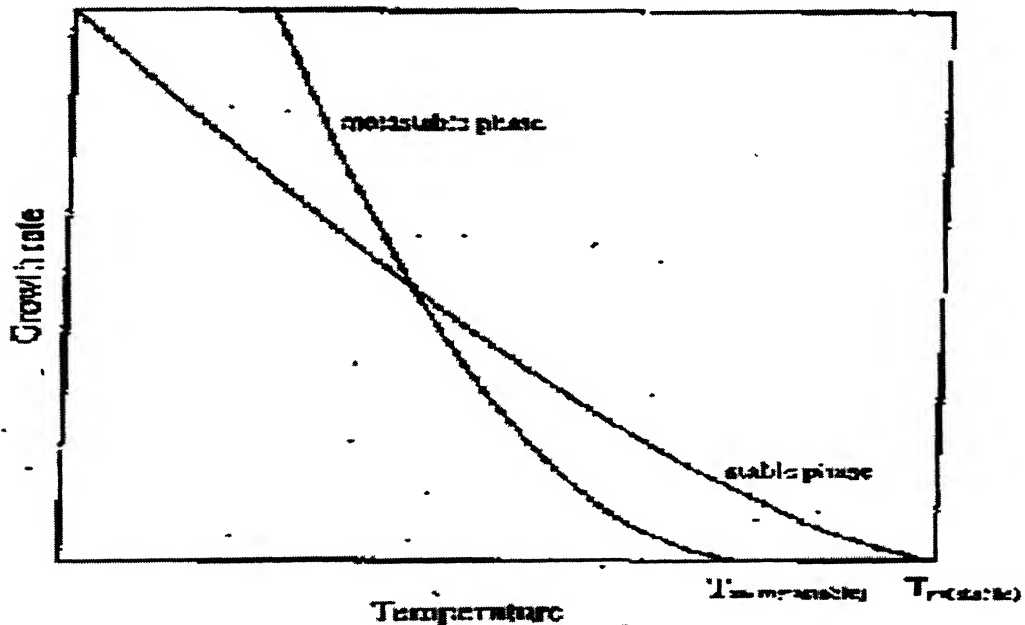


**Figure 1.9 Hypothetical relation of the growth rate for both stable and metastable phases. In this Figure, β of stable and metastable phases is 1.4 and 2.0, respectively. For S0, the value for the metastable phase is three times larger than that of the stable phase [Ishihara 1999].**

# CHAPTER 2

## 2. "MECHANICAL ALLOYING – EXPLOSIVE COMPACTION":
### A POSSIBLE ROUTE FOR PREPARING NsM FROM METAL POWDERS

Amongst the different options for preparations, the mechanical alloying of powders with high energy ball milling has been considered the most powerful method for nanostructured materials because of its simplicity, relatively inexpensive equipment, and the possibility of producing large quantities, that can be scaled up to several tons. Mechanically processed micronsized powders have been shown to posses nanosized substructures or even to become amorphous with appropriate milling parameters. In most systems, the nanograins or amorphous structure represents a "far from equilibrium" condition that is generally quite metastable in nature.

For most commercial applications, the nanostructured powders must be consolidated and further processed to create a final shape. Conventional consolidation and forming processes such as hot isostatic pressing (HIP) or hot extrusion require elevated temperatures for extended times, which considerably coarsen the metastable structure and greatly compromise the novel properties of the as milled powder. Explosive or shockwave consolidation is a means of consolidating particulates without high bulk temperatures. Passage of a large amplitude compressive stress wave resulting from plate impact or detonation of an explosive can cause densification by plastic flow in the particulates. Under appropriate conditions, bonding occurs by interparticle melting and rapid solidification. Melting is generally restricted to near-surface regions, and the bulk of the powder particles remains relatively cool.

Since the nanocrystalline powder prepared by mechanical alloying is highly metastable in nature, they require such a process of densification which does not allow grain to coarsen. The explosive compaction process has been proved most suitable for this purpose as it

produces high temperature and high pressure, which is an ideal condition for better compaction of powders. Since high temperature and high pressure are applied for a short duration of time, grain coarsening is restricted and this feature of explosive compaction makes it an ideal consolidation process for nanocrystalline powders. We will discuss the "mechanical alloying-explosive compaction" route in detail in this section.

## 2.1 MECHANICAL ALLOYING

Mechanical alloying is normally a dry, high-energy-ball-milling technique and has been employed to produce a variety of commercially useful and scientifically interesting materials. This technique was developed around 1966 by John S. Benjamin and his colleagues at the Paul D. Merica Research Laboratory of the International Nickel Company (INCO).

Mechanical alloying (MA) is a powder processing technique that allows production of homogeneous materials starting from blended elemental powder mixtures. This solid state powder processing technique involves repeated welding, fracturing, and rewelding of powder particles in a high energy ball mill. Originally developed to produce oxide-dispersion strengthened nickel and iron base superalloys for applications in the aerospace industry, MA has now been shown to be capable of synthesizing a variety of equilibrium and non-equilibrium alloy phases starting from blended elemental or prealloyed powders. The non-equilibrium phases synthesized include supersaturated solid solutions, metastable crystalline and quasicrystalline phases, nanostructures, and amorphous alloys [Suryanarayana 1999, 2001].

The actual process of MA starts with mixing of the powders in the right proportion and loading the powder mixture into the mill along with the grinding medium (generally steel balls). This mix is then milled for desired period of time until a steady state is reached when the composition of every powder particle is the same as the proportion of the elements in the starting powder mix. Some of the attributes of the MA process are as follows:

- Production of fine dispersion of second phase (usually oxide) particles
- Extension of solid solubility limits
- Refinement of grain sizes down to nanometer range
- Synthesis of novel crystalline and quasicrystalline phases
- Development of amorphous phases
- Disordering of ordered intermetallics
- Possibility of alloying of difficult to alloy elements
- Inducement of chemical reactions at low temperatures
- Scaleable process

Now, we will discuss the different parameters involved in the selection of raw materials, types of mills, and process variables.

## 2.1.1 Raw Materials

The raw materials used for MA are widely available commercially pure powders that have particles sizes in the range of 1-200μm. But, the powder particle size is not very critical, except that to should be smaller than the grinding ball size. This is because the powder particle size decreases exponentially with time and reaches a small value of a few microns only after a few minutes of milling. The raw powders fall into the broad categories of pure metals, master alloys, prealloyed powders, and refractory compounds. Ductile-ductile, ductile-brittle, and brittle-brittle powder mixtures are milled to produce novel alloys.

Occasionally, metal powders are milled with a liquid medium and this is referred to as wet grinding. If no liquid is involved then it is referred to as dry grinding. It has been reported that wet grinding id a more suitable grinding method than dry grinding to obtain finer-ground products because the solvent molecules are adsorbed on the newly formed surfaces of the particles and lower their surface energy. The less-agglomerated condition of the powder particles in the wet condition is also a useful factor. It has been reported

that the rate of amorphization is faster during wet grinding than during dry grinding. A disadvantage of wet grinding is the increased contamination of the powder.

## 2.1.2 Types of Mills

Different types of high energy milling equipments are used to produce mechanically alloyed powders. They differ in their capacity, efficiency of milling and additional arrangements for cooling, heating, etc. A brief description of different mills is provided below.

### 2.1.2.1 SPEX Shaker Mills

Shaker mills such as SPEX mills which mill about 10-20 grams of the powder at a time, are most commonly used for laboratory investigations and for alloy screening purposes. The common variety of the mill has one vial, containing the sample and grinding balls, secured in the clamp and swung energetically back and forth several thousand times a minute.

The back and forth shaking motion is combined with lateral movements of the ends of the vial, so that the vial appears to be describing a Figure 8 or infinity sign as it moves. Because of the amplitude (about 5cm) and speed (about 1200 rpm) of the clamp motion, the ball velocities are high (of the order of 5 m/s) and consequently the force of the ball's impact is great. Therefore these mills are considered as high energy variety.

### 2.1.2.2 Planetary Ball Mills

Another popular mill for conducting MA experiments is the planetary ball mill (referred to as Pulverisette) in which a few hundred grams of the powder can be milled at a time. The planetary mill owes its name to the planet-like movement of its vials. These are arranged on a rotating support disk and a special drive mechanism causes them to rotate around their own axes. The centrifugal force produced by the vials rotating around their

own axes and that produced by the rotating support disk both act on the vial contents, consisting of material to be ground and the grinding balls. Since the vials and the supporting disk rotate in the opposite directions, the centrifugal forces alternately in like and opposite directions. This causes the grinding ball to run down the inside wall of the vial – the friction effect, followed by the material being ground and grinding balls lifting off and traveling freely through the inner chamber of the vial and colliding against the opposite inside wall – the impact effect (Figure 2.1a and 2.1b).

## 2.1.2.3 Attritor Mills

A conventional ball mill consists of a rotating horizontal drum half-filled with small steel balls. As the drum rotates the balls drop on the metal powder that is being ground. The rate of grinding increases with the speed of rotation. Attritors are the mills in which large quantities of powder (from about 0.5 to 40 kgs) can be milled at a time.

## 2.1.2.4 New Designs

Several new designs of mills have been developed in recent years for specialized purposes. These include the rod mills, vibrating frame mills, and the equipment available from Dymatron Cincinnati, OH; Super Misuni NEV-MA-8 from Nisshin Giken, Tokyo, Japan (with the ability to control the temperature of milling from very low temperatures by spraying liquid nitrogen up to a high temperatures of $300^0C$ by electrical heating); Uni-Ball-mill from Australian Scientific Instruments (it is possible to control the nature and magnitude of impact of the balls in this machine by controlling the field strength with the help of adjustable magnets) etc.
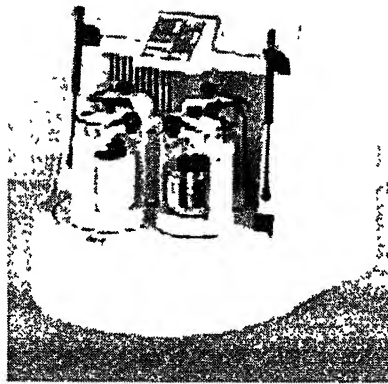
(a)
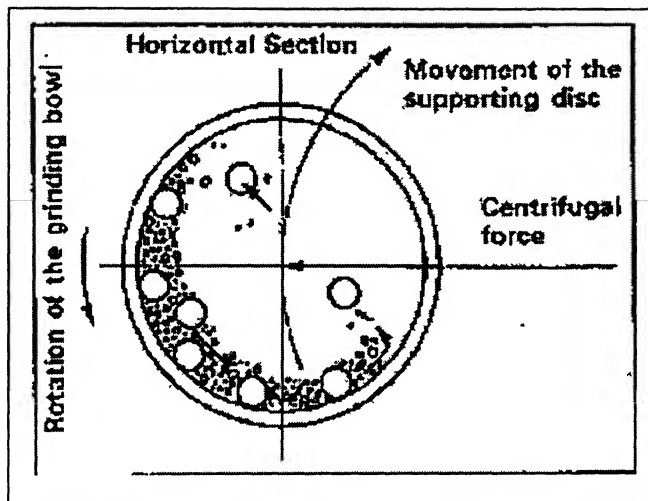


(b)

Figure 2.1. (a) Fritsch Pulverisette P-5 four station ball mill. (b) Schematic depicting the ball motion inside the ball mill. Courtesy of Gilson Company. Inc. Worthington, OH.

## 2.1.3 Process Variables

Mechanical alloying is a complex process and hence involves optimization of a number of variables to achieve the desired product phase and/or microstructure. Some of the important parameters, that have an effect on the final constitution of the powder, are:

- Type of mill,
- Milling container,
- Milling speed,
- Milling time,
- Type, size, and size distribution of the grinding medium,
- Ball-to-powder weight ratio,
- Extent of filling the vial,
- Milling atmosphere,
- Process control agent, and
- Temperature of milling

All these processes are not completely independent. Even then, we will discuss the effect of these variables, assuming mostly that other variables have no significant effect on the specific variable being discussed, on the final product obtained after MA.

## 2.1.3.1 Type of Mill

There are number of different types of mills for conducting MA. These mills differ in their capacity, speed of operation, and their ability to control the operation by varying the temperature of milling and the extent of minimizing the contamination of the powders. Depending on the type of the powder, and the final constitution required, a suitable mill can be adopted.

## 2.1.3.2 Milling Container

The material used for the milling container is important because if the material of the grinding vessel is different from that of the powder, then the powder may be contaminated with the grinding vessel material during grinding. The shape of the container also seems to be important, especially the internal design of the container. Alloying was found to occur at significantly higher rates in the flat-ended vial than in the round-ended container.

## 2.1.3.3 Milling Speed

It is easy to realize that the faster the mill rotates the higher would be the energy input into the powder. But, depending on the design of the mill there are certain limitations to the maximum speed that could be employed. In the conventional mill there is an upper speed limit and if the speed in increased above this critical speed (upper limit), the balls will be pinned to the inner walls of the vial and do not fall down to exert any impact force on the powder. Therefore, the maximum speed should be well below the critical speed so that balls fall down from the maximum height to produce maximum collision energy.

Another limitation is that at high speeds, the temperature of the vial may reach a high value. This may be advantageous in some cases where diffusion is required to promote homogenization and/or alloying in the powders. But, in some cases, this increase in temperature may be a disadvantage because the increased temperature accelerates the transformation process and results in the decomposition of supersaturated solid solutions or other metastable phases formed during milling. Additionally, the high temperature generated may also contaminate the powders. It has been reported that during nanocrystal formation, the average crystal size increases and the internal strain decreases at higher milling intensities due to the enhanced dynamical recrystallization [Suryanarayana 1999, 2001].

## 2.1.3.4 Milling Time

The milling time is the most important parameter. Normally the time is so chosen as to achieve a steady state between the fracturing and cold welding of the powder particles. The times required vary depending on the type of mills used, the intensity of milling, the ball-to-powder ratio, and the temperature of milling. It should be noted that the level of contamination increases as the milling time is increased hence it is desirable that the powder is milled just for the required duration and not any longer.

## 2.1.3.5 Grinding Medium

The density of the grinding medium should be high enough so that the balls create enough impact force on the powder. It is always desirable to have the grinding vessel and the grinding medium made of the same material as the powder being milled to avoid cross contamination. The size of the grinding medium also has an influence on the milling efficiency. A larger size (and high density) of the grinding medium is useful since the larger weight of the balls will transfer more impact energy to the powder particles. It has been reported that the final constitution of the powder is dependent upon the size of the grinding medium used.

## 2.1.3.6 Ball-to-Powder Weight Ratio

The ratio of the weight of the balls to the powder (BPR), sometimes referred to as charge ratio (CR), is an important variable in the milling process. This has been varied by different investigators from a value as low as 1:1 to as high as 220:1. The higher the BPR, the shorter is the time required to achieve a particular phase in the powder being milled. At high BPR more energy is transferred to the powder particles and so alloying takes place faster. It is also possible that due to the higher energy, more heat is generated

and this could change the constitution of the powder. The amorphous phase may even crystallize if the temperature rise is substantial [Suryanarayana 2001].

## 2.1.3.7 Extent of Filling the Vial

Since alloying among the powder particles occurs due to the impact forces exerted on them, it is necessary that should be enough space for the balls and the powder particles to move around freely in the milling container.

## 2.1.3.8 Milling Atmosphere

The major effect of the milling atmosphere is on the contamination of the powder. Therefore, the powders are milled in the containers that have been either evacuated or filled with an inert gas such as argon or helium.

## 2.1.3.9 Process Control Agents

The powder particles get cold welded to each other, especially if they are ductile, due to the heavy plastic deformation experienced by them during milling. But, true alloying among powder particles can occur only when a balance is maintained between cold welding and fracturing of particles. A process control agent (PCA), also referred to as lubricant or surfactant, is added to the powder mixture during milling to reduce the effect of cold welding.

The PCAs can be solids, liquids or gasses. They are mostly organic compounds, which act as surface-active agents. The PCA adsorbs on the surface of the powder particles and minimizes cold welding between powder particles and thereby inhibits agglomeration. The surface-active agents adsorbed on particle surfaces interfere with cold welding and lower the surface tension of the solid material. Since the energy required for the physical process of size reduction, E is given by

$$E = \gamma * \Delta S \qquad\qquad (7)$$

Where $\gamma$ is the specific surface energy and $\Delta S$ is the increase of surface area, a reduction in surface energy results in the use of shorter milling times and/or generation of finer powders [Suryanarayana 2001].

A wide range of PCAs has been used in practice at a level of about 1-5 wt% of the total powder charge. The most important of the PCAs include stearic acid, hexane, methanol, ethanol, and acetone. The choice of a PCA for milling depends on the nature of the powder being milled and the purity of the final product desired.

## 2.1.3.10 Temperature of Milling

The temperature of milling is another important parameter in deciding the constitution of the milled powder. Since diffusion process are involved in the formation of alloy phases irrespective of whether the final product phase is a solid solution, intermetallics, nanostructure, or an amorphous phase, it is expected that the temperature of milling will have a significant effect in any alloy system.

During the formation of nanocrystals, it was reported that the root mean square (rms) strain in the material was lower and the grain size larger for materials milled at higher temperatures. The extent of solid solubility was reported to decrease at higher milling temperatures. For example, during planetary ball milling of a Cu-37at%Ag powder mixture, it was noted that a mixture of an amorphous and crystalline (supersaturated solid solution) phases was obtained on milling at room temperature; instead, only a Cu-8at%Ag solid solution was obtained on milling the powder at $200^0$C. Similar results were also reported in the Cu-Ag, Zr-Al, and Ni-Ag alloy systems and were explained on the basis of the increased diffusivity and equilibration effects at higher temperatures of milling.

## 2.1.4 Mechanism of Mechanical Alloying

During high-energy ball milling the powder particles are repeatedly flattened, cold-welded, fractured and rewelded. Whenever two steel balls collide, some amount of of powder is trapped in between them. Typically, around 1000 particles with an aggregate weight of about 0.2 mg are trapped during each collision. The force of the impact plastically deforms the powder particles leading to work hardening and fracture (Figure 2.2). The new surfaces created enable the particles to weld together and this leads to an increase in particle size. Since in the early stages of milling, the particles are soft (if we are using either ductile-ductile or ductile-brittle material combination), their tendency to weld together and form large particles is high. A broad range of particle sizes develops, with some as large as three times bigger than the starting particles. The composite particles at this stage have a characteristic layered structure consisting of various combinations of the starting constituents (Figure 2.3) [Suryanarayana 1999, 2001]. With continued deformation, the particles get work hardened and fracture by fatigue failure mechanism and/or by the fragmentation of fragile flakes.

Fragments generated by this mechanism may continue to reduce in size in the absence of strong agglomerating forces. At this stage, the tendency to fracture predominates over cold welding. Due to the continued impact of grinding balls, the structure of the particles is steadily refined, but the particle size continues to be the same. Consequently, the inter-layer spacing decreases and the number of layers in a particle increases. However, it should be noted that the efficiency of particle size reduction is very low, about 0.1% in a conventional ball mill. The efficiency may be somewhat higher in high-energy ball milling processes, but is still less than 1%. The remaining energy is lost mostly in the form of heat, but a small amount is also utilized in the elastic and plastic deformation of the powder particles.
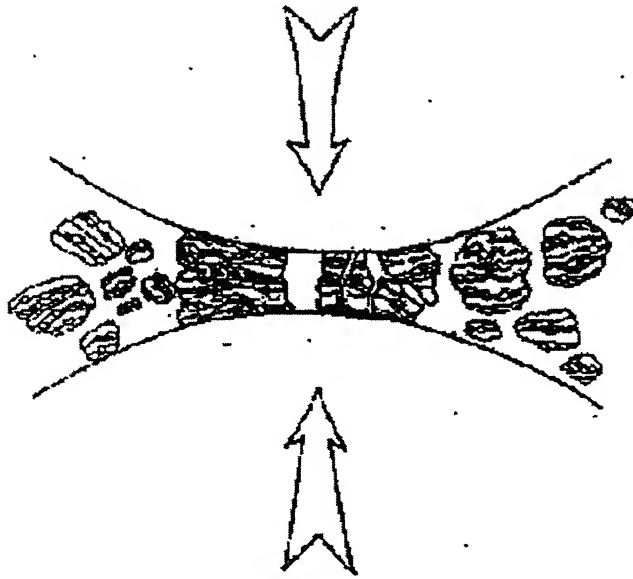
**Figure 2.2 Ball-powder-ball collision of powder mixture during mechanical alloying [Gilman and Benjamin 1983].**
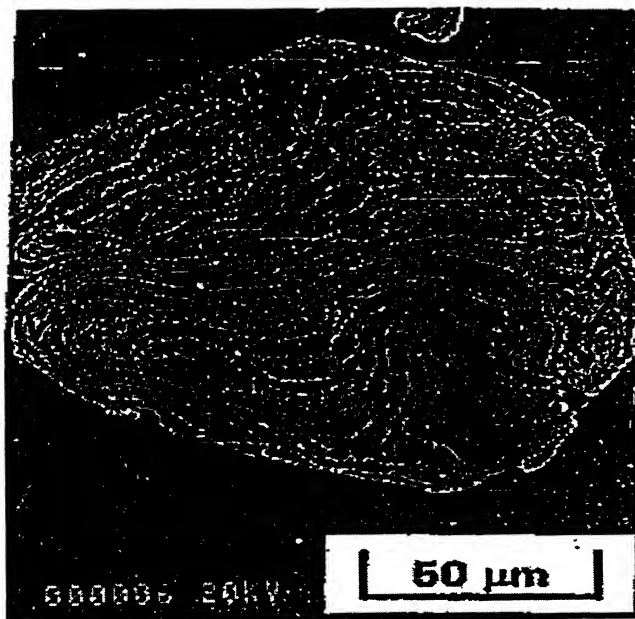


**Figure 2.3 Scanning electron micrograph depicting the convoluted lamellar structure o btained d uring m illing o f a d uctile-ductile c omponent s ystem ( Ag-Cu) [Suryanarayana 2001].**

51

After milling for a certain period of time, steady state equilibrium is attained when a balance is achieved between the rate of welding, which tends to increase the average particle size, and the rate of fracturing, which tend to decrease the average composite particles size. Smaller particles are able to withstand deformation without fracturing and tend to be welded in larger pieces, with an overall tendency to drive both very fine and very large particles towards an intermediate size. At this stage each particle contains substantially all of the starting ingredients, in the proportion they were mixed together and the particles reach saturation hardness due to the accumulation of strain energy. The particle size distribution at this stage is narrow, because particles larger than average are reduces in size at the same rate that fragments smaller than average grow through agglomeration of smaller particles (Figure 2.4).

From the foregoing it is clear that during MA, heavy deformation is introduced into the particles. This is manifested by the presence of a variety of crystal defects such as dislocations, vacancies, staking faults, and increased number of rain boundaries. The presence of this defect structure enhances the diffusivity of solute elements into the matrix. Further, the refined microstructural features decrease the diffusion distances. Additionally, the slight rise in temperature during milling further aids the diffusion behavior, and consequently, true alloying takes place amongst the constituent elements. While this alloying generally takes place nominally at room temperature, sometimes it may be necessary to anneal the mechanically alloyed powder at an elevated temperature for alloying to be achieved. This is particularly true when formation of intermetallics is desired.

The specific times required to develop a grain structure in any system would be a function of the initial particle size and characteristics of the ingredients as well as the specific equipment used for conducting the MA operation and the operating parameters of the equipment. But, in most of the cases, the rate of refinement of the internal structure (particles size, crystallite size, lamellar spacing, etc.) is roughly logarithmic with

processing time and therefore the size of the starting particles is relatively unimportant. In a few minutes to an hour, the lamellar spacing usually becomes small and the crystallite (or grain) size is refined to nanometer dimensions (Figure 2.5). The ease with which nanostructured material can be synthesized is one reason why MA has been extensively employed to produce Nanocrystalline materials.

## 2.1.5 Applications of Mechanical Alloying

The technique of MA has been shown to produce a variety of materials. The most important reason for the invention and development of the MA process was the production of oxide dispersion strengthened (ODS) materials in which fine particles of $Y_2O_3$ or $ThO_2$ were uniformly dispersed in a nickel or iron based super alloy. Investigations have revealed that MA can synthesize metastable phases such as super saturated solid solutions, nonequilibrium crystalline or quasicrystalline intermediate phases and amorphous alloys. In addition, nanostructures with a grain size of a few nanometers, typically <100nm, are produced. These metastable phases have interesting combinations of physical, chemical, mechanical, and magnetic properties and are being widely explored for potential applications.

Mechanically alloyed materials find applications in a variety of industries. The applications include synthesis and processing of advanced materials (magnetic materials, superconductors, and functional ceramics), intermetallics, nanocomposites, catalysts, hydrogen storage materials, food heaters, gas absorbers, and also in the modification of solubility of organic compounds, waste management, and production of fertilizers. But, the major applications of mechanically alloyed materials have been in the areas of thermal processing, glass processing, energy production, aerospace, and other industries [Suryanarayana 1999, 2001].
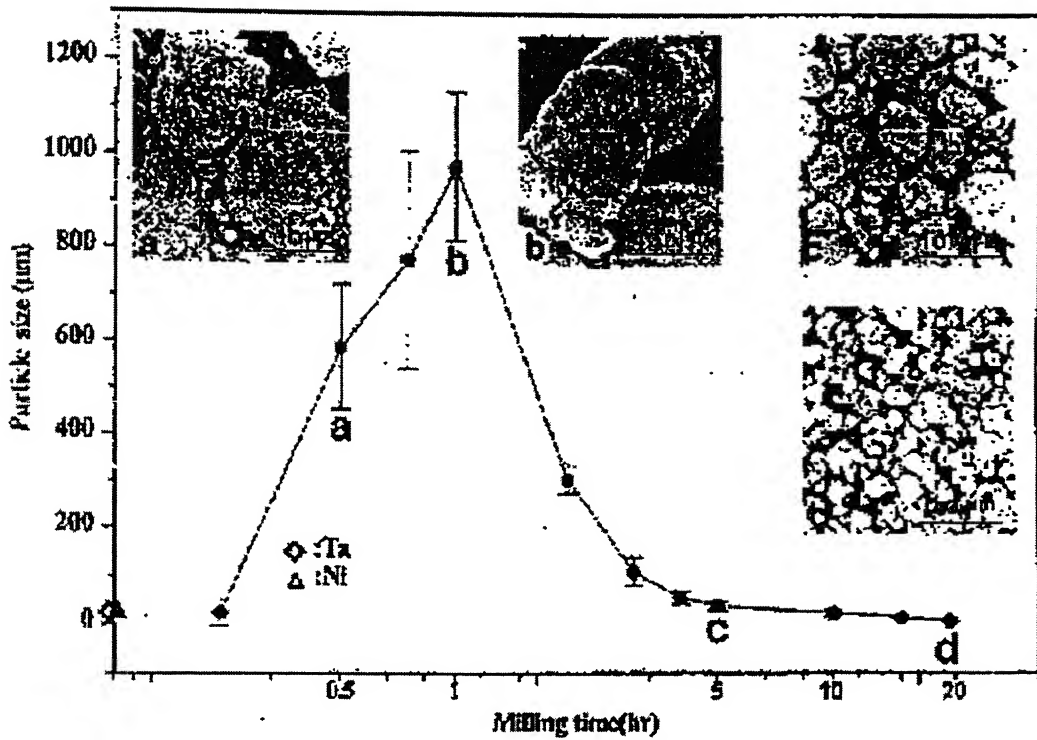
**Figure 2.4 Narrow particle size distribution caused by tendency of small particles to weld together and large particles to fracture under steady-state conditions [Suryanarayana 2001]**
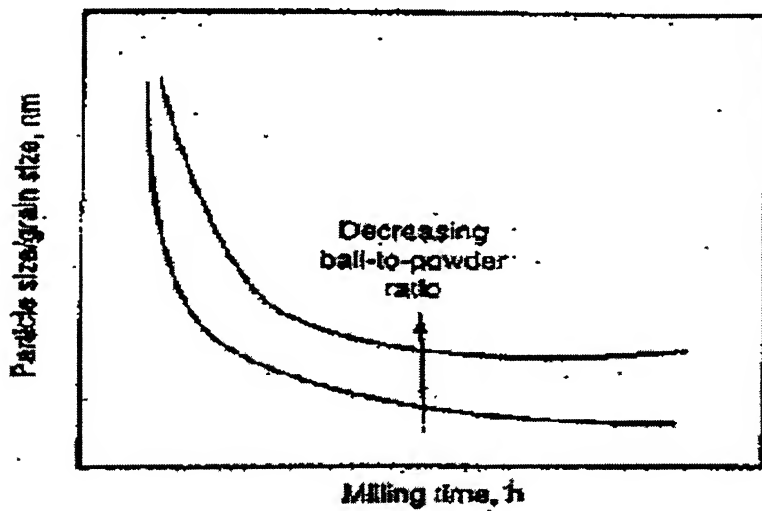


**Figure 2.5 Refinement of particle and grain sizes with milling time.**

## 2.2 EXPLOSIVE COMPACTION OF MA NANOCRYSTALLINE POWDER

Explosive consolidation proceeds with the passage of a large-amplitude compressive stress generated by plate impact or explosive without any external heating. The peak pressure values may be on the order of tens of GPa, thus providing densification by plastic yielding for both metals and ceramics [Groza 1999, Glade and Thadani 1995, Kondo 1990]. Localized heating possibly up to melting temperatures due to particle friction occurs and enables good interparticle bonding. The major drawback in the explosive consolidation is the difficult coordination of the short stress and heat application events that result in frequent specimen fracture.

In nanosize powders the heat may transfer throughout the entire particle, thus providing an advantage over coarser materials where the heating is only superficial. Best results are achieved when high temperatures are reached before the shockwave passes. If particles are heated, they may deform rather than fracture upon stress application. This very short high temperature exposure provides the best means to retain fine grain size or far from equilibrium conditions such as amorphous structures, or supersaturated solid solutions. Full densification has been reported in explosive compacted mechanically alloyed TiAl specimens with final grain sizes of 15nm. These latter results have been compared with HIPping that provided full consolidation at 1075 K/207Mpa/2h but grain sizes were about 100 nm [Suryanarayana 1997].

Nanocrystalline metal powders synthesized by mechanical alloying in a ball mill result in micron sized powder particles with a nanosized substructure. Conventional consolidation methods result in considerable coarsening of the metastable nanometer crystallites, but dynamic consolidation of these powders using explosive technique produce fully dense monoliths while retaining the nanometer substructure. Numerical modeling, used to guide the experimental phase, revealed that the compression wave necessary for suitable consolidation was of the order of 10 GPa for a few tenths of a microsecond.

Korth and Williamson (1995) have explained the process of Dynamic compaction while performing few experiments in which the powders were compacted by double tube technique. In this technique, the dynamic consolidation is performed in a cylindrical geometry using an explosive. The powder is pressed into a stainless steel container tube to a density of approximately 60% of theoretical. A stainless steel driver tube is placed concentrically around the container tube, leaving an annular gap. A slurry explosive, contained in an acrylic or aluminum tube surrounding the driver tube, is detonated from one end of the apparatus. As the detonation front sweeps down the axis of the assembly, the driver tube is accelerated inward to impact the container tube, producing a shock wave that progresses into the powder sample. Thus, the powder densifying compression wave is generated from the metal-to-metal impact of the two tubes rather than from a direct coupling with the explosive. The densification/consolidation event occurred in the time frame of a few microseconds.

The double tube technique for dynamic consolidation of powders, which is described above, is generally used because it allows more flexibility in adjusting the magnitude and duration of the compression wave than would be possible direct coupling with the explosive (i.e. eliminating the driver tube). Using a direct coupling method, the pressure wave into the container tube and powder is dictated by the detonation pressure (Chapman-Jouguet pressure) peculiar to the explosive being used. The duration of the pressure pulse can be modified somewhat by using more explosive, and thereby changing the shape of the release wave (Taylor wave), but the peak pressure can only changed by selecting another explosive with a different detonation pressure. In the case of double-tube method, the shock pressure can be changed quite readily by varying the impact velocity of the driver tube, which is accomplished by varying the mass ratio of the explosive and the driver tube. The duration of the compression wave is governed by the driver tube wall thickness.

As the pressure wave first enters the powder, it has a magnitude of about 11 GPa. The pressure gradually decays to approximately 5GPa at midradius, as the energy is partially consumed in the densification process, and then increases quite markedly as the wave

converges towards the axis of symmetry. If the densification pressure is too high, it appears to lead to excessive bulk temperatures which result in grain coarsening and material softening.

It is believed that explosive consolidation was the most successful method used in preserving the metastable nanostructure due to the short duration of pressure application. Pressure pulses were seen in this process to be only a few tenths of a microsecond in duration. Even though large temperatures (above melting) were generated by the high-strain-rate deformation as the interparticle voids collapsed, the temperature excursions were confined to the particle surfaces and rapidly quenched by the particle interiors [Williamson and Berry 1986].

Particle level analysis of other materials have shown the interparticle temperature spike to be only a few tenths of a microsecond in duration, which would severely limit any diffusional processes required for grain growth. In addition to retention of the nanosized grains, hardness measurements were also observed to be retained during the dynamic consolidation in the Fe-base material.
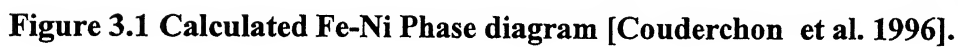
# *CHAPTER 3*

## 3. Ni-Fe AND Ni-Fe-Co SYSTEM

### 3.1 Fe-Ni SYSTEM

The calculated phase diagram for the Ni-Fe system is shown in Figure 3.1. The two elements are close together in the periodic Table and are chemically similar, with almost identical electronic structures. The behavior of their alloys could therefore be expected to be quite straightforward. However the behavior of these alloys is complex, due to the fact that iron and nickel are both ferromagnetic transition elements. Both these elements together with Co show the characteristic properties of this group (Table 3.1).This is essentially due to the fact that the 4 s electron shell is occupied without the 3 d orbital being completely filled. In the solid state, this leads to a narrow 3d band in which the electrons are mainly localized, together with a high density of states close to the Fermi level. This particular electronic structure gives rise to a number of general characteristics in the transition elements such as strong cohesion, relatively high electrical Resistivity and variable chemical behavior. In some cases, it also leads to some curious effects such as the appearance of magnetic order, causing either ferromagnetism (α-Fe, Co, Ni) or antiferromagnetism (Cr, Mn, γ-Fe) [Rosenberg 1968, Couderchon et al.1996].

### 3.1.1 Crystal Structure of the Fe-Ni Alloys

The FCC phase exists over a wide concentration field, ranging from pure nickel to 27% Ni at room temperature (Figure 3.2). Below 27% Ni, the number of electron per atoms is no longer sufficient for the f.c.c. structure to remain the only stable phase, and it is gradually replaced by the b.c.c. lattice. For Nickel content greater than 27%, the stability of the f.c.c. structure offers a number of advantages. It provides high ductility, enabling the alloy to be rolled down to very small thickness, of the order of 10 μm.

**Figure 3.1 Calculated Fe-Ni Phase diagram [Couderchon et al. 1996].**



**Figure 3.2 Fe-Ni binary phase diagram**

The absence of a ductile-brittle transition at low temperatures makes it possible to use these materials at cryogenic temperatures (Invar for LNG tankers). Finally, heat treatment can be performed at all temperatures without the complication of phase transformations. This is extremely useful for developing recrystallization textures or exceptional magnetic properties.

One of the simplest consequences of the stability of f.c.c. phase in Fe-Ni alloys is that their lattice parameters and densities obey the rule of mixtures over a wide range of compositions, from pure Nickel to 40% Nickel (Figure 3.3). However, below 40% Ni, the situation becomes much more complicated, since the normal variation of lattice parameter with composition is accompanied by a more unusual and quite unexpected effect of temperature [Couderchon et al. 1996].

## 3.1.2 Electromagnetic Properties of Ni-Fe Alloys

The Ni-Fe alloys are ferromagnetic throughout the range of concentrations, and their original electromagnetic behavior has led to a wide variety of soft magnetic materials. The variations of their electromagnetic characteristics (Ms, etc) with parameters such as composition, microstructure and temperature have natural repercussions on their functional properties, particularly on the most commonly used one, the relative permeability $\mu$. It is given by

$$\mu = B/ (\mu_0 H) \qquad \ldots\ldots\ldots\ldots (8)$$

Where B is the induction, H is the field strength and $\mu_0$ is the permeability of vacuum.

In weakly anisotropic materials such as the Ni-Fe alloys, the permeability $\mu_z$ for the usual case of AC operation can be written as

$$1/ \mu_z \approx [\{(b+K_u+ (3/2\lambda\sigma))^{1/2}\}/AM_s] +(16fdl/\pi^2\rho) \qquad \ldots\ldots\ldots\ldots(9)$$
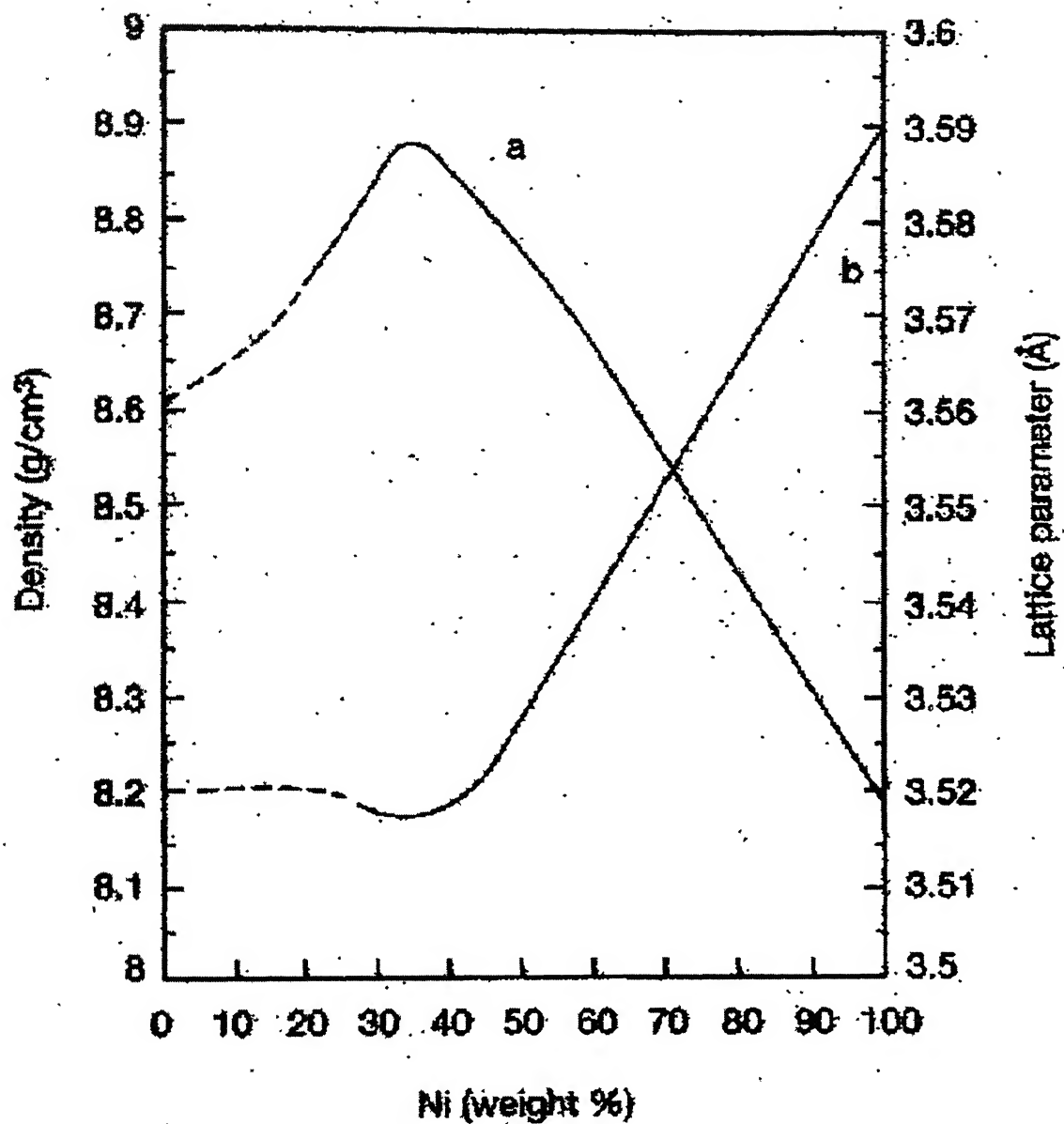
Figure 3.3 Effect of composition on (a) lattice parameter and (b) density in Fe-Ni alloys at $20^0$ C

where, Ms is the saturation magnetization, corresponding to the maximum magnetic flux which the material can transport, $\rho$ is the electrical Resistivity which limits eddy current losses during AC operation and therefore improves the efficiency of electromagnetic energy exchanges, $K_1$ and $K_u$ are the magnetocrystalline and induced (unidirectional) magnetic anisotropies via which the magnetic structure can be adapted, $\lambda$ is the magnetostriction, which accounts for the effect of stress $\sigma$, b is the magnetostatic energy term which takes into account the effects of precipitates, grain boundaries, etc., f is the operating frequency, d is the strip thickness, l is the width of the magnetic domains and A is a constant [Couderchon et al. 1996].

The simplified relation shows that, in addition to the stability of ferromagnetism ($M_s$ and $T_c$) four major parameters ($\rho$, $K_1$, $K_u$, $\lambda$) determine the functional magnetic properties of commercial alloys. For high permeability, it can be seen that $M_s$ and $\rho$ must be as large as possible and $K_1$, $K_u$, and $\lambda$ as small as possible.

## 3.1.2.1 Ferromagnetism of Ni-Fe Alloys

When iron, with 2.2 Bohr magnetrons ($\mu_B$), per atom, i.e. $M_s = 2.1T$, and a Curie point of $770^0C$ is added to nickel, which has only 0.6 $\mu_B$ per atom and a curie point of $358^0C$, it is to be expected that the saturation magnetization and curie point will be increased and this is indeed observed, as shown in Figure 3.4. The fall in Curie point beyond 30-40% indicates that the ferromagnetic coupling gradually weakens above this concentration, and it should be noted that this behavior correspondence to the change in sign of the spontaneous volume magnetostriction (Figure 3.5).

The increase in saturation magnetization with iron content is linear up to about 60% Fe, as predicted by the band theory of magnetism. However, the behavior deviates slightly from linearity beyond 50% Fe, and becomes frankly anomalous on approaching the invar composition (64%Fe). Between 40 and 25% Ni, it is as though not only does the ferromagnetic coupling disappear, but also, at the same time, the magnetization of the
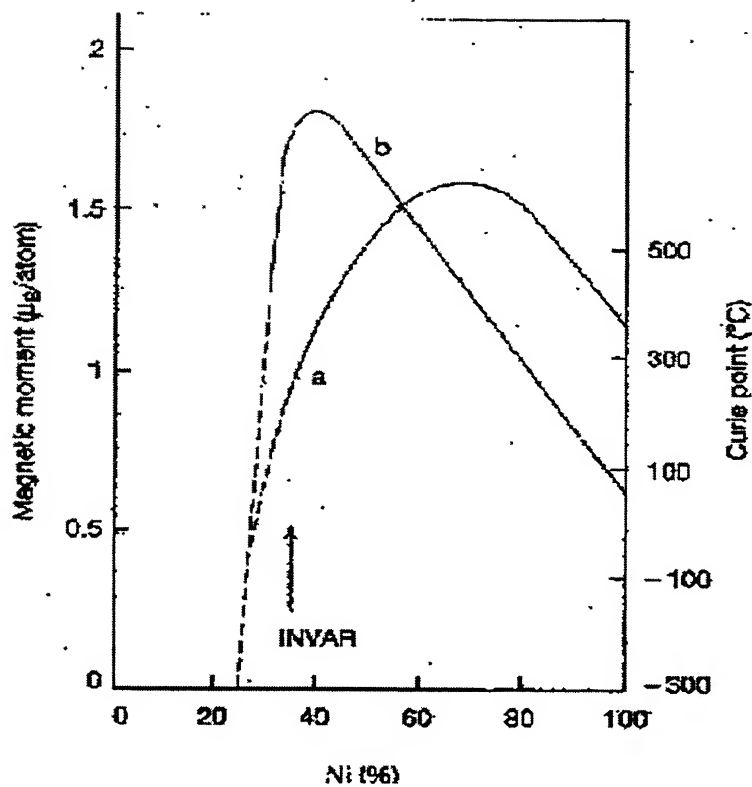
**Figure 3.4 Variation of the Curie point and magnetic moment in Fe-Ni alloys [Nakamura 1976].**
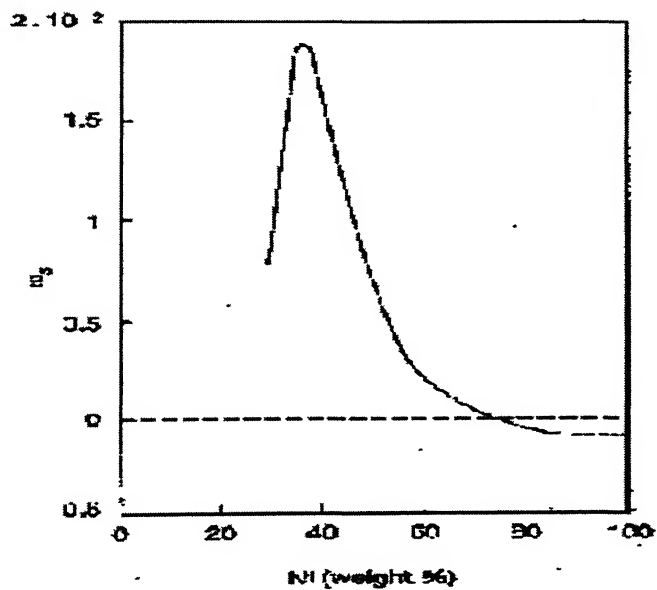


**Figure 3.5 Spontaneous volume magnetostriction of Fe-Ni alloys at 0K [Nakamura 1976].**

material vanishes. This can be due to the tendencies for local antiferromagnetic coupling. Another possibility is that the magnetic moments decrease at a specific electron concentration [Rosenberg 1968, Couderchon et al. 1996].

### 3.1.2.2 Electrical Resistivity of Fe-Ni Alloys

The electrical resistivity increases with temperature and with the presence of irregularities in the crystal lattice (foreign atoms, differences in magnetic moments, etc.,) since these factors disturb the propagation of conduction electrons. The resistivity near room temperature increases rapidly as the iron content increases above 50%, reaching a maximum in the region of the invar composition [Couderchon et al.1996]. This abnormal increase in the resistivity is a consequence of the highly disturbed magnetic state in this range of concentrations.

### 3.1.2.3 Magnetic Anisotropy in Fe-Ni Alloys

Equation (9) shows that, neglecting complications due to inevitable eddy currents, the permeability of Fe-Ni alloys depend essentially on two factors. Firstly, micro-structural features, such as non-magnetic precipitate particles, grain boundaries, etc., disturb the induced magnetic flux lines, creating magnetostatic energy of density b. in order to magnetize the material, the magnetizing field must expand this energy. It can be reduced essentially by careful control of the melting, working and heat treatment processes. Secondly, the term $(K_l+K_u+\lambda\delta)$ corresponds to the sum of the different anisotropies in the crystal environment, which exert an influence on the local magnetization of the material [Couderchon 1996]. In fact ferromagnetic lattices are naturally high anisotropic, and the effect sometimes can be enhanced by external factors such as stresses, magnetic field annealing, recrystallization, etc.

## 3.1.2.4 High Permeability of 80Ni-20Fe Alloys

In the binary 80Ni-20Fe alloys with around 80%Ni, the magneto-crystalline anisotropy Kl and the magnetostriction do not vanish exactly at the same composition, so that it is not possible to obtain a total anisotropy of zero. Moreover, these alloys have two additional disadvantages. Firstly, their electrical resistivity is only moderate and is insufficient for ac applications. Secondly, the ordering reaction occurs too rapidly for it to be readily controlled during industrial heat treatments. Empirical solutions have been obtained for most of these problems, and consist in adding a small amount (3-6%) of Cr or Mo, sometimes combined with copper. As expected these element increase the resistivity and retard ordering but also have more unexpected effects. In particular, they shift the composition, where $K_1$ falls to zero, and with an appropriate choice for additions it becomes possible to make it coincide with that for the magnetostriction.

In order to make use of these complex behaviors, it is necessary to finally adjust both the alloy chemistry and the heat treatments. By combining particular composition with appropriate heat treatments, it is possible to obtain a family of alloys whose range of properties covers the requirement of a wide variety of applications [Couderchon et al.1996].

## 3.1.3 Applications

The Fe-Ni alloys have the highest known permeability for sintered soft magnetic materials, particularly Fe-80%Ni, which can give a maximum permeability of 95,000 with a coercive force of only 0.02 A/cm. the very high permeability and very low coercive force of Fe-Ni alloys make them suitable for use in circuits that are excited by very low currents and require quick response [Bas et al. 2003]. There are many other applications of these alloys. In color television, they are found in the electron guns and in the color-separating grid known as the shadow mask. They line the insides of the gigantic tanks of LNG tankers. They are present in watches, integrated circuits, automobiles,

electricity grids, regulating devices, measuring instruments, telecommunications, domestic appliances and many other applications [Tiers 1996].

## 3.2 THE Fe-Ni-Co SYSTEM

In a critical analysis of experimental results concerning the Fe-Ni-Co system, Raynor et al. (1988) present a liquidus projection derived from the work of Kase (1927) and combine it with data for the constituent binary systems. The only information available for the solid state concerns the phase boundaries between the b.c.c. and f.c.c. phases in the temperature range 650-800$^0$C, determined by Koster et al. (1969) and later by Widge et al. (1977). At lower temperatures (400$^0$C), Viting (1957) determined the range of existence of the ordered $Ni_3Fe$ and austenite phases [Ansara 1996].

Fernandez-Guillermet (1989) evaluated the parameters of the thermodynamics functions of the different phases in the Co-Ni and Co-Fe binary systems, together with those for the ternary system, but did not determine the corresponding parameters for the formation of the $L1_2$ ordered $Ni_3Fe$ phase. The 427$^0$C isothermal section of the ternary diagram is shown in Figure 3.6 and 3.7, while that calculated for 140$^0$C is illustrated in Figure 3.8. At 427$^0$C, in the iron rich region, at very low cobalt contents, a narrow two phase region occurs, where the paramagnetic and ferromagnetic f.c.c. structures coexist. This field disappears at lower temperatures, where it is replaced by equilibrium between the b.c.c. structure and $Ni_3Fe$, as can be seen in the 140$^0$C section [Ansara 1996].
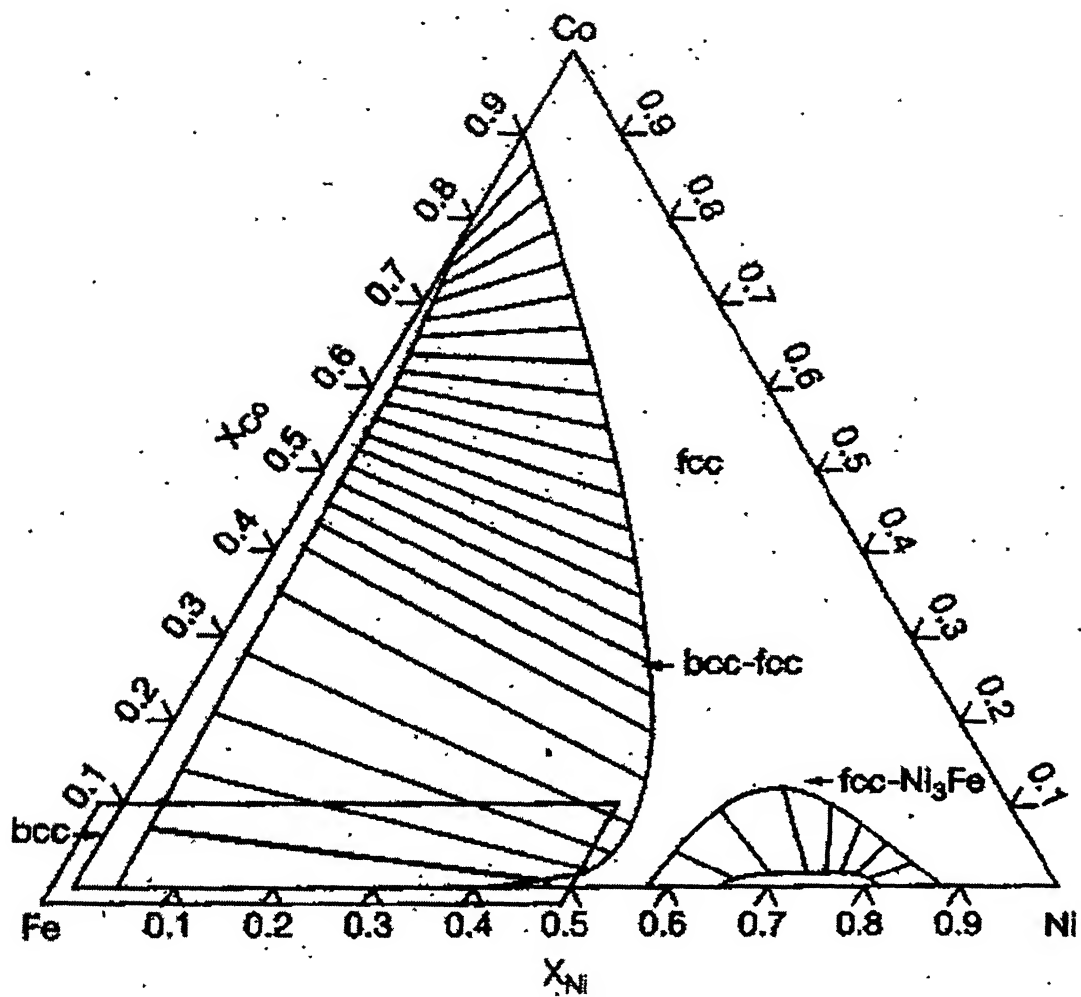
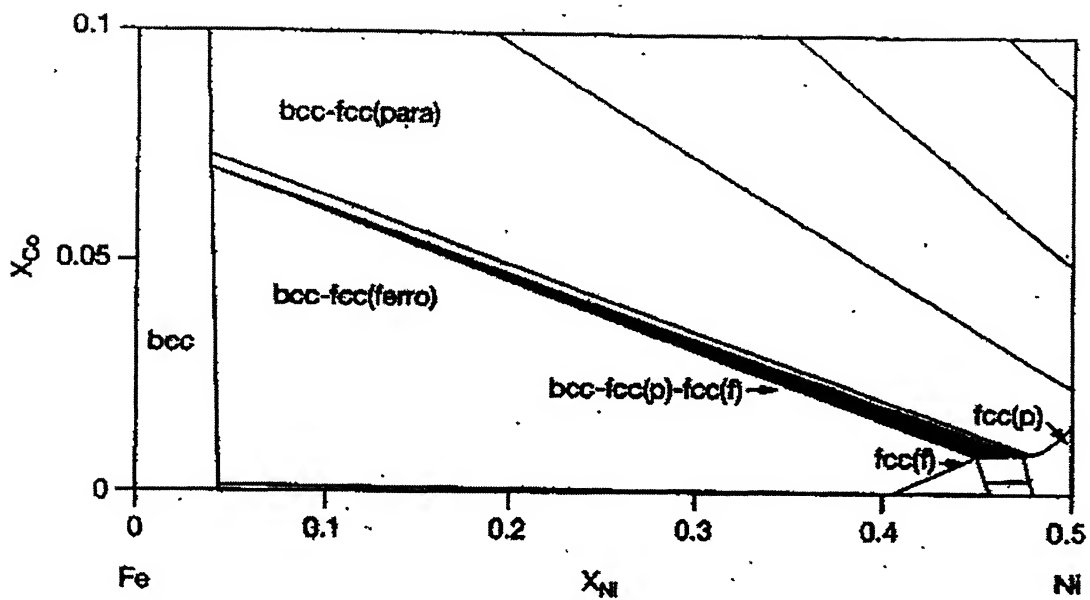Figure 3.6 Calculated $427^0C$ isothermal section of the Fe-Ni-Co system.

**Figure 3.7 Iron-rich region of the calculated $427^0C$ isothermal section of the Fe-Ni-Co system.**
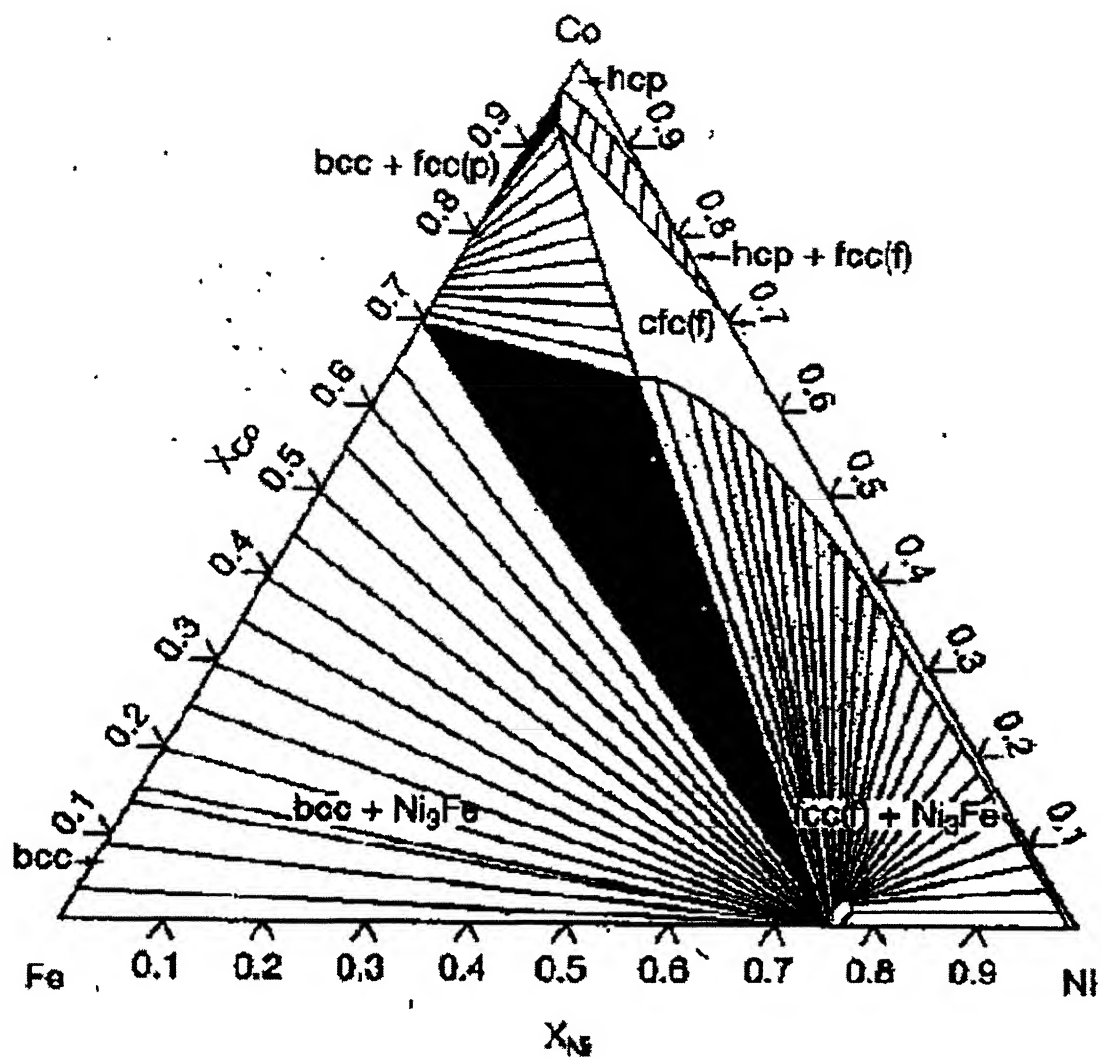
**Figure 3.8 Calculated $140^{0}C$ isothermal section of the Ni-Fe-Co system.**

## 3.2.1 Applications

The ternary alloy Cobalt-Iron-Nickel is a good candidate for soft magnetic high frequency applications, because in contrast to Permalloy, the saturation magnetization in this alloy can be made high, 2.1T [Voorthuysen 2002]. Ni-Fe-Co alloys are commonly used in magneto-electronic devices. In particular, for high density magnetic random access memories (MRAM), it is advantageous to use very thin magnetic films from the stand point of minimizing the demagnetizing field in the devices and maintaining low switching fields required for device operation. Ni-Fe-Co has been used extensively as active magnetic film in giant magneto-resistance (GMR) spin valves and MTJs [Ingvarsson 2002]. Magnetic multilayer thin films based on giant magneto-resistance effect are the basis of extremely high density (>10Gbit/square inch) data storage systems [Jung 1999].

# CHAPTER 4

## 4. OBJECTIVE OF THE PRESENT INVESTIGATION

The p resent i nvestigation i s a imed a t p roducing n anocrystalline 8 0Ni-15Fe-5Co ( wt%) powder via mechanical alloying process by using a laboratory scale Planetary mill for milling and its processing into bulk compacted samples via Explosive Compaction technique. Scanning Electron Microscopy (SEM), Transmission Electron Microscopy (TEM) and X-Ray diffraction techniques have been used for the characterization of the material. The saturation magnetization and Curie temperature have been determined by Vibrating Sample Magnetometer (VSM) technique.

# CHAPTER 5

# 5. EXPERIMENTAL PROCEDURE

## 5.1 RAW MATERIAL

### 5.1.1 Iron Powder

Electrolytic iron powder supplied by M/S Sudhakar Products Bombay was used. The particle size determination of the powder was carried out in laser particle size analyzer and Median particle size of the powder was estimated around 89.0 μm as shown in Table 5.1. The powder morphology of as received iron powder is shown in Figures 5.1a-5.1b, whereas the size distribution of electrolytic iron powder, as determined by laser particle size analyzer, is shown in Figure 5.1c.
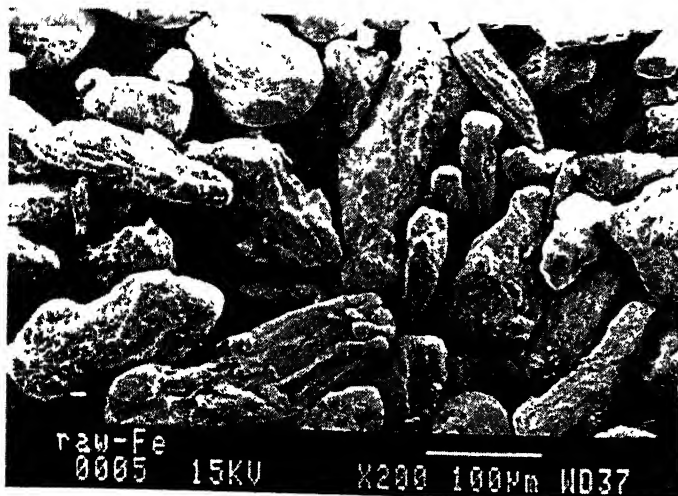
### 5.1.2 Nickel Powder

INCO type-123 nickel powder was used. This was produced by carbonyl process. The particle size determination of the powder was carried out in laser particle size analyzer and Median particle size of the powder was estimated around 9.0 μm as shown in Table 5.1. The powder morphology of as received Nickel powder is shown in Figures 5.2a-5.2b, whereas the size distribution of Nickel powder, as determined by laser particle size analyzer, is shown in Figure 5.2c.

### 5.1.3 Cobalt Powder

EFP grade Cobalt powder supplied by M/S Union Miniere- Cobalt and Energy Products, Belgium was used. The supplier provided the following characteristics of the EFP Cobalt powder: Chemical composition – 99.9 wt% Co, 0.4 wt% $O_2$, 0.5 wt% $H_2$ loss, and 120 ppm C.; Theoretical density = 8.9 gm/cc, Apparent density = 1.0 gm/cc, Tap density = 2.1 gm/cc, Average particle size (Fisher sub-sieve analysis) = 2.1 μm, Average particle size, $d_{50}$ = 3.9 μm, Specific surface area = 1.0 $m^2$/g.

**Table 5.1: Particle size determination of raw Ni, Fe, Co and milled 80Ni-15Fe-5Co powders by Laser Particle Size Analyzer**
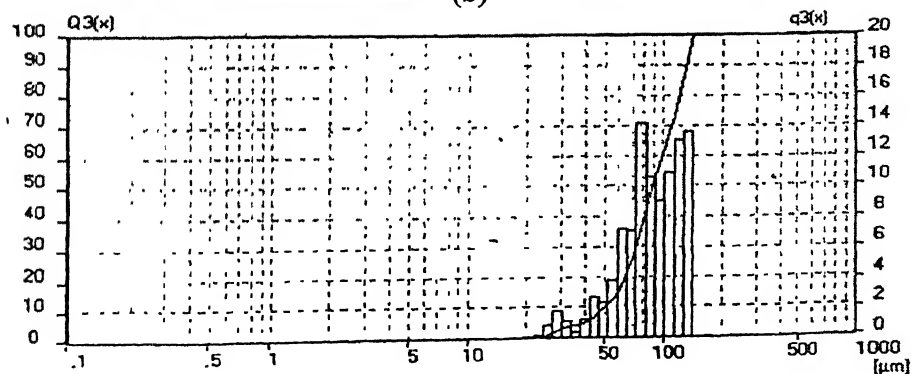
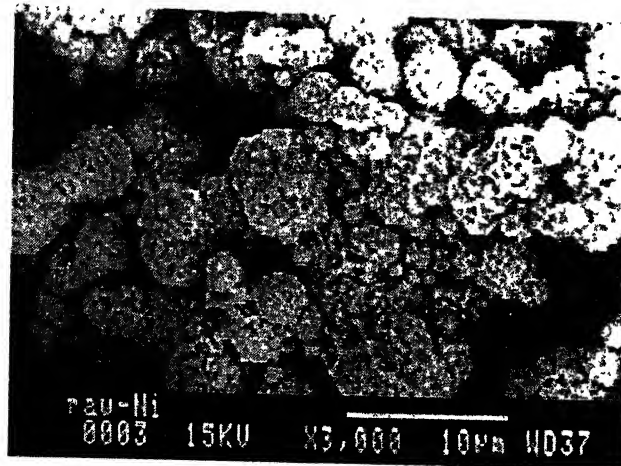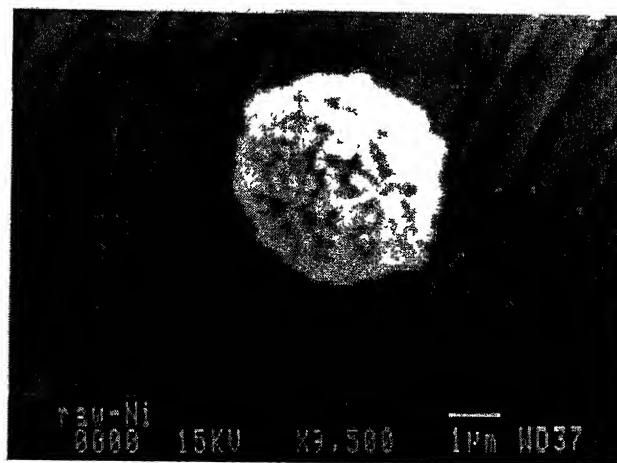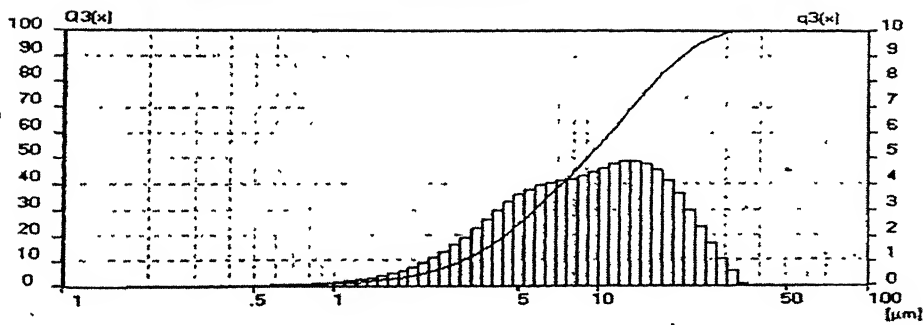| Powder Sample | Median Particle Size ($\mu$m) |
|---|---|
| Nickel | 9.0 |
| Iron | 89.0 |
| Cobalt | 10.0 |
| MA 80Ni-15Fe-5Co (125 hrs milled) | 7.0 |

(a)
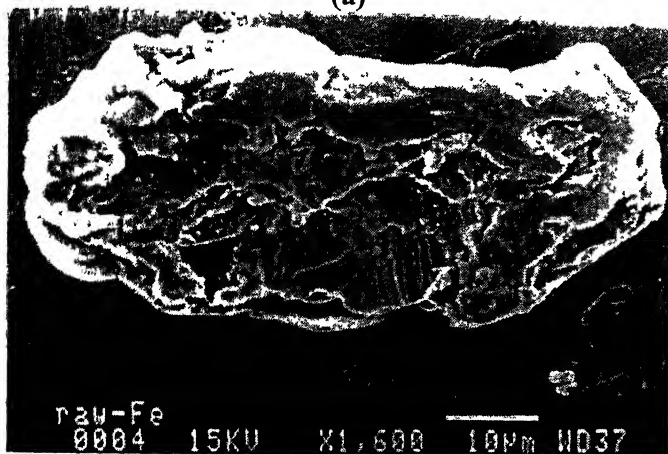


(b)



(c)

Figure 5.1 (a) & (b) Powder morphology of as received iron powder (c) Size distribution of electrolytic Iron powder
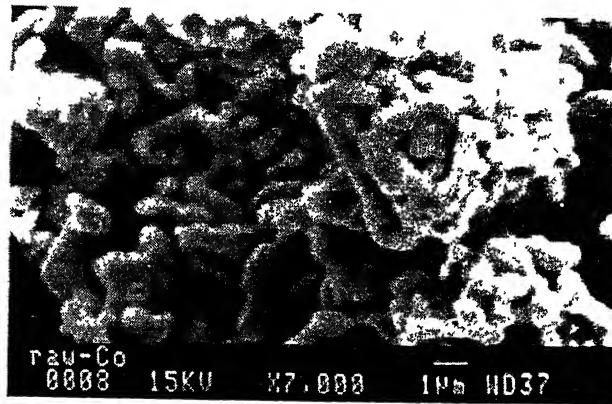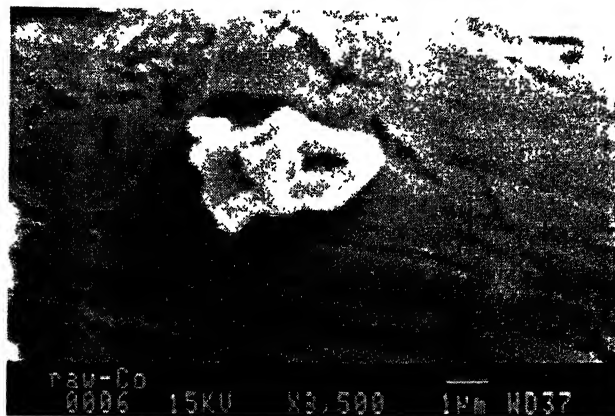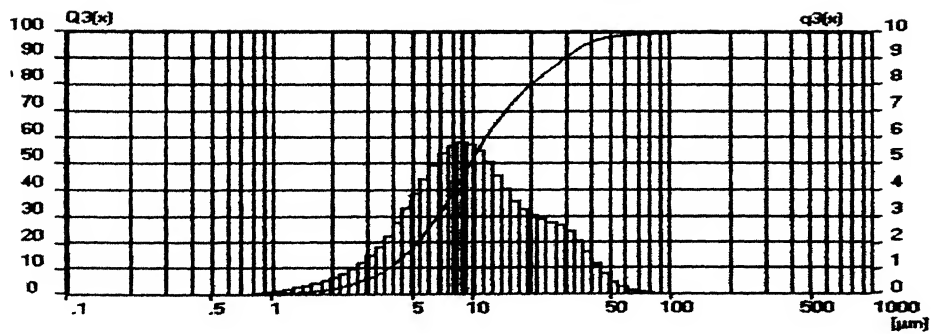
(a)



(b)



(c)

**Figure 5.2 (a) & (b) Powder morphology of as received Nickel powder (c) Size distribution of Nickel powder**

(a)



(b)



(c)

Figure 5.3 (a) & (b) Powder morphology of as received Cobalt powder (c) Size distribution of Cobalt powder

The particle size of the powder was also determined in the Lab using laser particle size analyzer and Median particle size of the powder was found to be around 10.0 μm, as shown in Table 5.1. The powder morphology of as received Cobalt powder is shown in Figures 5.3a-5.3b, whereas the size distribution of Cobalt powder, as determined by laser particle size analyzer, is shown in Figure 5.3c.

### 5.1.4 Gases

IOLAR-2 grade argon, nitrogen and hydrogen gases were used in the present work.

### 5.2 PREPARATION OF NANOCRYSTALLINE 80Ni-15Fe-5Co POWDER BY MECHANICAL ALLOYING

To start with, Ni, Fe, and Co powders were reduced by placing them in reducing atmosphere, by passing Hydrogen gas in atmosphere controlled furnace, at $690^0$C for 30 minutes to reduce any oxide present in the powders. The Nickel, Iron, and Cobalt powders were blended in the ratio 80Ni-15Fe-5Co (wt %) and were milled in a high-energy ball mill (Fritsch Pulverisette, planetary ball mill with two bowls) to produce nanocrystalline Ni-Fe-Co (16:3:1) at a disc rotation speed of 450 r.p.m. and disc to vial coupling ratio of 1:2. High Ni-Cr steel vials were given one trial run so that a thin coating of Ni-Fe-Co (16:3:1) was formed on the vial as well as high Ni-Cr steel balls.

This minimizes the contamination during mechanical alloying. The ball to powder ratio (BPR) was maintained at 4:1. In order to avoid agglomeration, wet milling was carried out using acetone as suspension media. The lids of the vials were tightly closed to isolate the system from the atmosphere. After different time intervals of milling, samples were taken from the vials for further investigations. Powder mix milled for 125 hours was taken for final processing and analysis. The particle size determination of the powder was carried out in laser particle size analyzer and Median Particle size of the powder was obtained around 7.0 μm as shown in Table 5.1. The morphology of 125 hr milled 80Ni-15Fe-5Co powder is shown in Figures 5.4a-5.4b whereas the size distribution of the milled powder, as determined by laser particle size analyzer, is shown in Figure 5.4c.
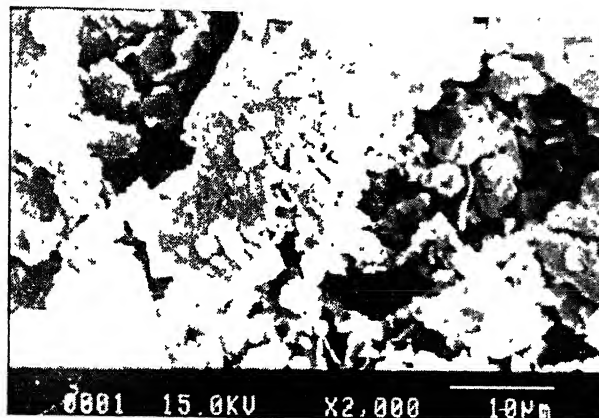
(a)
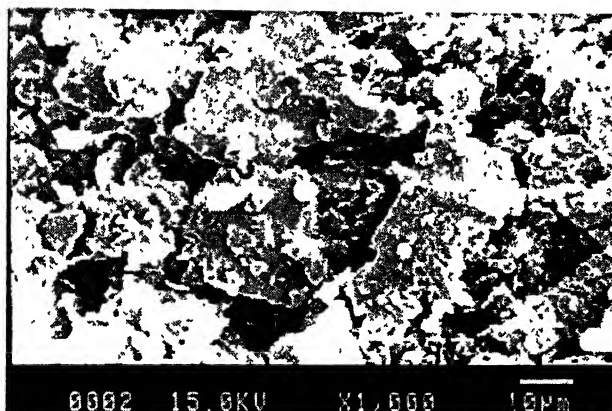


(b)
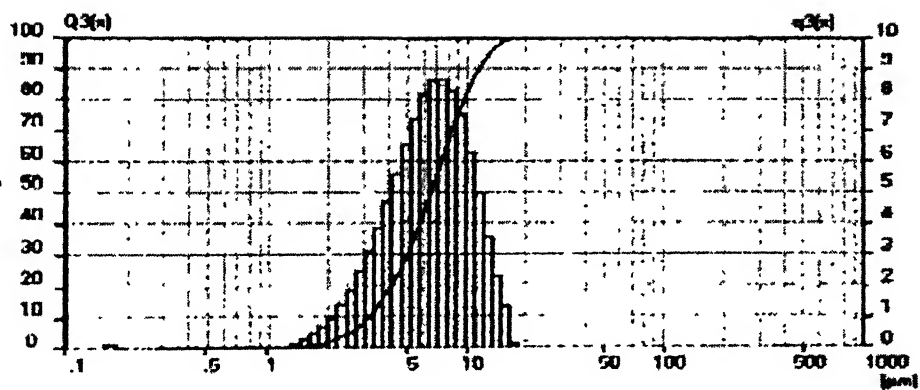


(c)

Figure 5.4 (a) & (b) Morphology of 125 hr milled 80Ni-15Fe-5Co powder (c) Size
distribution of 125 hr milled 80Ni-15Fe-5Co powder

## 5.3 CONSOLIDATION OF MA 80Ni-15Fe-5Co POWDER

It is expected that nanostructured 80Ni-15Fe-5Co powder would be obtained from mechanical alloying (MA) process. Consolidation of powders requires sintering, which is usually done at a temperature equal to 0.8 Tm (where, Tm is the melting point of the powder in Kelvin). Thus during consolidation of mechanically alloyed powder grain growth would take place. If proper care is not taken then nanocrystallinity may be destroyed during the process due to grain growth. Thus every effort must be made to choose a processing route, in particular temperature and number of unit steps, in such a way that the grain growth is minimized.

The melting points of Ni, Fe, and Co are 1728K, 1812K and 1768K respectively. Thus a temperature of about 1400K would be suitable for sintering such a powder. The following route was adopted to make bulk sample from mechanically alloyed 80Ni-15Fe-5Co powder in the present investigation.

MA 80Ni-1Fe-5Co powder ⟶ Annealing of MA powder at 200$^0$C for 15 minutes in reducing atmosphere (Hydrogen gas) ⟶ Explosive Compaction

Powder was annealed to remove stresses developed in the powder particles during milling as well as to remove any moisture content present in the milled powder. It can be clearly seen that explosive compaction is a one-step process which minimizes any kind of grain growth. In Explosive Compaction high pressure and high temperature are generated which is prerequisite for good compaction. Since high temperature and high pressure are generated for **one tenth of a microsecond time period,** there is no possibility of extensive grain growth.

## 5.3.1 Preparation of Bulk Sample of nanocrystalline 80Ni-15Fe-5Co via Explosive Compaction

At first, mechanically alloyed 80Ni-15Fe-5Co powder was annealed in reducing atmosphere ($H_2$) at $200^0C$ for 15 minutes to remove any moisture content present as well as to remove internal stresses introduced in particles due to milling. The powder was put in the mild steel containers, called Ampule, and was tapped gently for 1 hour so that powder particles settle down properly and no void remains inside the powder mass. After tapping, the ampules were closed by putting conical stopper (upper plug) at the top of the ampules.

Finally conical stopper (upper plug) was pressed little a bit to make powder mass more compacted inside the ampule. Each ampule was fixed on a circular wooden disc, which is used as a base, and then this arrangement was placed inside a cylindrical container (Explosive container). These explosive containers were made of aluminum and acrylic. Slurry explosive was then filled in the explosive container. The whole assembly was then put into a pit dug on the earth and then the pit was filled with soil and dust. Finally, the pit was closed by putting a heavy iron sheet at the opening of the pit. The explosive compaction arrangement is shown in Figure 5.5. Conditions, under which the explosive compaction process was conducted, are shown in Table 5.2.

Now the slurry explosive, contained in an acrylic or cardboard tube surrounding the ampule, was detonated from one end of the apparatus. After detonation the ampules were recovered (Figure 5.6a and 5.6b) and machined to take out the compacted samples. Cylindrical compacted samples were recovered after machining.
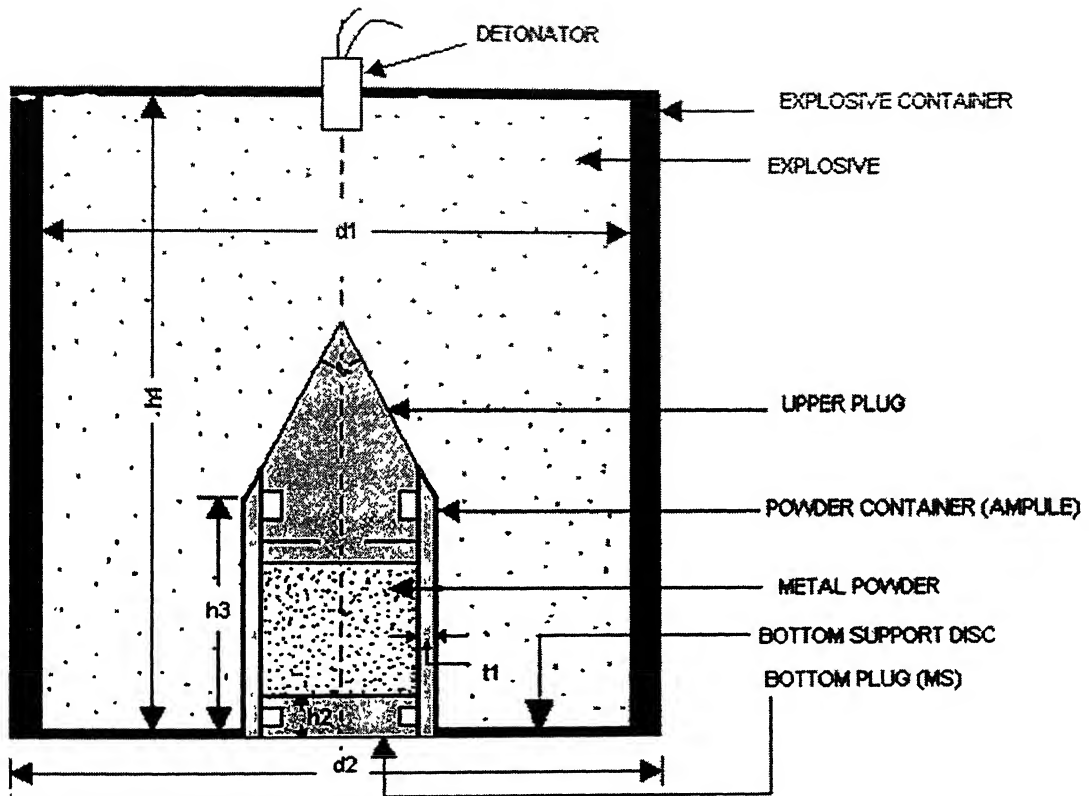
Figure 5.5 Schematic diagram of explosive compaction arrangement where,

d1 = 67 mm, d2 = 62 mm, h1 = 70 mm, h2 = 12.8 mm, h3 = 39 mm, t1 = 1 mm and $\alpha = 80^0$

**Table 5.2 Parameters during the explosive compaction experiments**

| Sample Designation | Explosive Used | Wall Thickness Of Ampule (mm) | Initial Packing Density of Powder (gm/cc) | Internal Dia. Of Explosive Cylinder (mm) |
|---|---|---|---|---|
| TBRL2 | ANFO (150 gms) | 1.00 | 3.670 | 62.00 |
| TBRL3 | TRIMONITE (160 gms) | 1.00 | 3.596 | 62.00 |
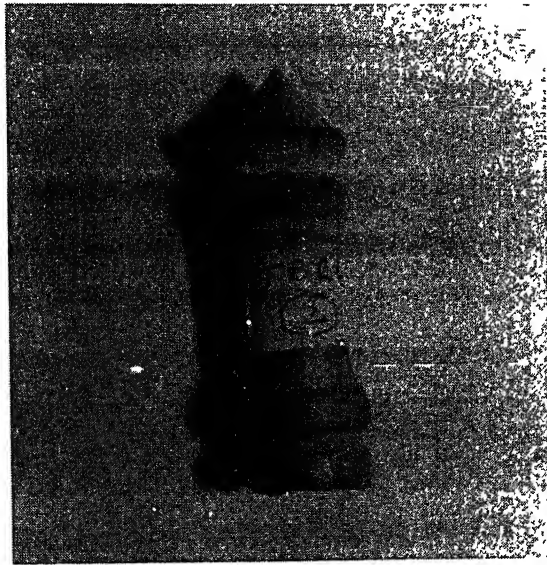
(a)
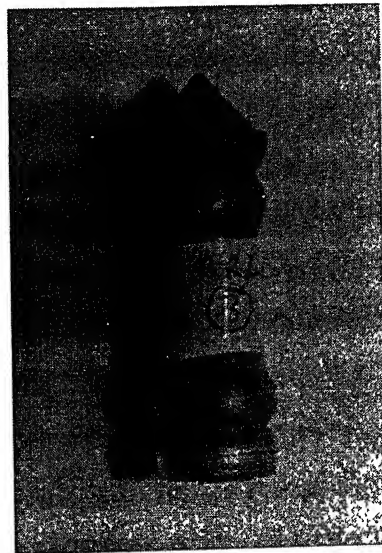


(b)

**Figure 5.6: (a) TBRL2 Ampule after explosive compaction (b) TBRL3 ampule after explosive compaction**

## 5.4 ELECTRON MICROSCOPY

### 5.4.1 Transmission Electron Microscopy

For analysis of mechanically alloyed 80Ni-15Fe-5Co powders, the powder was dispersed in acetone and allowed to settle down for 1 minute. After the bigger particles of the powder settled down, one drop of solution was taken from the upper portion of the solution by micropipette and placed on the carbon coated Cu grid (3mm dia., one side coated with carbon). The Cu grid was then allowed to dry under the electric bulb for 30 minutes and then observed under the transmission electron microscope.

Compacted samples were also analyzed by Transmission Electron Microscope. For this purpose, suitable sized circular pieces of explosive compacted 80Ni-1Fe-5Co were cut from the compacted cylindrical samples by diamond cutter. The samples so obtained, having thickness of approx. 1mm, were mechanically polished on emery papers (No 1/0-3/0) to reduce their thickness up to 0.1mm. Since the material was brittle, it was carefully cut into pieces and its sharp corners were polished to make them nearly circular. The final size of the each sample was 3 mm in diameter. Finally each sample was further thinned down by electro-jet polishing technique before examining it under Transmission Electron Microscope [Goodhew et al. 1988].

During the electro-jet polishing, the samples were further thinned down to the extent of electron transparency using twin jet electro-polishing unit at 20 volts and 30 mA. A solution containing 10% (by volume) perchloric acid and 90% acetic acid was used as an electrolyte. The bath temperature was maintained at 250C. All TEM work was carried out in a JOEL JEM-2000FX microscope at 160 kV.

## 5.4.2 Scanning Electron Microscopy

Powder morphology of raw Ni, Fe, Co and MA 80Ni-15Fe-5Co powders were analyzed under a JOEL JSM 840A Scanning Electron Microscope (SEM). The metal powder morphologies were observed by dispersing the powders with acetone on finely polished brass stubs prepared especially for this purpose. Sample preparation for the micro-structural studies consisted of standard emery paper polishing followed by fine cloth polishing with $0.3\mu m$ alumina abrasive particles in suspension with water.

## 5.5 X-RAY DIFFRACTION

Powder samples were taken out of planetary ball mill after different time intervals, and were characterized using X-ray diffraction technique. The bulk compacted samples were also characterized by this method. The instrument used was Seifert ISO-DEBYFLEX 2002 diffractometer with copper target. The tube was operated at 30kV and 10 mA. The radiation used was Cu K$\alpha$ having wavelength of 1.540598 A$^0$. The scanning rate in the X-ray powder diffraction was kept at $3^0$/min and $0.3^0$/min.

## 5.6 GRAIN SIZE DETERMINATION OF M.A. POWDERS

The grain sizes of the powder samples were determined by using "PEAKOC" software. The details about this software are as follows:

## 5.6.1 PEAKOC

"PEAKOC" is a general profile fitting computer program written in C++ programming language. It is particularly suitable for the INEL CPS detector data as it runs with the INEL data format and performs CPS calibration (files). But it can treat any other raw data in ASCII format too (from a Bragg Brentano setting for instance). Peakoc allows fitting peak-by-peak diffractogram under windows. Six peak shapes are proposed in this software: Gaussian, Lorentzian, Pearson VII, Voigt, Pseudo Voigt (PV) and Split Pseudo

Voigt (SPV). "Peakoc" is able to perform background removing, smoothening or $K\alpha_2$ stripping.

## 5.6.2 Procedure for Analysis

The data collected from the diffractometer was converted into the required format for the software. The X-ray diffraction patterns were fitted with a Gaussian function convoluted with an asymmetric function using the "PEAKOC" software for diffraction. The whole pattern was fitted in multiple steps along with a parabolic varying background. A nonlinear least square-fitting algorithm was used to minimize the residuals. Usual correction for the q-dependent part of the diffraction pattern was applied. The effect of diffraction of $K\alpha2$ line is removed with the correction for the instrumental broadening. Both the profile shape parameters (viz. peak position *2q*, maximum intensity *I*, half width *w* and the pV mixing parameter *h*) along with the background were refined simultaneously.

The grain size was calculated using Pseudo-Voigt function. The PEAKOC software gives the values of $2\theta$ and FWHM (full width at half maximum). To remove instrumental broadening effects from the FWHM value obtained for our sample, we followed following procedure. We eliminated the FWHM value (of the peak at same position as in our sample under investigation) of standard Si sample from the FWHM value of sample under investigation by the following approximation:

$$B = (W^2 - W_s^2)^{1/2} \tag{10}$$

where, B is the full width at half maximum after suitable correction, W is the FWHM of the sample under consideration and Ws is the FWHM of the standard, Silicon in the present case.

The value of B thus obtained is put in the Scherrer's formula to calculate the value of crystallite size.

The Scherrer's formula is:

$$D = (K\lambda)/ (B*Cos\theta). \qquad\qquad (11)$$

where, K is Scherrer's constant, $\lambda$ is wavelength of Copper K$\alpha$ radiation, $\theta$ is half of the value of 2$\theta$ in radians.

## 5.7 LASER PARTICLE SIZE ANALYSIS

FRITSCH PARTICLE SIZER ANALYSETTE 22 was used to determine the particle sizes of pure electrolytic iron, pure carbonyl nickel, pure cobalt and 125 hours ball milled 80Ni-1Fe-5Co powders. Measurement duration was of 20 scan in each of the above case.

## 5.8 DENSITY MEASUREMENT

Density evaluations of compacted samples of 80Ni-15Fe-5Co were done by dimensional measurements method and Archimedes method. During the density determination of compacted samples by Archimedes principle, the sample surface was coated by wax properly to avoid the seepage of water inside the compacted samples through pores, if any, present on the surface of the samples. Seepage of water inside the sample will give the erroneous results and the density calculated will be much higher than the actual density of the sample. Distilled water was used as a liquid media in these experiments.

## 5.9 MAGNETIC CHARACTERIZATION

Magnetic saturation curve and Curie temperature were determined by Vibrating Sample Magnetometer (VSM), Model 155 (Figure 5.7 and 5.8) [Manual for VSM]. A cylindrical sample of 3 mm diameter and 3mm length was cut from the compacted sample of 80Ni-15Fe-5Co. the sample w as fixed in a holder, which is kept at the center of the region between the pole pieces of the magnet. A slender vertical sample rod connects the sample holder with a transducer assembly located above the magnet, which in turn, supports the transducer assembly by means of sturdy, adjustable support rods.

The transducer converts a sinusoidal as drive signal, provided by an oscillator/amplifier circuit located in the console, into a sinusoidal vertical vibration of the sample rod, and the sample is thus made to undergo a sinusoidal motion in a uniform magnetic field. Coils mounted on the pole pieces of the magnet pick up the signal resulting from the sample motion. This ac signal at the vibration frequency is proportional to the magnitude of the moment induced in the sample. However, it is also proportional to the vibration amplitude and frequency. This being the case, moment readings are taken by measuring the amplitude of the signal.
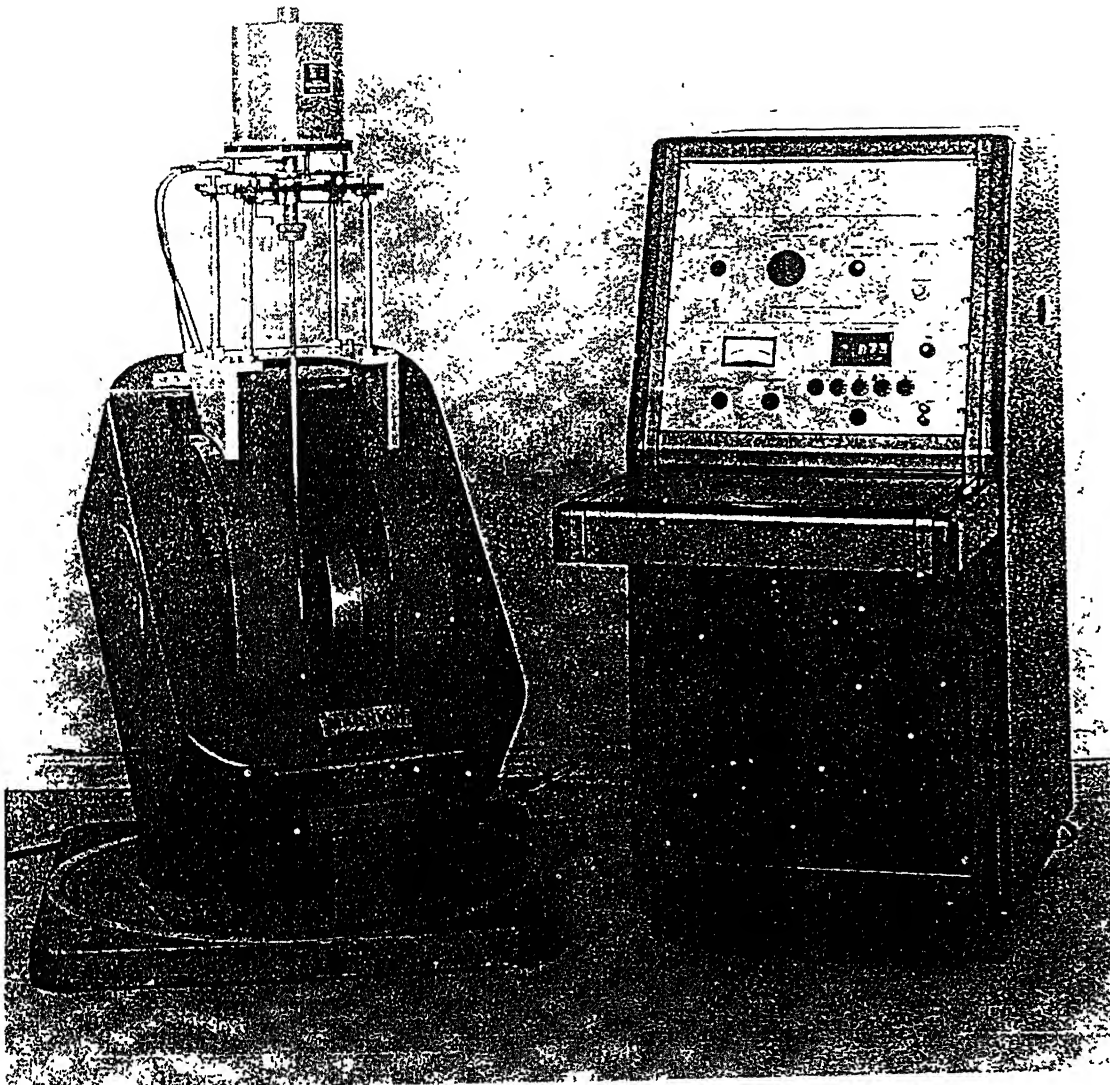
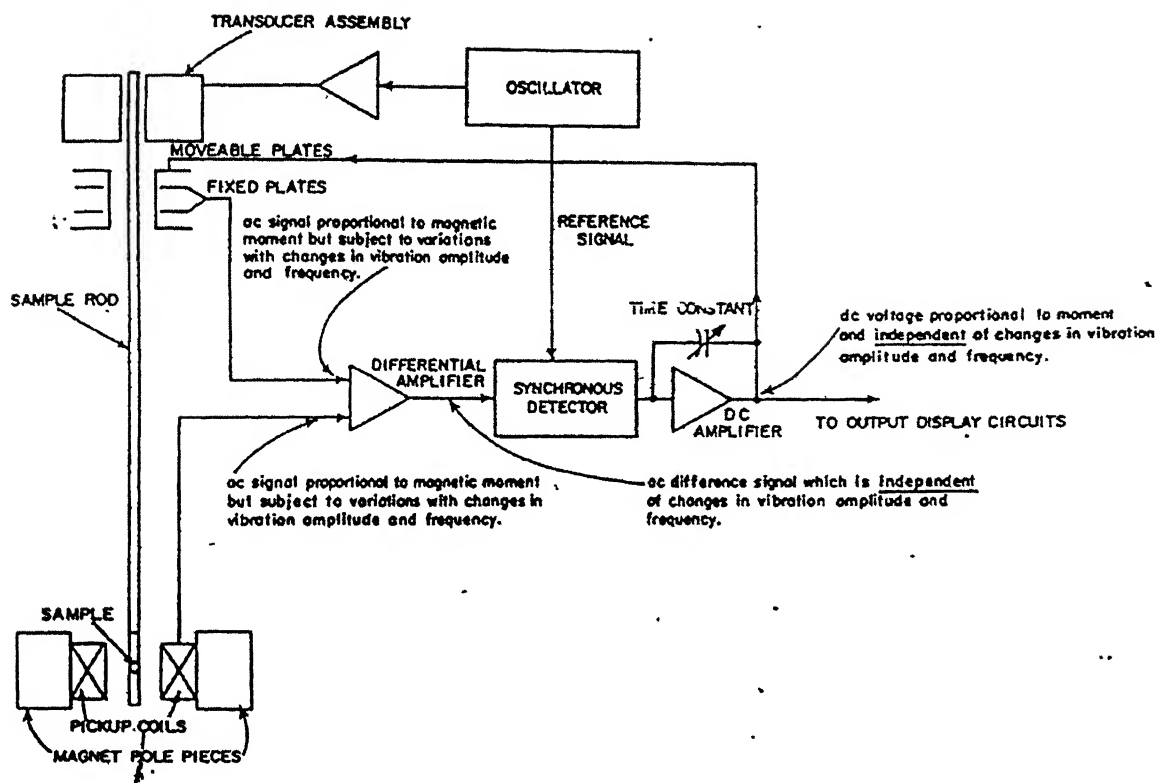Figure 5.7 Model 155 Magnetometer System Assembly

TRANSDUCER ASSEMBLY

OSCILLATOR

MOVEABLE PLATES

FIXED PLATES

ac signal proportional to magnetic
moment but subject to variations
with changes in vibration amplitude
and frequency.

REFERENCE
SIGNAL

SAMPLE ROD

TIME CONSTANT

dc voltage proportional to moment
and independent of changes in vibration
amplitude and frequency.

DIFFERENTIAL
AMPLIFIER

SYNCHRONOUS
DETECTOR

DC
AMPLIFIER

TO OUTPUT DISPLAY CIRCUITS

ac signal proportional to magnetic moment
but subject to variations with changes in
vibration amplitude and frequency.

ac difference signal which is independent
of changes in vibration amplitude and
frequency.

SAMPLE

PICKUP COILS

MAGNET POLE PIECES

Figure 5.8 Simplified block diagram of the model 155 Magnetometer

# CHAPTER 6

## 6. RESULTS AND DISCUSSION

### 6.1 XRD STUDIES ON MA 80Ni–15Fe–5Co POWDER

#### 6.1.1 Phase Identification in MA 80Ni–15Fe–5Co Powder

The XRD patterns of MA 80Ni–15Fe–5Co, milled for 15min., 12hr, 50hr, 125hr and 170hr are shown in Figure 6.1 to 6.5 respectively. These XRD patterns show predominantly three peaks. The intensity & d values of these peaks are shown in Table 6.1. These are in order of decreasing intensity in all diffraction patterns. On comparing intensities and d values with all the standard compounds of Ni, Fe, Co and oxygen i.e. $NiO$, $Ni_2O_3$, $CoO$, $Co_2O_3$, $Co_3O_4$, $FeO$, $Fe_2O_3$ and $Fe_3O_4$ which are shown in Appendix 1, it was concluded that no oxide peak was present in the XRD patterns of the milled powder, indicating absence of any substantial quantity of oxides.

The XRD pattern of 125hr milled 80Ni–15Fe–5Co (Figure 6.4) was selected for phase identification. This XRD pattern shows three prominent peaks at 2θ values of $44.40^0$, $51.65^0$ and $76.30^0$ respectively, in order of decreasing intensities. The 2θ values, Intensities, d values and corresponding planes of 125hr milled 80Ni–15Fe–5Co, FeNi, $FeNi_3$, FeCo and $Co_3Fe_7$ are shown in Table 6.2. The 2θ values, d values & Intensities of the peaks of MA 80Ni – 15Fe – 5Co were compared with those of Fe, Ni, Co, FeNi, $FeNi_3$, FeCo and $Co_3Fe_7$ for phase identification.

The XRD pattern of the present MA Ni–Fe–Co have not been compared with ternary phase of Ni–Fe–Co alloy due to unavailability of XRD data of ternary alloys of Ni – Fe – Co. On comparing the 2θ values, d values and intensities of MA 80Ni–15Fe–5Co (125h milled) with those of Ni, Fe, Co, FeNi, $FeNi_3$, FeCo and $Co_3Fe_7$ it was concluded that the

first peak of the XRD pattern of the MA Ni-Fe–Co belongs to (111) $FeNi_3$, (111) FeNi, (110) FeCo and (110) $Co_3Fe_7$, whereas second peak belongs to (200) $FeNi_3$ and (200) FeNi.
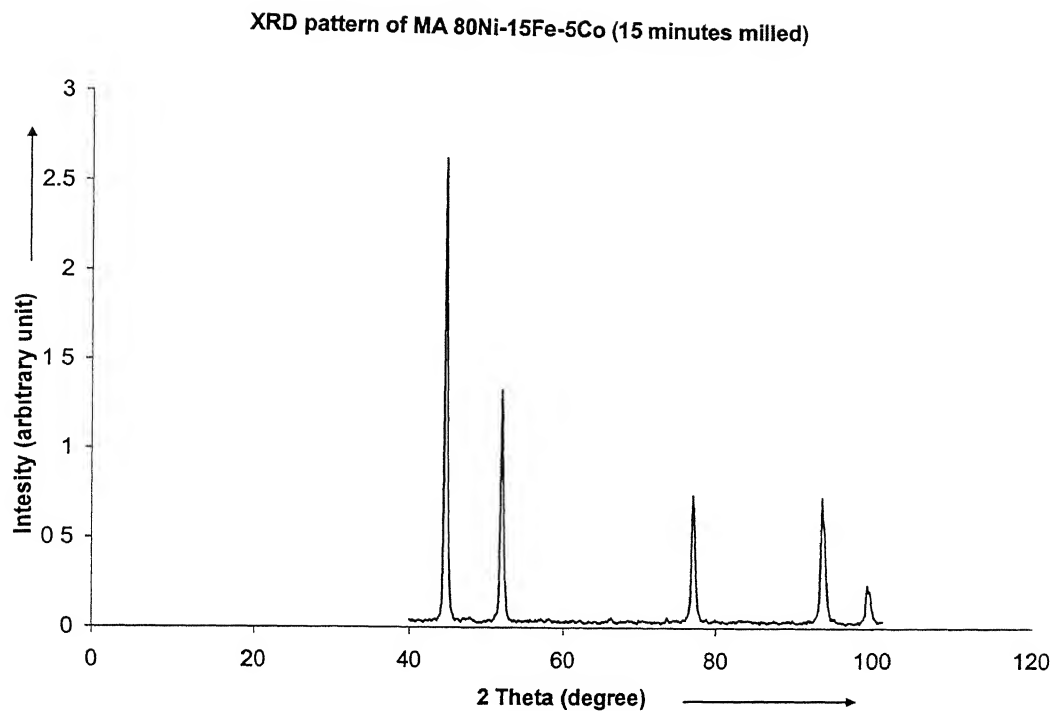
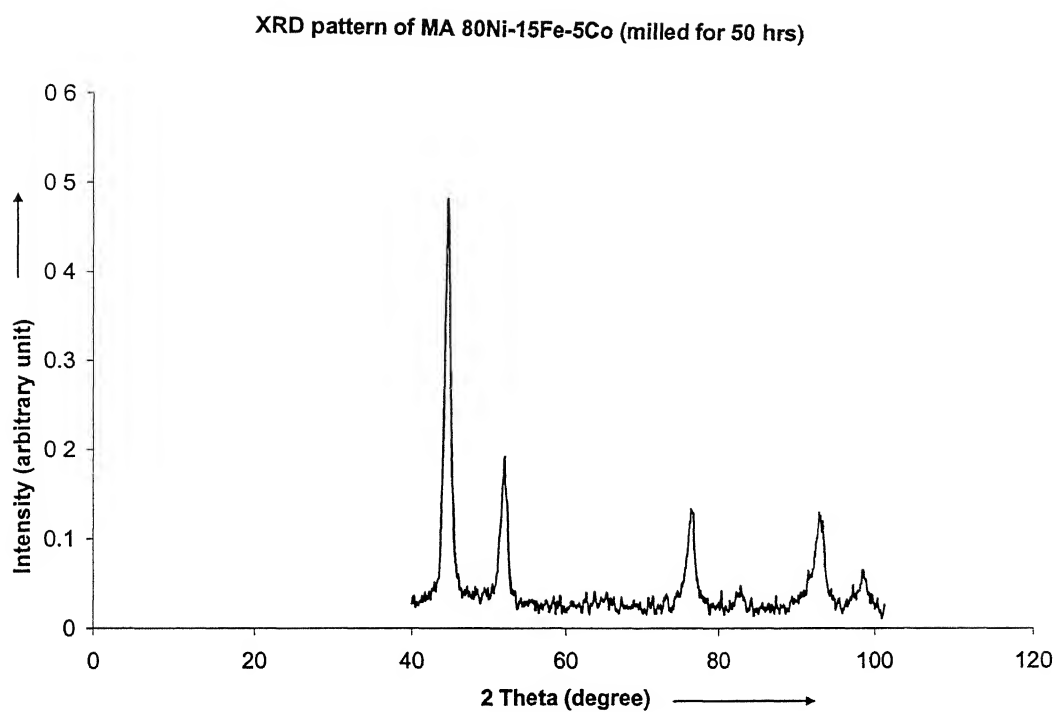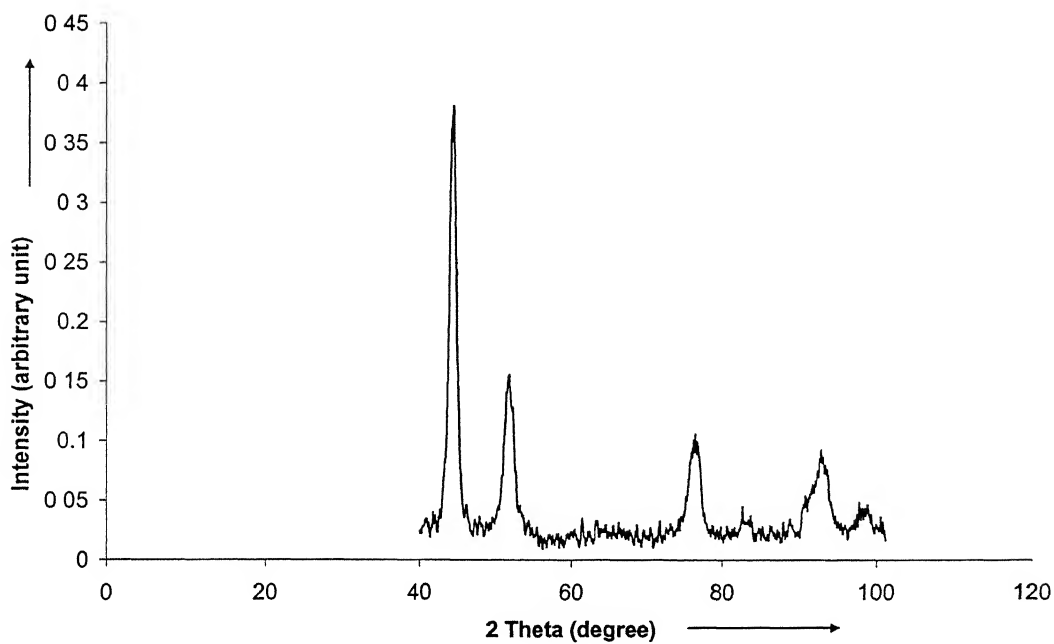**XRD pattern of MA 80Ni-15Fe-5Co (15 minutes milled)**



**Figure 6.1 XRD pattern of MA 80Ni-15Fe-5Co powder milled for 15 min.**

**XRD Pattern of MA 80Ni-15Fe-5Co (milled for 12 hrs)**
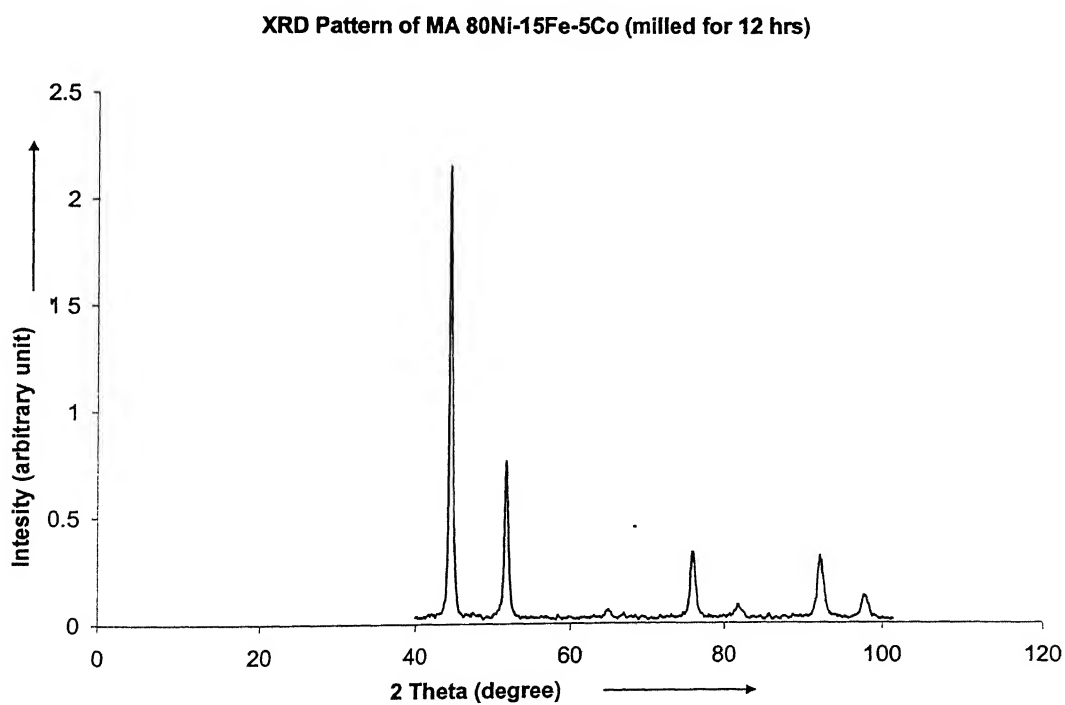


**Figure 6.2 XRD pattern of MA 80Ni-15Fe-5Co powder milled for 12 hr.**

**Figure 6.3 XRD pattern of MA 80Ni-15Fe-5Co powder milled for 50 hr.**

**Figure 6.4 XRD pattern of MA 80Ni-15Fe-5Co powder milled for 125 hr.**
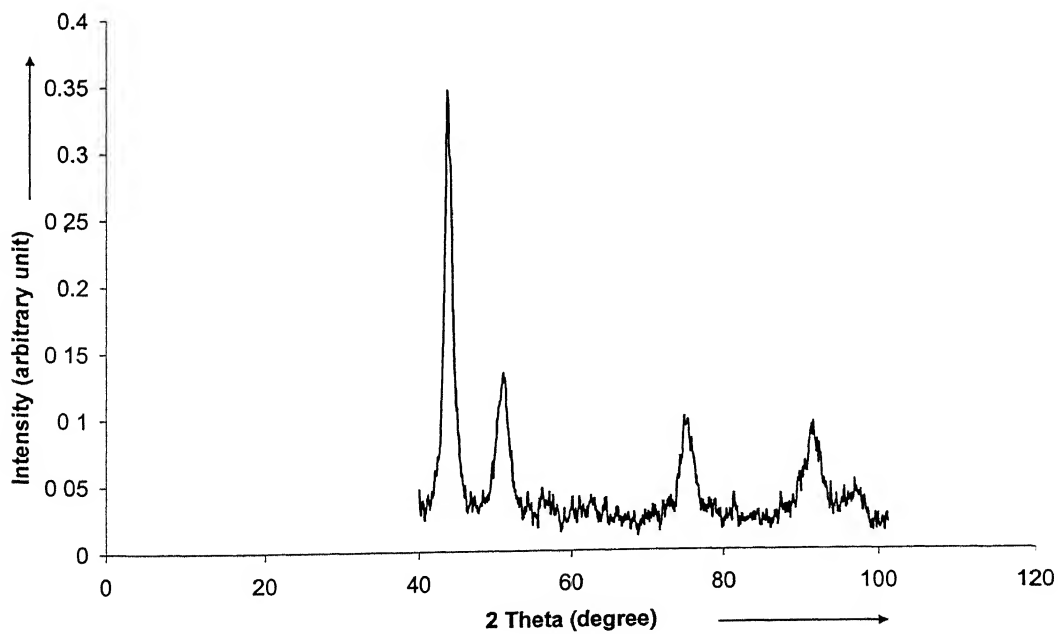


**Figure 6.5 XRD pattern of MA 80Ni-15Fe-5Co powder milled for 170 hr.**

95

**Table 6.1 Intensities and d-values of different peaks of MA 80Ni-15Fe-5Co powder milled for various period of time.**

| S. No. | Alloys/System | Peak Intensities (%) | d ($A^0$) |
|--------|---------------|----------------------|-----------|
| 1. | 80Ni-15Fe-5Co (15 minutes milled) | 98<br>49<br>28<br>27 | 2.034<br>1.764<br>1.249<br>1.066 |
| 2. | 80Ni-15Fe-5Co (12 hours milled) | 100<br>36<br>16<br>15 | 2.038<br>1.765<br>1.249<br>1.065 |
| 3. | 80Ni-15Fe-5Co (50 hours milled) | 100<br>40<br>27<br>25 | 2.036<br>1.764<br>1.247<br>1.066 |
| 4. | 80Ni-15Fe-5Co (125 hours milled) | 100<br>41<br>25<br>24 | 2.040<br>1.770<br>1.248<br>1.068 |
| 5. | 80Ni-15Fe-5Co (170 hours milled) | 99<br>38<br>28<br>28 | 2.066<br>1.790<br>1.272<br>1.080 |

**Table 6.2 Intensities, 2θ values, d-values and corresponding planes of 125 hours milled 80Ni-15Fe-5Co, FeNi, FeNi$_3$, FeCo and Fe$_7$Co$_3$**

| S. No. | Alloy-System/ Compound | Intensity (%) | Angle (2θ) | d-values (A$^0$) | (hkl) |
|--------|------------------------|---------------|------------|------------------|-------|
| 1. | 80Ni-15Fe-5Co (125 hours-milled) | 100 41 25 24 | 44.41 51.65 76.27 92.43 | 2.04 1.77 1.25 1.07 | ---- ---- ---- ---- |
| 2. | FeNi | 100 100 100 | 43.51 50.72 74.75 | 2.08 1.8 1.27 | (111) (200) (220) |
| 3. | FeNi$_3$ | 100 60 40 30 | 44.32 51.58 92.30 75.94 | 2.04 1.77 1.07 1.25 | (111) (200) (311) (220) |
| 4. | CoFe | 100 25 14 | 44.87 82.74 65.32 | 2.02 1.17 1.43 | (110) (211) (200) |
| 5. | Co$_3$Fe$_7$ | 100 36 25 | 44.76 82.50 65.16 | 2.025 1.17 1.43 | (110) (211) (200) |

Further the identification of third peak shows that this peak belongs to (220) FeNi and (220) FeNi$_3$. From the above analysis it can be concluded that 125 hr milled MA 80Ni-15Fe-5CO is solid solution of Fe and Co in Ni. In this system, FeNi$_3$ (an intermetallic compound having face centered cubic crystal structure) is the predominant phase present whereas FeNi, FeCo and Co$_3$Fe$_7$ phases are also present in the system. The data from JCPDS files show that crystal structure of all the phases present in this system is cubic in nature. Hence it can be predicted that crystal structure of the system will also be cubic.

Figure 6.6 compares the XRD pattern of pure Ni with that of 125 hr milled MA 80Ni-15Fe-5Co powder. It can be seen that there is no extra peak in the XRD pattern of MA 80Ni-15Fe-5Co powder as compared to that of pure Ni. Further it can also be seen that there is slight shifting of all the peaks of MA 80Ni-15Fe-5Co powder towards lower angles as compared to the peaks of pure Ni. This slight shifting indicates that alloying is taking place in pure Ni. Intensities of the peaks at higher angles in MA 80Ni-15Fe-5Co powder are very small or rather peaks seem to disappear. This dis-appearance of peaks at higher angles indicates the partial amorphization. From the above it can be concluded that since Ni has an FCC structure, the crystal structure of the phases present in MA 80Ni-15Fe-5Co powder is also FCC

## 6.1.2 Determination of Crystallite size of MA 80Ni–15Fe–5Co Powder

Crystallite size of the MA powder, milled for 15min., 12hr, 50hr, 125hr and 170hr, was determined from the respective XRD patterns, as shown in Figures 6.1 to 6.5, using X-ray broadening technique while taking two major peaks (111) and (220) into consideration. The profile shape function of the type Pseudo-Voigt was filled on the smoothened X-ray data of Figures 6.1 to 6.5.

In order to get the real FWHM of the samples, the instrumental broadening was removed. For this purpose, XRD patterns of standard sample of pure silicon was obtained using the same experimental parameters as used in the sample of MA Ni–Fe–Co powder.

Comparison of XRD Patterns of Pure Ni and 125 hr milled MA 80Ni-15Fe-5Co Powder
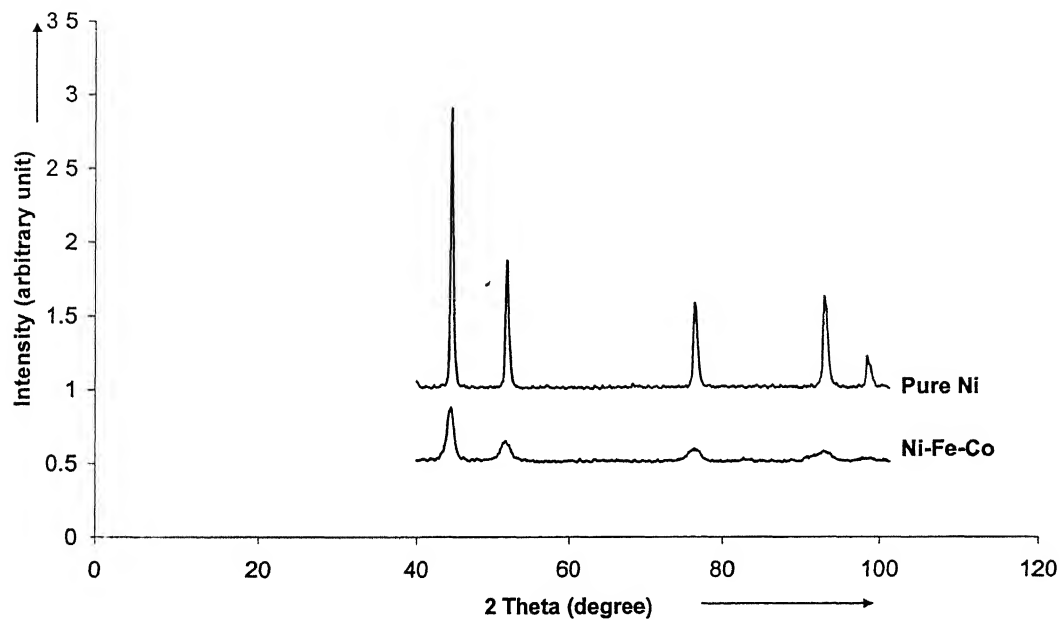
**Figure 6.6 Comparison of XRD patterns of Pure Ni and 125 hr milled MA 80Ni-15Fe-5Co powder**

From this data of silicon instrumental broadening effect in the XRD patterns of the MA 80Ni-15Fe-5Co powder was removed. The FWHM obtained after removal of instrumental broadening effect, was used to determine crystallite size using Scherrer's formula. The values of fit of $2\theta$ and FWHM for MA 80Ni–15Fe–5Co powder milled for various period of time were calculated and are shown in Table 6.3. The crystallite size of the MA Ni–Fe–Co powders, milled for different periods of time, was calculated for the plane (111) and (200) using equation (11), and these are also shown in Table 6.3.

The effect of milling time on the crystallite size corresponding to (111) plane of the resulting Ni–Fe–Co powder is schematically shown in Figure 6.7. Figure 6.7 clearly shows that the rate of decrease in the crystallite size is very rapid in the first 12 hours of milling. Subsequently the rate of decrease in grain size is less rapid up to 125 hr of milling. Beyond this much milling time, the grain size of the MA powder is almost constant. This behavior of crystallite size refinement vs milling time is same as reported by Eckert et al. (1992). The reason for this trend is that in the initial phase of milling powder particles are deformed and fractured severely which causes accumulation of defects, dislocations, stacking faults etc. and these features cause severe distortions in the lattice. These defects become localized in the shear bands formed and then disintegrate into smaller grains due to higher instability of the structure.

Figure 6.8 compares the XRD pattern of MA 80Ni–15Fe–5Co powder milled for various periods of time. It can be seen that the broadening in peaks is increasing as the milling time is increased. Data of FWHM shown in Table 6.3 also confirms this observation. It can also be observed that apart from broadening in peaks, the intensities of higher peaks have reduced and the peaks at high angles have almost disappeared. This indicates that partial amorphization has occurred in the powder. The crystallite size vs milling time behavior, obtained for two different peaks, corresponding to two different planes i.e. (111) & (200) for MA powder are shown in Figure 6.9.

**Table 6.3 Angle (2θ) and FWHM values obtained from the Pseudo-Voigt curve fitting on experimental XRD data of MA 80Ni-15Fe-5Co powder milled for various periods of time and the calculated grain size.**

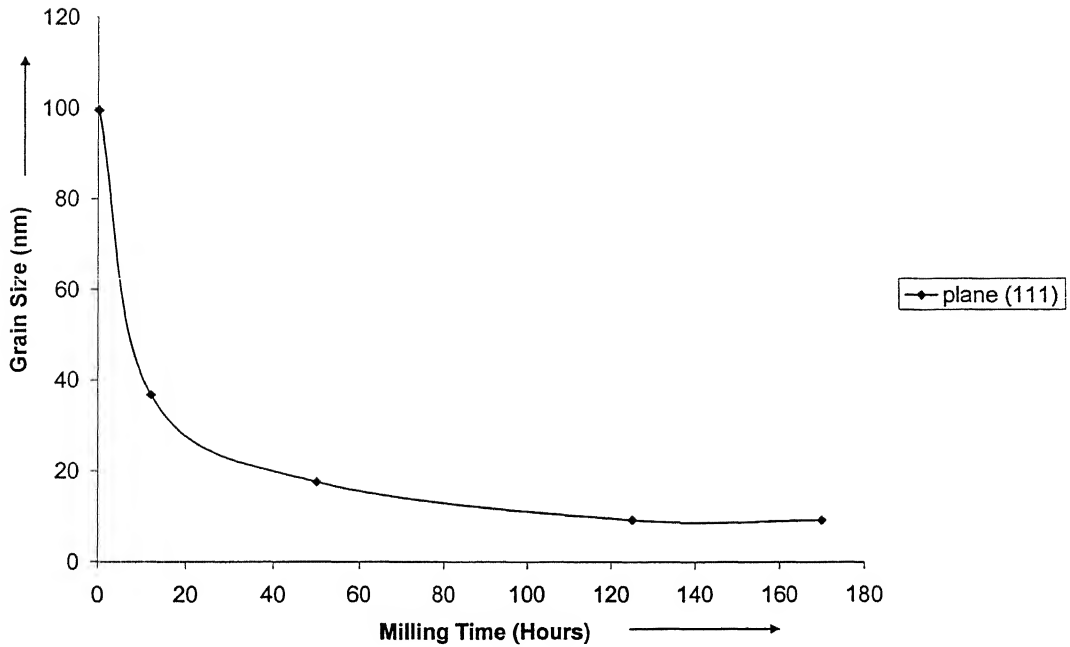| Milling Time (hours) | 2θ values (degree) | | FWHM (degree) | | Grain Size (nm) | |
|---|---|---|---|---|---|---|
| | (111) | (200) | (111) | (200) | (111) | (200) |
| 0.25 | 44.64 | 52.09 | 0.4384 | 0.4510 | 100 | 35 |
| 12 | 44.53 | 51.78 | 0.4900 | 0.5710 | 37 | 21 |
| 50 | 44.56 | 51.88 | 0.6134 | 1.2650 | 18 | 7 |
| 125 | 44.39 | 51.72 | 1.0562 | 1.7142 | 9 | 5 |
| 170 | 44.39 | 51.73 | 1.0156 | 1.7130 | 9 | 5 |

**Figure 6.7 Effect of milling time on the crystallite size corresponding to (111) plane of 80Ni-15Fe-5Co powder.**
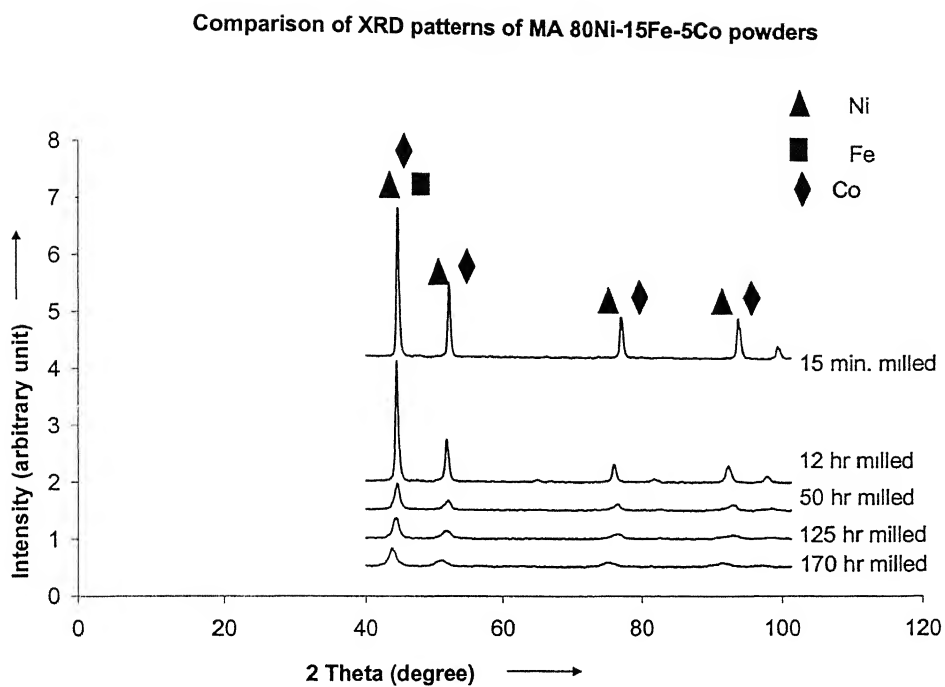
Figure 6.8 Comparison of XRD patterns of MA 80NI-15Fe-5Co powders milled for different periods of time.

**Effect of milling time on the crystallite size of 80Ni-15Fe-5Co System**
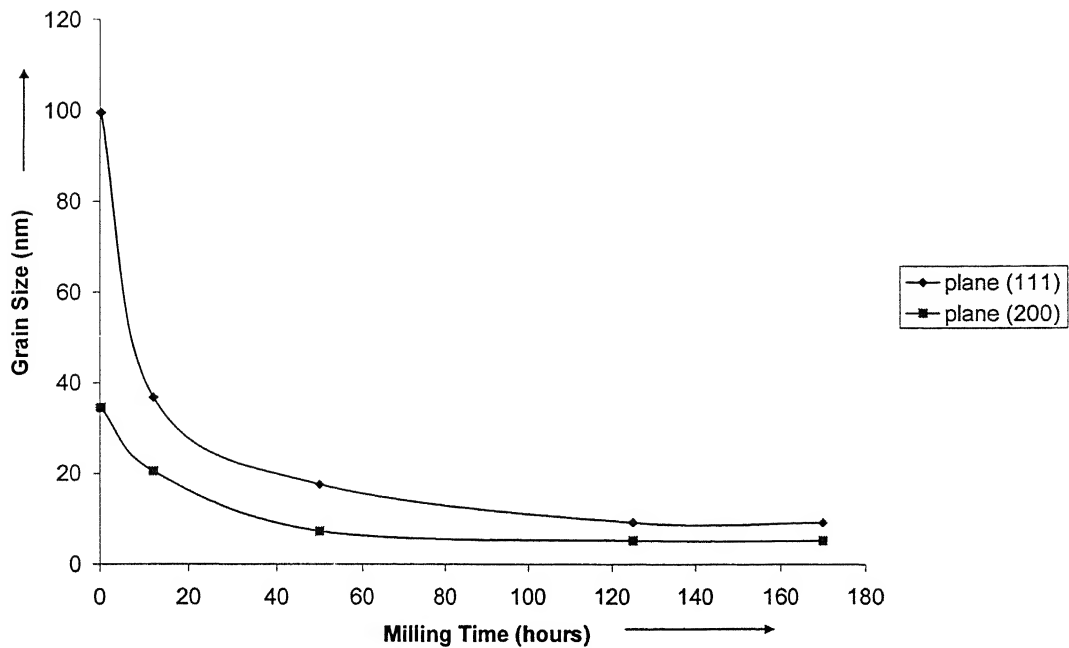
**Figure 6.9 Comparison of effect of milling time on the crystallite size corresponding to plane (111) and (200) of 80Ni-15Fe-5Co powder system.**

It can be seen from the figure 6.9 that the trend of behavior is very similar for the two planes. It can also be observed from Table 6.3 that crystallite size obtained from peaks corresponding to (111) plane is greater than that obtained from (200) planes. This is because of the fact that the d-spacing for (111) plane is greater that (200) plane.
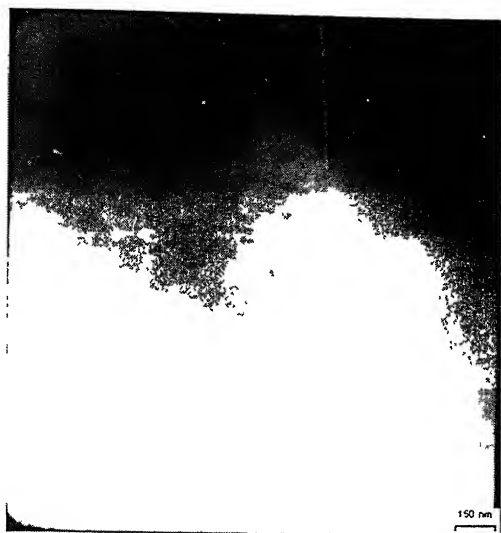
## 6.2 TEM ANALYSIS OF 125 hr MILLED MA 80Ni-15Fe-5Co POWDER

A bright field TEM micrograph of one of the particle of 125 hr milled MA 80Ni-15Fe-5Co powder is shown in Figure 6.10a. This Figure shows the crystalline nature of the particle. The corresponding SADP of the area, which is shown in Figure 6.10b, also confirms the crystalline nature of the particle. The ring pattern indicates that the system has very fine grain structure. Grain sizes from the above TEM image were calculated in the range of 10 − 50 nm. The ring pattern indicates that the crystallites have random orientations in the system.
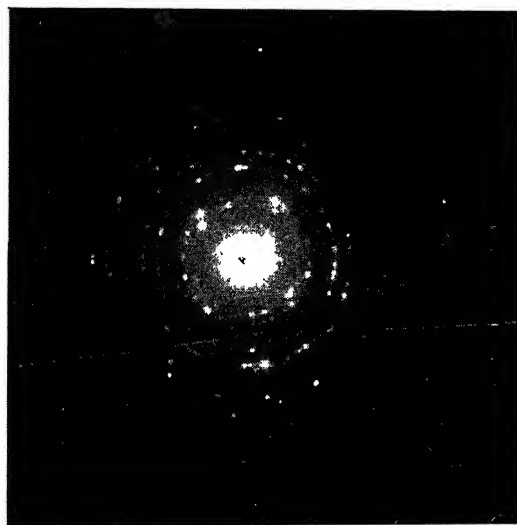
A bright field TEM micrograph of another particle is shown in Figure 6.11a. It gives clear evidence that the particle under consideration has got amorphised. The amorphous character can be inferred from the featureless nature of the particle in most of the area except for a few dark spots which could be fine nano-sized crystallites. The corresponding SADP (Small Area Diffraction Pattern) of the same particle is shown in Figure 6.11b, which shows amorphous ring pattern. It supports the earlier conclusion that the some particles have got amorphised.

A bright field TEM micrograph of another particle of the powder, shown in Figure 6.12a, shows a featureless amorphous region and darker regions which are crystallized regions with the crystallite size in the nano scale range. A localized region showing "Dynamic Crystallization" is also marked in this region. The corresponding SADP, shown in Figure 6.12b confirms the amorphous nature while showing diffused ring pattern. Figure 6.13 shows the higher magnification image of the dynamically recrystallized region. The banded nature of the rod like particle in the region could be due to twinning.

Hence from the above analysis it can be concluded that 125 hr milled MA 80Ni-15Fe-5Co powder contains predominantly nanocrystalline structure though it contains some areas which are amorphous in nature. The structure also contains defects like stacking faults etc. which are obvious due to the severe milling of the powder.
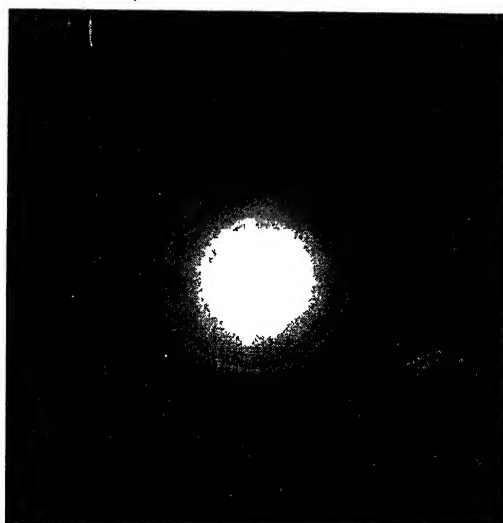
(a)



(b)

Figure 6.10: (a) Bright field TEM micrograph of 125 hr milled MA 80Ni-15Fe-5Co powder and (b) corresponding Selected Area Diffraction Pattern (SADP)
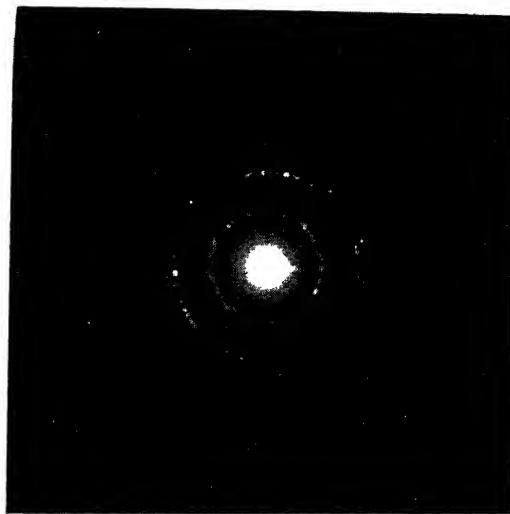
(a)



(b)

Figure 6.11: (a) Bright field TEM micrograph of 125 hr milled MA 80Ni-15Fe-5Co powder and (b) corresponding Selected Area Diffraction Pattern (SADP)

(a)



(b)

Figure 6.12: (a) Bright field TEM micrograph of 125 hr milled MA 80Ni-15Fe-5Co powder and (b) corresponding Selected Area Diffraction Pattern (SADP)
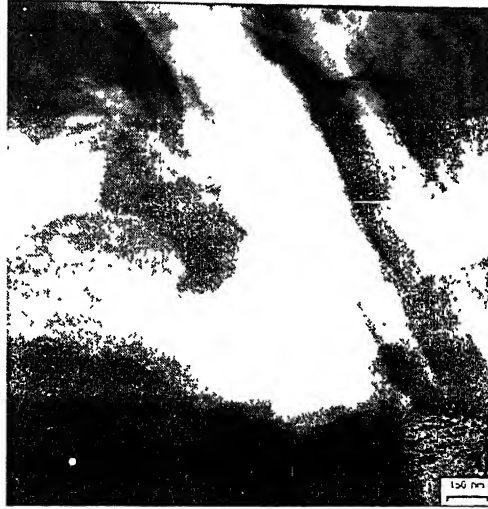
Figure 6.13: Bright field TEM micrograph of 125 hr milled MA 80Ni-15Fe-5Co powder showing magnified image of dynamic recrystallized region

## 6.3 GRAIN GROWTH KINETICS OF 125 hr MILLED NANOCRYSTALLINE MA 80Ni-15Fe-5Co POWDER ON ISOTHERMAL ANNEALING

The 125 hr milled MA nanocrystalline 80Ni-15Fe-5Co powder was annealed at $500^0$C for different periods of time. Table 6.4 shows the isothermal grain growth results of 125 hr milled M A n anocrystalline 8 0Ni-15Fe-5Co p owder a nnealed a t 5 00$^0$C for 1 5 m in., 3 0 min., 45 min. and 60 min. along with the grain size of starting powder. Figure 6.14 shows the grain growth behavior of the 80Ni-15Fe-5Co powder with different annealing times. Analyzing the Figure 6.14, we observe that the grain growth kinetics exhibits the following general features:

1) The grain size first increases rapidly and then increases very slowly.
2) The grain growth is very f ast in the first 10 minutes, which implies that a low activation energy process is dominating in this growth stage.
3) Beyond 10 minutes sintering time, the grain growth exhibits a level off trend suggesting that a higher activation energy process is operating in this stage.

The existence of a larger number of interfaces and their change during grain growth is thought to play an important part in grain growth process of nanocrystalline materials. The low activation energy can be attributed to the large percentage of highly disordered interfaces in the as prepared nanocrystalline 80Ni-15Fe-5Co powder. As temperature or annealing time increases, structural relaxation of these interfaces takes place and reduces the degree of disorder as explained by Shek et al. (1999). The energy barrier of this structural change arising from the local rearrangement of atoms is much lower than the energy barrier for diffusional grain growth. The ordering of distorted interfaces by structural relaxation proceeds with grain growth. Low activation energy facilitates the short-range rearrangement of atoms in the interface region.

**Table 6.4 Grain size of 125 hr milled MA nanocrystalline 80Ni-15Fe-5Co powder at different annealing times.**

| S.No. | Annealing Time (minute) | Grain Size (nm) |
|-------|-------------------------|-----------------|
| 1.    | 5                       | 25              |
| 2.    | 10                      | 40              |
| 3.    | 15                      | 51              |
| 4.    | 30                      | 56              |
| 5.    | 60                      | 62              |

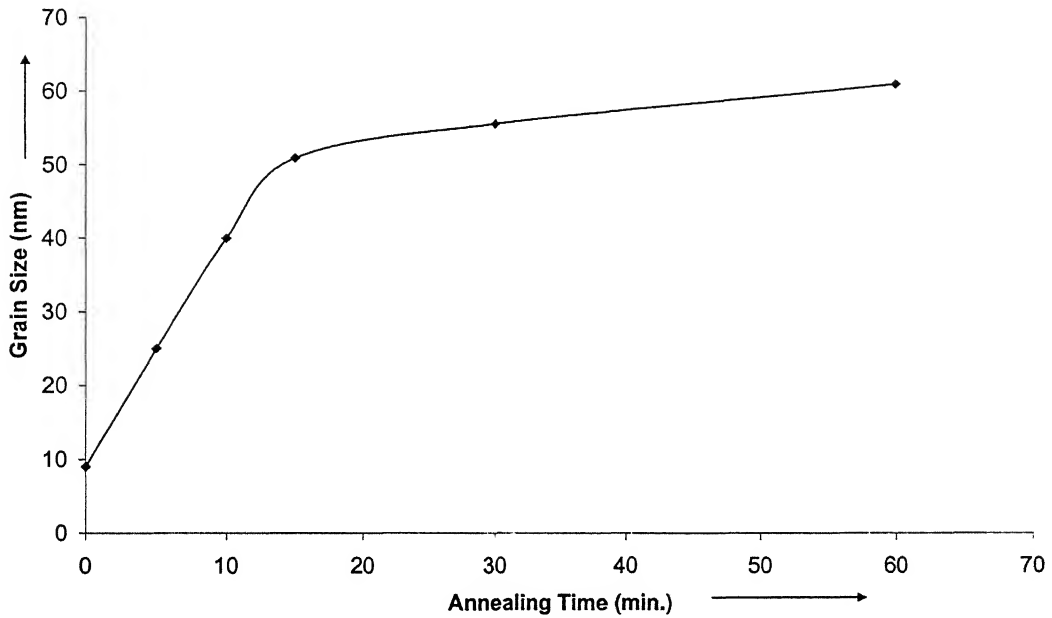Grain Growth Behaviour of nanocrystalline MA 80Ni-15Fe-5Co powder annealed at 500 degC

**Figure 6.14 Grain growth behavior of the 125 hr milled MA nanocrystalline 80Ni-15Fe-5Co powder with annealing time. The annealing temperature was kept at $500^0$C.**

## 6.4 EXPLOSIVE COMPACTION BEHAVIOR OF 125 hr MILLED MA NANOCRYSTALLINE 80Ni-15Fe-5Co POWDER

Nanocrystalline 80Ni-15Fe-5Co powder, prepared by mechanical alloying process, was compacted using explosive compaction technique under different conditions. Two compacted powder samples, designated as TBRL2 and TBRL3 respectively, were collected after the explosive compaction, and were machined to take out the compacted powder which was cylindrical in shape. The outer surfaces of the machined samples did not show any defect such as crack or depression.

### 6.4.1 Density of Explosive Compacted 125 hr Milled MA Nanocrystalline 80Ni-15Fe-5Co Powder.

For calculating % theoretical density of the explosive compacted specimen, theoretical density of the 80Ni-15Fe-5Co (wt %) system was calculated using the following formula:

$$D_T = (W_{Ni} + W_{Fe} + W_{Co}) / \{(W_{Ni}/D_{Ni}) + (W_{Fe}/D_{Fe}) + (W_{Co}/D_{Co})\} \qquad (12)$$

where, $W_{Ni}$ = Weight of Ni in the mixture

$\quad W_{Fe}$ = Weight of Fe in the mixture

$\quad W_{Co}$ = Weight of Co in the mixture

$\quad D_{Ni}$ = Theoretical density of Ni (8.9 g/cc)

$\quad D_{Fe}$ = Theoretical density of Fe (7.86 g/cc)

$\quad D_{Co}$ = Theoretical density of Co (8.9 g/cc)

Using the above method theoretical density of the 80Ni-15Fe-5Co (wt %) system was calculated and it came out to be 8.72 g/cc. This value of theoretical density is an approximate value as density due to the final phases formed could be different than the density obtained using density of the constituent elements.

Density of the explosive compacted samples i.e. TBRL2 and TBRL3, was measured using Archimedes method. Samples were coated with wax to prevent the seepage of water in the samples, as seepage of water in the samples gives higher density as compared to its true value. To verify the values of densities obtained above, density of the samples was also obtained by measuring the dimensions of the machined samples. Table 6.5 gives the % shrinkage in diameter after explosive compaction of MA powder. It can be seen that in both the cases, the % shrinkage in diameter is about 33-34 %. The above table also shows the density of explosive compacted specimens, measured by Archimedes method and by dimension measurement method. It can be seen that values obtained from both the methods are very similar. It can be noted that both the explosives used in the present study give about 90% of theoretical density.

**Table 6.5 Density of explosive compacted samples calculated using Archimedes method and dimensional measurements.**

| S. No . | Sample Designa- -tion | Diameter of powder mass before Compact- -ion (mm) | Diameter of powder mass after Compact- -ion (mm) | % Shrinkage in diameter | Density obtained by Archimedes Method | | Density obtained by Dimensional Measurements | |
|---|---|---|---|---|---|---|---|---|
| | | | | | g/cc | % of $D_T$ | g/cc | % of $D_T$ |
| 1. | TBRL2 | 12.8 | 8.5 | 34 | 7.76 | 8.9% | 7.85 | 90% |
| 2. | TBRL3 | 12.8 | 8.6 | 33 | 7.81 | 89.5 | 7.71 | 88% |

## 6.4.2 Densification and Deformation Behavior of the MA 80Ni-15Fe-5Co Powder during Explosive Compaction

In order to study the densification and deformation behavior of MA 80Ni-15Fe-5Co powder during explosive compaction, fractured samples of explosive compacted specimens, both at transverse cross-section and longitudinal cross section were studied under Scanning Electron Microscope. Figure 6.15 shows the structure of the explosive compacted specimen TBRL2 at the centre of the transverse cross section. It can be seen that a hole has formed at the centre of the specimen. The formation of hole at the centre may be due to the convergence of shock wave on the cylinder axis which forms a pressure spike and axial shock. The pressure spike and axial shock can impart a large axial speed to material. If the compression is large enough, material is blown out, leaving a hole along the axis.

Figures 6.16-6.22 show the SEM photographs of the explosive compacted TBRL2 samples at the transverse cross-section near the periphery of the specimen. It can be seen that a structure having wavy pattern emanating from the periphery towards the centre is obtained in the explosive compaction specimens (Figures 6.16 -6.18). This suggests that there is an extensive material flow in the direction of shock wave propagation. i.e. from the periphery to the centre. Some radial cracks in the explosive compacted specimens were also observed (Figure 6.16 and Figure 6.19). This may be due to the release of shock waves after the explosion.

The most interesting feature of the structure of the explosive compacted specimens, as revealed by the SEM photographs is that the original flaky powder particles of the MA 80Ni-15Fe-5Co powder has deformed into an elongated shape. Subsequently such elongated particles have joined together to form a bigger particle having some pores in between. It appears that the flaky particles of MA 80Ni-15Fe-5Co powder are getting folded during explosive compaction to form elongated particles. Such a behavior is evident from Figures 6.20-6.22, which show the process of folding in a powder particle. Several such particles not only get joined together but also that these
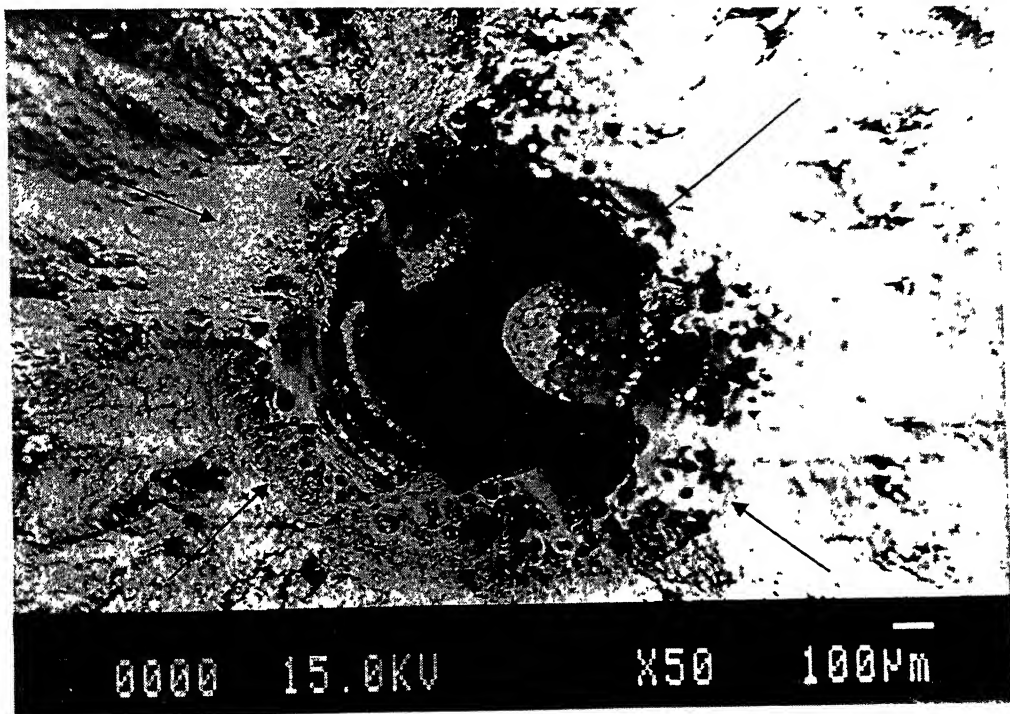
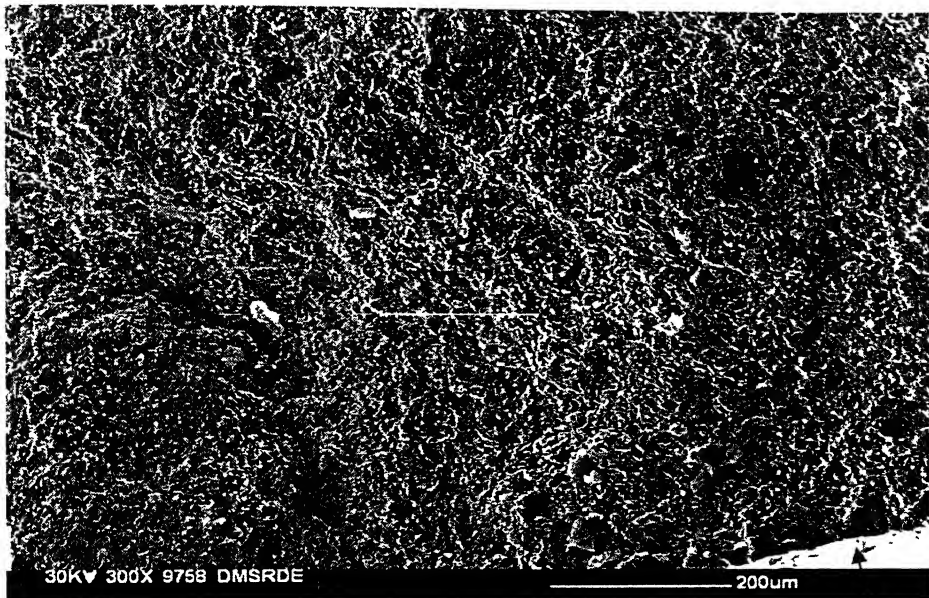**Figure 6.15 SEM photograph of fracture surface at the centre of the specimen TBRL2**

**Figure 6.16** Fracture surface at the periphery of the specimen TBRL2 (arrow is indicating the periphery as well as the direction of initial shock propagation)
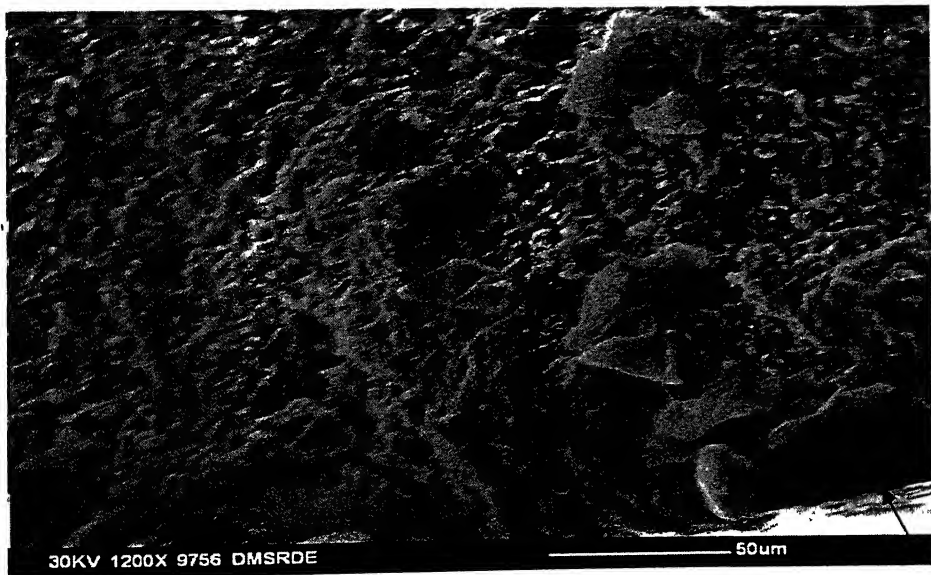


**Figure 6.17** Fracture surface at the periphery of the specimen TBRL2 (arrow is indicating the periphery as well as the direction of initial shock propagation)

**Figure 6.18** Fracture surface at the periphery of the specimen TBRL2 (arrow is indicating the periphery as well as the direction of initial shock propagation)
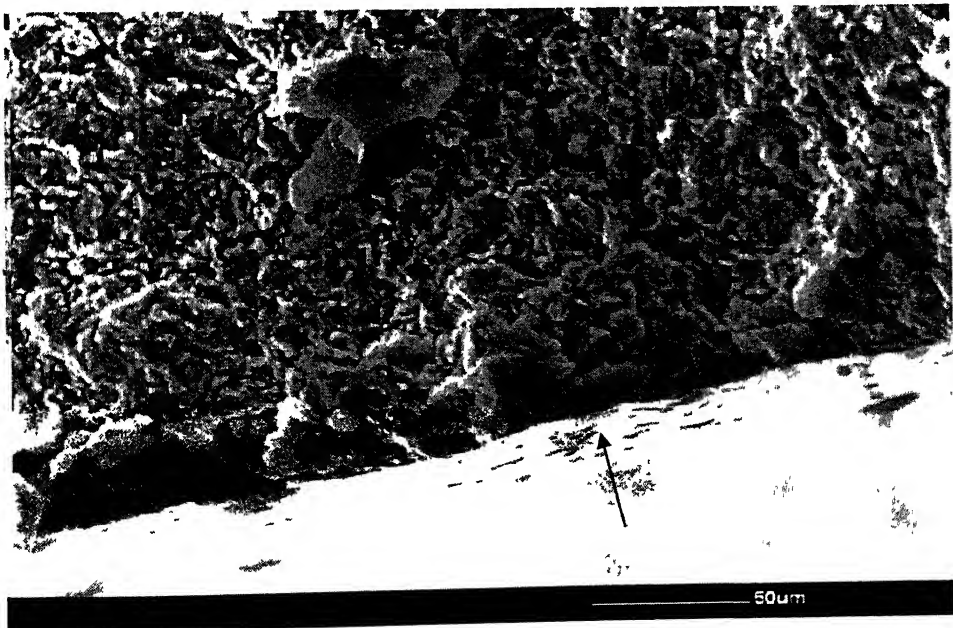


**Figure 6.19** Fracture surface at the periphery of the specimen TBRL2 (arrow is indicating the periphery as well as the direction of initial shock propagation)
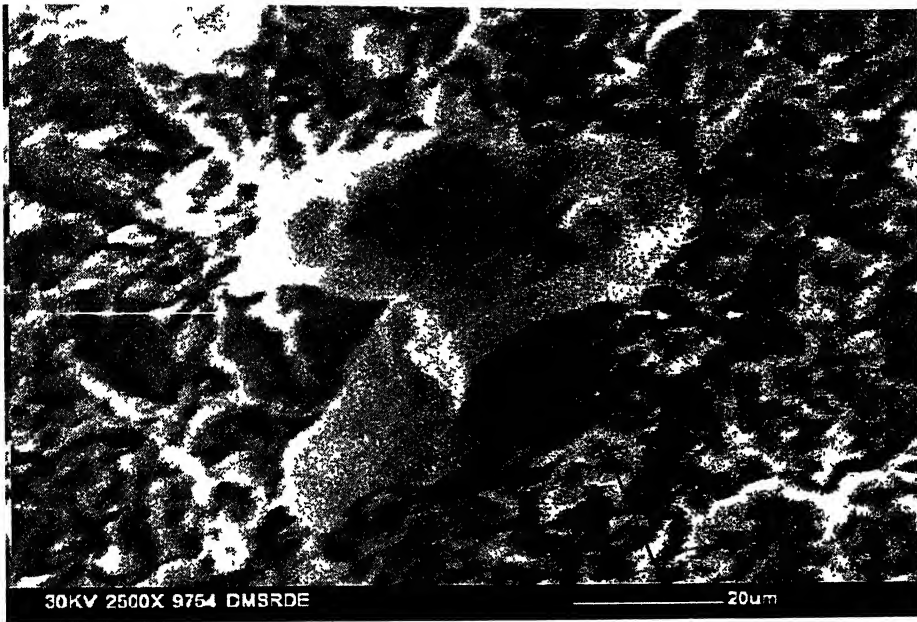
Figure 6.20 SEM photograph showing fracture surface at the periphery of the specimen TBRL2 (arrow is indicating the direction of initial shock propagation)
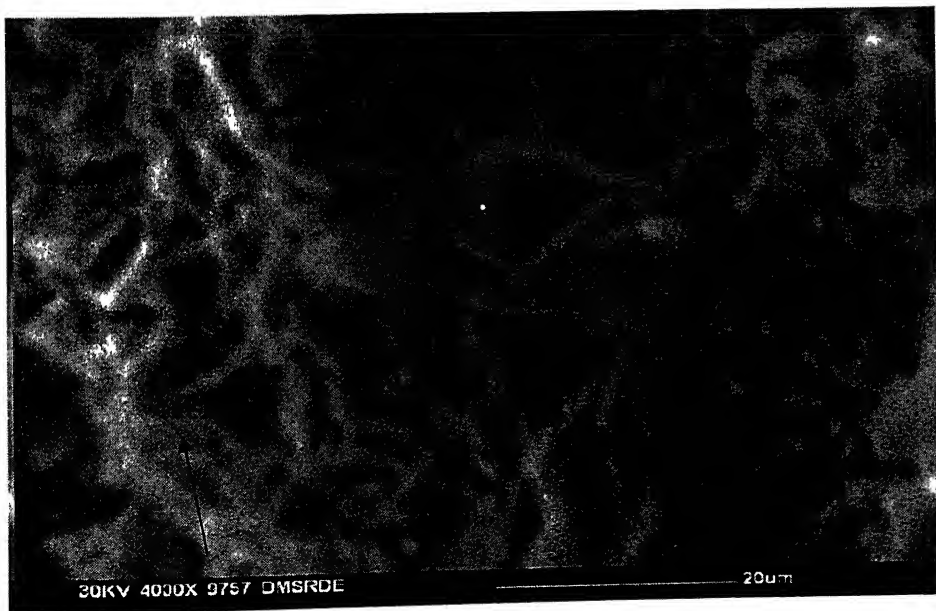


Figure 6.21 SEM photograph showing fracture surface at the periphery of the specimen TBRL2 (arrow is indicating the direction of initial shock propagation).
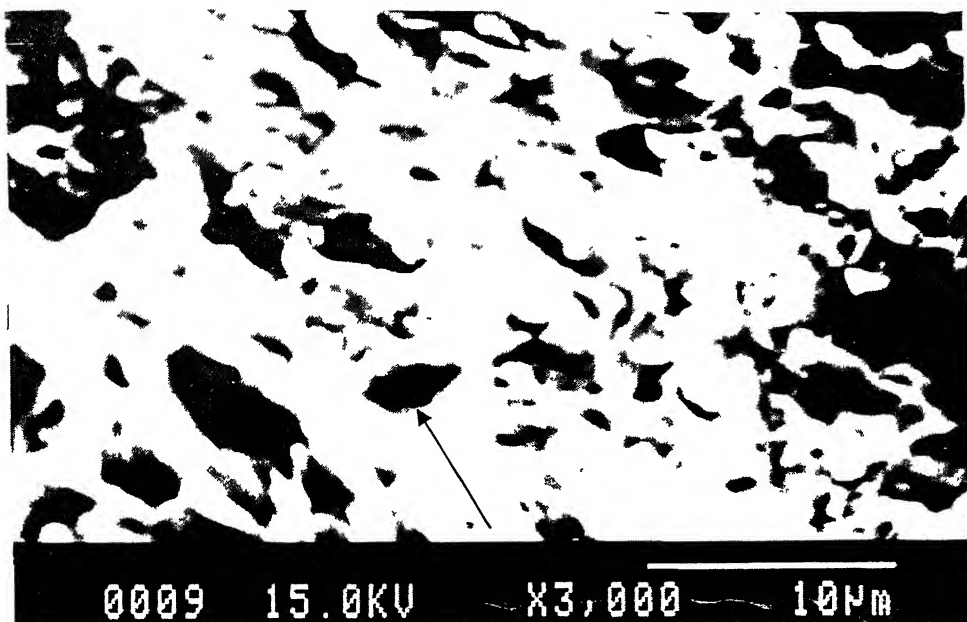
Figure 6.22 SEM photograph showing fracture surface at the periphery of the specimen TBRL2 (arrow is indicating the direction of initial shock propagation).

particles get folded by another particle. Such a behavior is shown in figure 6.21. Voids are present between the joined particles, as shown in Figure 6.22.

Figures 6.23-6.24 show the SEM photographs at the transverse cross-section, somewhere in between the centre and periphery of the explosive compacted specimen. There have been some cracks which were circumferential in nature. These cracks may be due to the tensile wave or compact density difference in the two regions. Figure 6.25 shows the folding of a powder particle near the crack area. This is very similar to that reported earlier. Figure 6.26 shows the SEM photograph of the area further towards the centre at the transverse cross-section. It can be seen that many powder particles are flaky in nature. The particles have come closer and have also joined together. However, some particles have elongated. Figure 6.27 shows a typical area, near the centre having elongated particles.

Figures 6.28-6.29 show the SEM photograph of TBRL3 explosive compacted specimen at its longitudinal cross-section near the periphery it can be seen that the particles have elongated and joined together. Further, joined elongated particles are getting folded by another elongated particle so as to form a bigger particle as shown in figure 6.29. Many of the interfaces between the particles do not show discontinuity (Figure 6.30). This observation is very much similar to that discussed earlier in case of TBRL2 specimen. Figure 6.31 shows a typical SEM photograph of TBRL3 specimen near the centre of its longitudinal cross-section. It can be seen that it consists of both elongated particles and partially folded and joined flaky particles. The partial folding of flakes and its subsequent joining leads to the formation of somewhat a porous mass, as shown in Figure 6.31. A feature of the SEM photographs is the absence of typical ductile fracture. Some Particle pull-out is evident from these photographs, which suggest that the metallurgical bonding between the particles at these locations is not very strong. However, it must be emphasized that these are clusters of particles which have been metallurgically bonded together very efficiently.
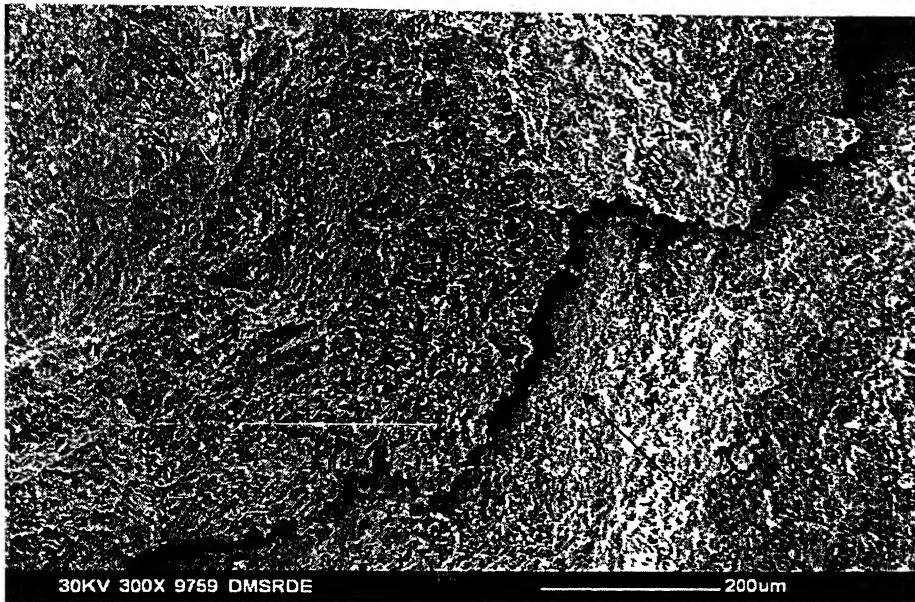
Figure 6.23 SEM photograph showing fracture surface in the region between periphery and the centre of the specimen TBRL2 (arrow is indicating the direction of shock propagation).
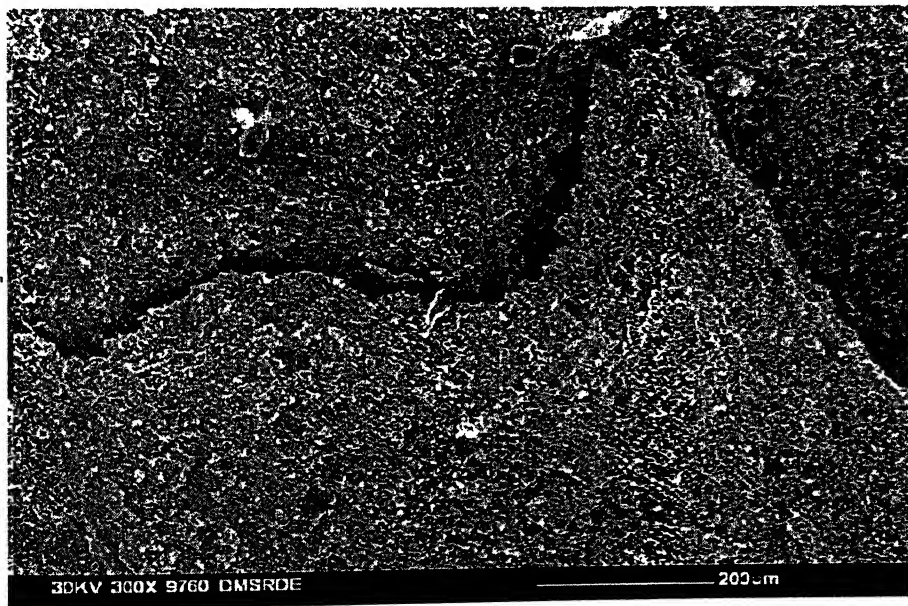


Figure 6.24 SEM photograph showing fracture surface in the region between periphery and the centre of the specimen TBRL2 (arrow is indicating the direction of shock propagation).

Figure 6.25 SEM photograph showing folded particle on the fracture surface in the region between periphery and the centre of the specimen TBRL2 (arrow is indicating the direction of shock propagation).
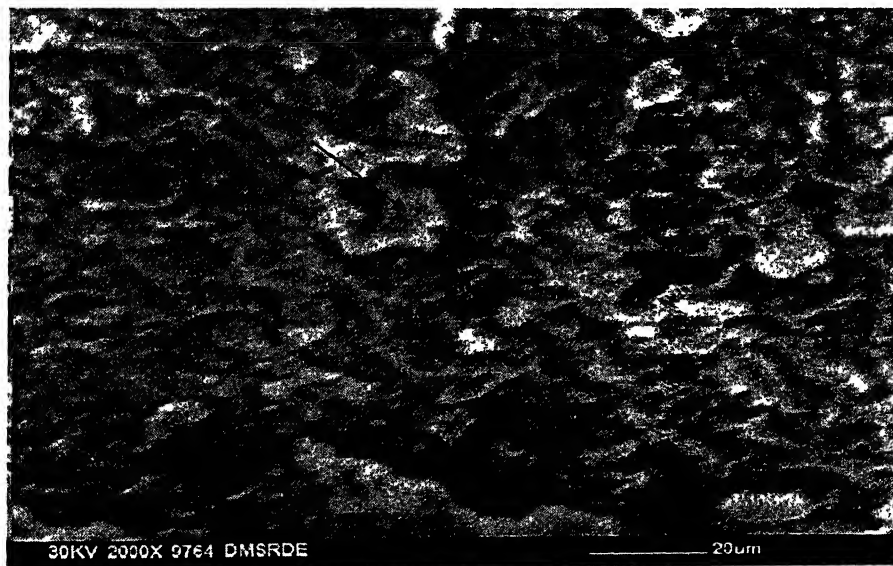


Figure 6.26 SEM photograph showing fracture surface of the region between periphery and the centre of the specimen TBRL2 (arrow is indicating the direction of shock propagation).
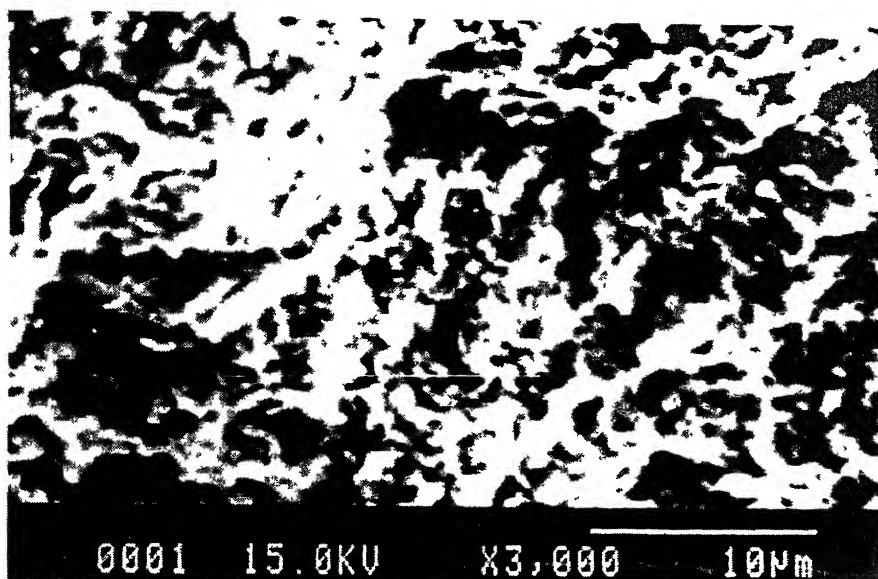
**Figure 6.27 SEM photograph showing fracture surface of the region near centre of the specimen TBRL2**



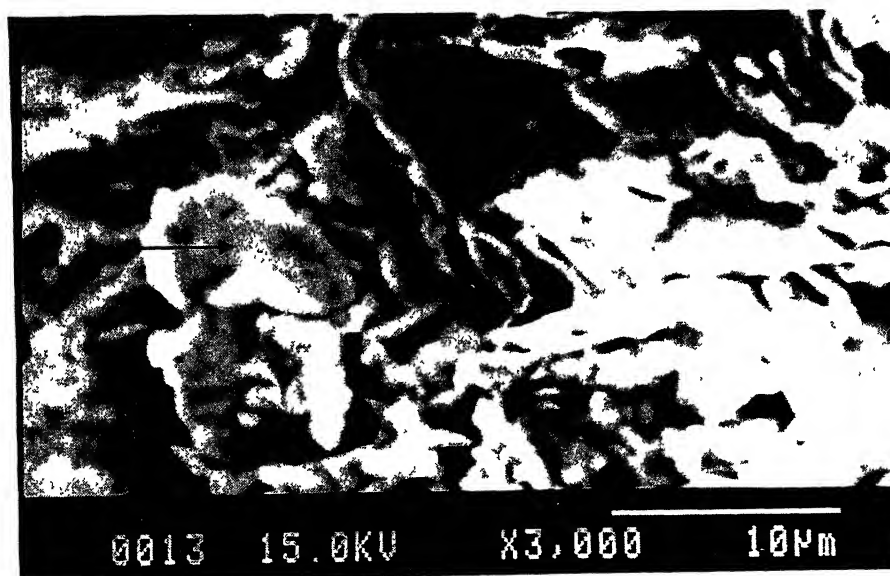**Figure 6.28 SEM photograph of the fracture surface of the region near periphery of the specimen TBRL3 (direction of shock propagation is shown by an arrow)**
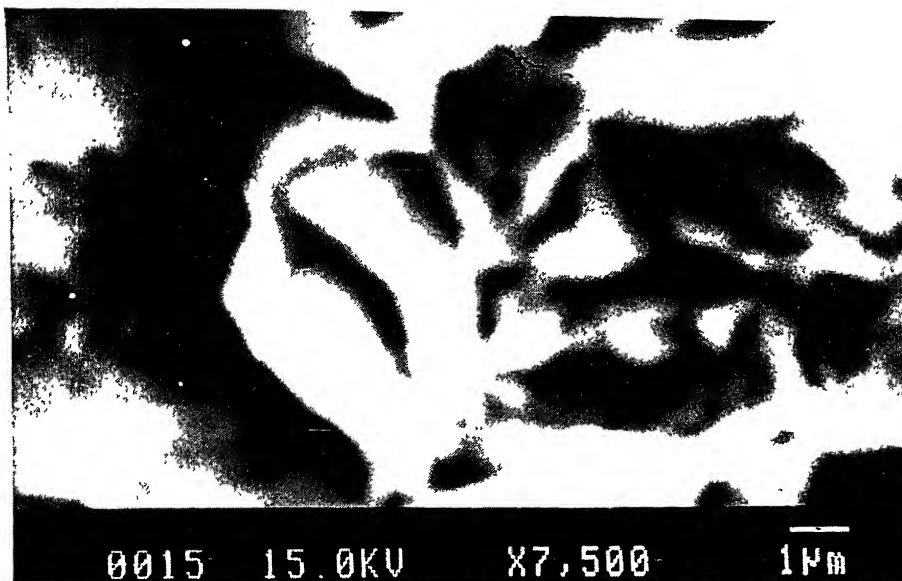
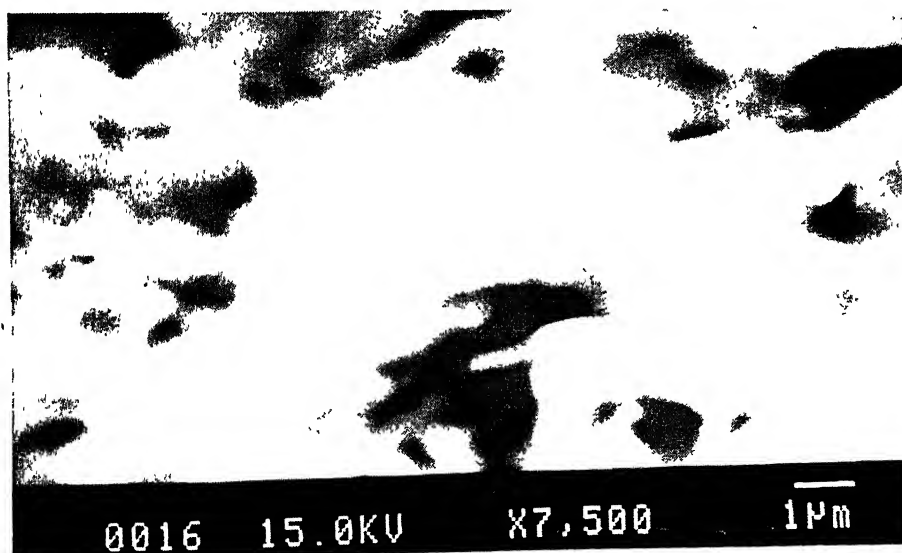**Figure 6.29 SEM photograph of the fracture surface of the region near periphery of the specimen TBRL3**



**Figure 6.30 SEM photograph of the fracture surface of the region near periphery of the specimen TBRL3 showing joining of particles at their edges**
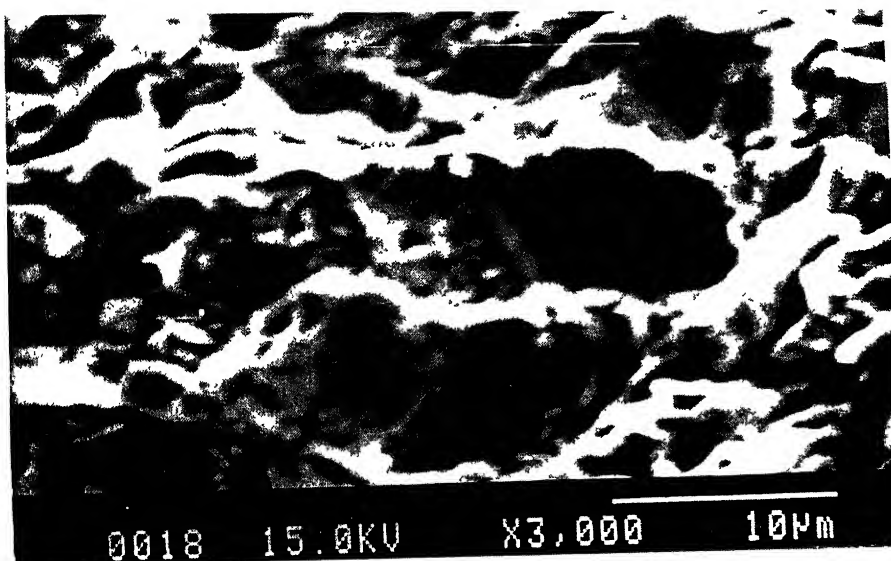
**Figure 6.31 A typical SEM photograph of the fracture surface of the region near centre of the specimen TBRL3**

Explosive compaction produces a concentration of energy within very localized regions at particle interfaces (Belyakov et al). Swartz et al have shown that peak temperatures as high as 1425 K (1152$^0$C) are produced during the explosive compaction of Copper and Constantan powders. Localized melting at particle interfaces is as important feature of explosive compacted metal powder. Evidence of any significant melting at the interface of MA 80Ni-15Fe-5Co was not observed. As described earlier, there were evidences of the folding of the MA 80Ni-15Fe-5Co powder particles during explosive compaction. Flaky or plate-like particles are subject to bending movements and very high concentrations of stresses, which are not present in the case of spherical powder (Gourdin 1986). This leads to folding of flaky particles.

For ascertaining densification in powder mass by explosive compaction, it is not only the total energy input is important, but also the energy flux over the particle surface (Gourdin 1986). Gourdin has described the relationship between the energy flux and the surface area of the powder particle (Gourdin 1984). The energy behind the shock wave is deposited at the surface of powder particles over the rise time of the compaction shock, which is given by

$$\tau = D/ v_s \qquad (13)$$

where D is a physical particle size, taken to be the median diameter, and $v_s$ is the shock speed. If the powder is brought to nearly full density by the passage of the first shock wave, most of the energy is deposited by this first shock. The net specific energy deposited in the powder by the compaction shock is then simply

$$E = E_s - E_r, \qquad (14)$$

where $E_s$ is energy behind the shock given by the Hugonoit relationship

$$E_s = (1/2)*P*(V_0-V) \qquad (15)$$

and $E_r$ is energy upon release. Here $V_0$ is the initial specific volume, and V and P are the specific volume and stress behind the shock wave, determined from the powder Hugonoit. The average flux incident on the surface of powder particles is just

$$F_0 = E/\tau A \tag{16}$$

where A is the measured specific area of the powder. This flux is assumed to be constant and uniform for a time $\tau$, after which it falls to zero and adiabatic conditions prevail. The energy flux associated with flaky powder reduces significantly, and the surface temperatures are correspondingly lower.

As the area-equivalent size decreases, the thermal diffusion distance decreases, and hence the time required for thermal equilibration. This would in turn lower the surface temperature for a given energy input. The area-equivalent size can decrease by a number of ways, such as irregularity, aspect ratio, etc. in other words, if the particle size is smaller than the energy is essentially dispersed throught the powder particle mass, and thermal equilibrium attains very rapidly. This explains why the surface temperature rise in the present case of flaky MA 80Ni-15Fe-5Co powder particles is not high, and effective metallurgical bonding between them has not taken place.

# 6.5 XRD STUDIES ON EXPLOSIVE COMPACTED 125 hr MILLED MA 80Ni–15Fe–5Co POWDER SAMPLES

## 6.5.1 Phase Identification in Explosive Compacted TBRL2 AND TBRL3 Samples

The XRD patterns of TBRL2 and TBRL3 samples are shown in Figures 6.32 and 6.33 respectively. These XRD patterns show predominantly three peaks. The intensity & d values of these peaks are shown in Table 6.6. These are in order of decreasing intensity in all diffraction patterns. On comparing intensities and d values with all the standard compounds of Ni, Fe, Co and oxygen i.e. $NiO$, $Ni_2O_3$, $CoO$, $Co_2O_3$, $Co_3O_4$, $FeO$, $Fe_2O_3$ and $Fe_3O_4$ which are shown in Appendix 1, it was concluded that no oxide peak was present in the XRD patterns of TBRL2 and TBRL3 samples, indicating absence of any substantial quantity of oxides.

The $2\theta$ values, Intensities, d values and corresponding planes of TBRL2, TBRL3, FeNi, $FeNi_3$, FeCo and $Co_3Fe_7$ are shown in Table 6.7. The $2\theta$ values, d values & Intensities of the peaks of TBRL2 and TBRL3 were compared with those of FeNi, $FeNi_3$, FeCo and $Co_3Fe_7$ for phase identification. The XRD patterns of the TBRL2 and TBRL3 have not been compared with ternary phase of Ni–Fe–Co alloy due to unavailability of XRD data of ternary alloys of Ni – Fe – Co. On comparing the $2\theta$ values, d values and intensities of TBRL2 and TBRL3 samples with those of FeNi, $FeNi_3$, FeCo and $Co_3Fe_7$ it was concluded that the first peak of the XRD patterns of the TBRL2 and TBRL3 both belongs to (111) $FeNi_3$, (111) FeNi, (110) FeCo and (110) $Co_3Fe_7$, whereas second peak of both the samples belongs to (200) $FeNi_3$ and (200) FeNi. Further the identification of third peak of both the samples shows that this peak belongs to (220) FeNi and (220) $FeNi_3$. From the above analysis it can be concluded that TBRL2 and TBRL3 are solid solution of Fe and Co in Ni. In both the samples, $FeNi_3$ (an intermetallic compound having face centered cubic crystal structure) is the predominant phase present whereas FeNi, FeCo and $Co_3Fe_7$ phases are also present in the system. The data from JCPDS files show that crystal structure of all the phases present in this system is cubic in nature. Hence it can be predicted that crystal structure of the system will also be cubic.
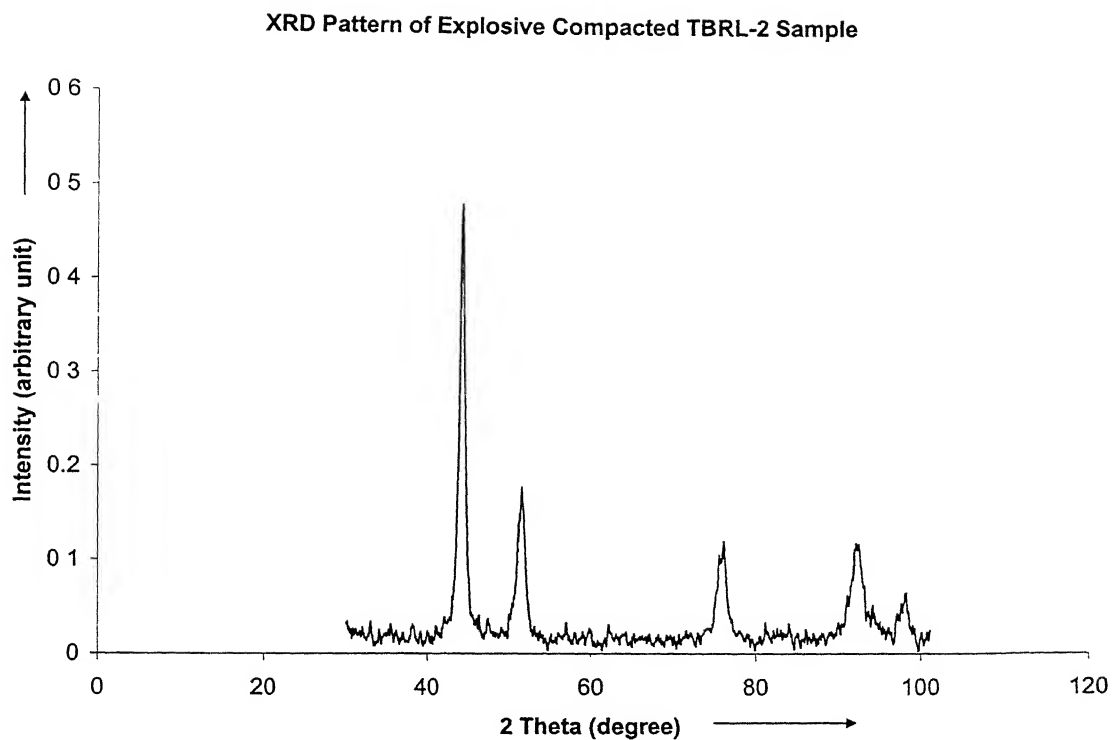
**Figure 6.32 XRD pattern of explosive compacted TBRL2 sample**
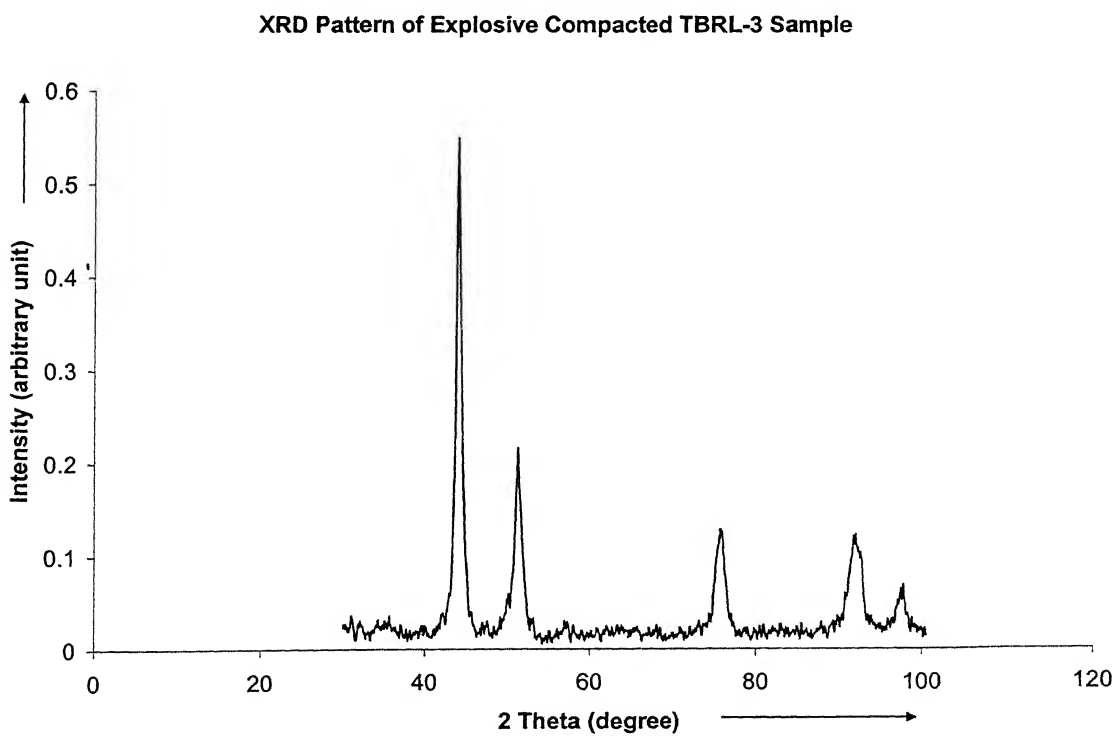


**Figure 6.33 XRD pattern of explosive compacted TBRL3 sample**

**Table 6.6 Intensities and d-values of different peaks of XRD patterns of TBRL2 and TBRL3 samples**

| S.No. | Sample Identification | Peak Intensities (%) | d (A$^0$) |
|---|---|---|---|
| 1. | TBRL2 | 99 | 2.05 |
|  |  | 37 | 1.77 |
|  |  | 25 | 1.25 |
| 2. | TBRL3 | 100 | 2.05 |
|  |  | 39 | 1.78 |
|  |  | 23 | 1.25 |

**Table 6.7 Intensities, 2θ values, d-values and corresponding planes of TBRL2, TBRL3, FeNi, FeNi₃, FeCo and Co₃Fe₇**

| S. No. | Alloy-System/ Compound | Intensity (%) | Angle (2θ) (degree) | d-values (A⁰) | (hkl) |
|--------|------------------------|---------------|---------------------|---------------|-------|
| 1. | TBRL2 | 99<br>37<br>25 | 44.19<br>51.53<br>76.07 | 2.05<br>1.77<br>1.25 | ----<br>----<br>----<br>---- |
| 2. | TBRL3 | 100<br>39<br>23 | 44.23<br>51.45<br>75.95 | 2.05<br>1.78<br>1.25 | ----<br>----<br>---- |
| 3. | FeNi | 100<br>100<br>100 | 43.51<br>50.72<br>74.75 | 2.08<br>1.8<br>1.27 | (111)<br>(200)<br>(220) |
| 4. | FeNi₃ | 100<br>60<br>40<br>30 | 44.32<br>51.58<br>92.30<br>75.94 | 2.04<br>1.77<br>1.07<br>1.25 | (111)<br>(200)<br>(311)<br>(220) |
| 5. | CoFe | 100<br>25<br>14 | 44.87<br>82.74<br>65.32 | 2.02<br>1.17<br>1.43 | (110)<br>(211)<br>(200) |
| 6. | Co₃Fe₇ | 100<br>36<br>25 | 44.76<br>82.50<br>65.16 | 2.025<br>1.17<br>1.43 | (110)<br>(211)<br>(200) |

Figure 6.34 compares the XRD patterns of pure Ni with that of TBRL2 and TBRL3 samples. It can be seen that there is no extra peak in the XRD patterns of TBRL2 and TBRL3 samples as compared to that of pure Ni. Intensity of the peaks at higher angles in TBRL2 and TBRL3 is very small or rather peaks are disappearing. This disappearance of peaks at higher angles indicates the partial amorphization of the system. From the above it can be concluded that since Ni has an FCC structure, the crystal structure of the phases present in TBRL2 and TBRL3 samples is also FCC.

## 6.5.2 Determination of Crystallite size of Explosive Compacted TBRL2 and TBRL3 samples

Crystallite size of the explosive compacted TBRL2 and TBRL3 samples, was determined from the respective XRD patterns, as shown in Figures 6.32 and 6.33 respectively, using X-ray broadening technique while taking two major peaks (111) and (220) into consideration. The profile shape function of the type Pseudo-Voigt was filled on the smoothened X-ray data of Figures 6.32 and 6.33. In order to get the real FWHM of the samples, the instrumental broadening was removed. For this purpose, XRD patterns of standard sample of pure silicon was obtained using the same experimental parameters as used in the sample of explosive compacted TBRL2 and TBRL3 samples.

From this data of silicon instrumental broadening effect in the XRD patterns of the explosive compacted TBRL2 and TBRL3 samples was removed. The FWHM obtained after r emoval o f i nstrumental b roadening e ffect, w as u sed t o d etermine c rystallite s ize using Scherrer's formula. The values of fit of 2θ and FWHM for explosive compacted TBRL2 and TBRL3 samples were calculated and are shown in Table 6.8. The crystallite size of the explosive compacted TBRL2 and TBRL3 samples was calculated for the plane (111) and (200) using equation (11), and these are also shown in Table 6.7.

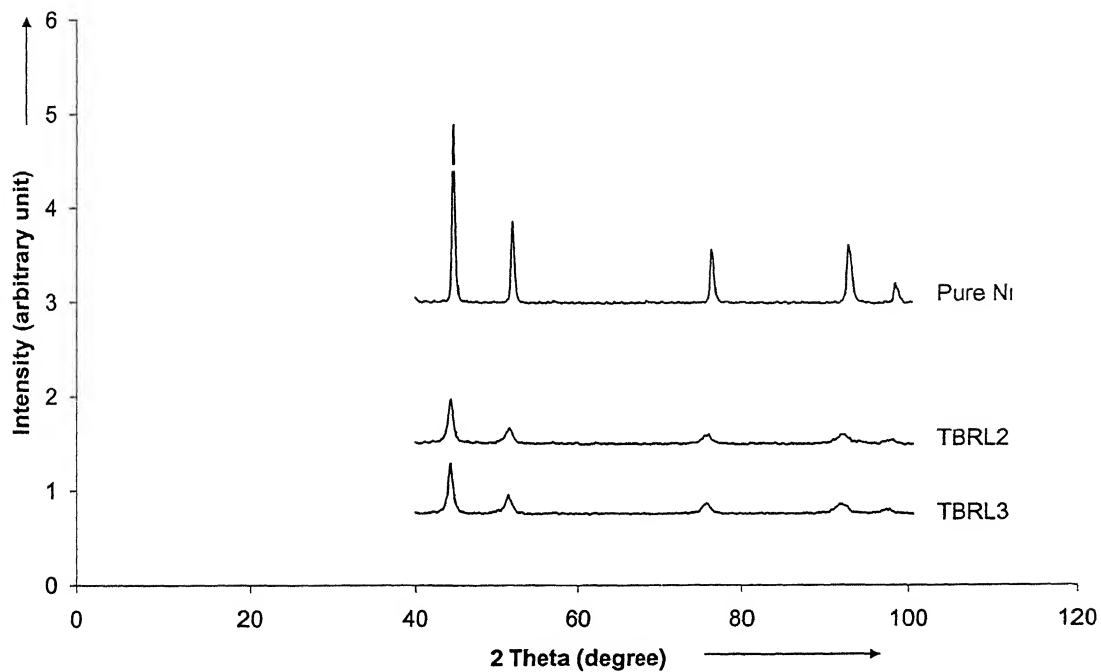**Comparison of XRD Patterns of Pure Ni, TBRL2 and TBRL3**

**Figure 6.34 Comparison of XRD patterns of TBRL2 and TBRL3 with XRD pattern of Pure Ni**

**Table 6.8 Angle (2θ) and FWHM values obtained from the Pseudo-Voigt curve fitting on experimental XRD data of explosive compacted TBRL2 and TBRL3 samples and the calculated grain size.**

| Sample Designation | 2θ values (degree) | | FWHM (degree) | | Grain Size (nm) | |
|---|---|---|---|---|---|---|
| | (111) | (200) | (111) | (200) | (111) | (200) |
| TBRL2 | 44.12 | 51.41 | 0.708 | 1.115 | 15 | 9 |
| TBRL3 | 44.06 | 51.30 | 0.712 | 1.047 | 15 | 9 |

## 6.6 TEM ANALYSIS OF EXPLOSIVE COMPACTED MA NANOCRYSTALLINE 80Ni-15Fe-5Co POWDER
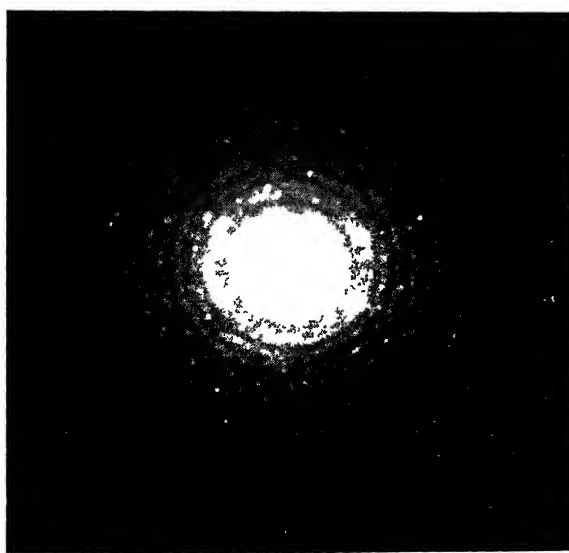
A bright field TEM micrograph of one of the regions of the explosive compacted TBRL2 is shown in Figure 6.35a whereas the corresponding SADP is shown in Figure 6.35b. The TEM image shown in this figure reveals the nanocrystalline character of the structure which can be inferred from the SADP corresponding to the above region. This indicates possible formation of some new phases during the compaction process. The crystallite size was estimated in the range between 10-50 nanometer (nm). TEM micrograph of another area of TBRL2 sample, shown in Figure 6.36a clearly shows well defined crystallites in the size range 10-50 nm. The SADP corresponding to the above area, shown in Figure 6.36b, clearly supports the estimation while showing very fine rings. The SADP confirms the polycrystalline nature of the region.

Another bright field TEM micrograph of TBRL2 is shown in Figure 6.37a. The dark areas visible in the figure are the crystallized regions. The crystallites sizes in this figure are in the nanocrystalline range. However, the featureless region in the image may still correspond to the amorphised region. The crystallized regions could have been formed from the molten regions during compaction. In the molten region, there could have been a large number of heterogeneities so that crystallites could have been nucleated in large numbers thus leading to the nanocrystalline character. Much more strong evidence of the phase transformation during compaction can be seen from SADP pattern, shown in the Figure 6.37b, of the area shown in Figure 6.37a. The diffraction clearly supports the above argument while showing emergence of many new sharp rings in the SADP.

Figure 6.38a shows the bright field TEM image of TBRL3 sample while corresponding SADP is shown in Figure 6.38b. The image shows well defined crystallites in the size range of 10-30 nm. The SADP shows that rings are very sharp in nature indicating well defined crystalline nature of the sample whereas the appearance of many new rings indicates the formation of new phases.
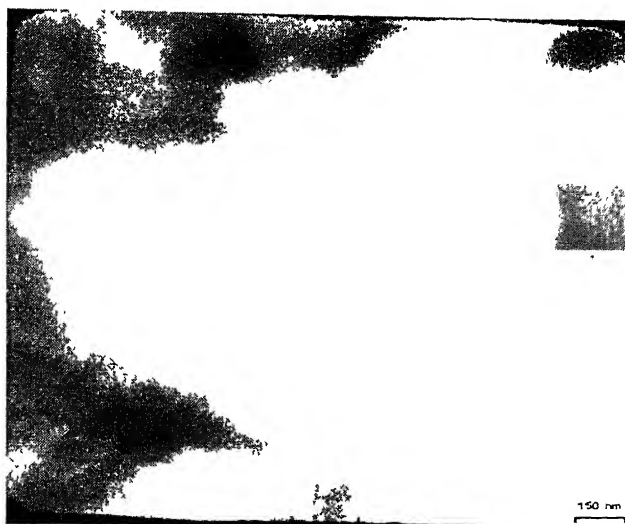
(a)



(b)

**Figure 6.35:** (a) Bright field TEM micrograph of TBRL2 and (b) corresponding Selected Area Diffraction Pattern (SADP)
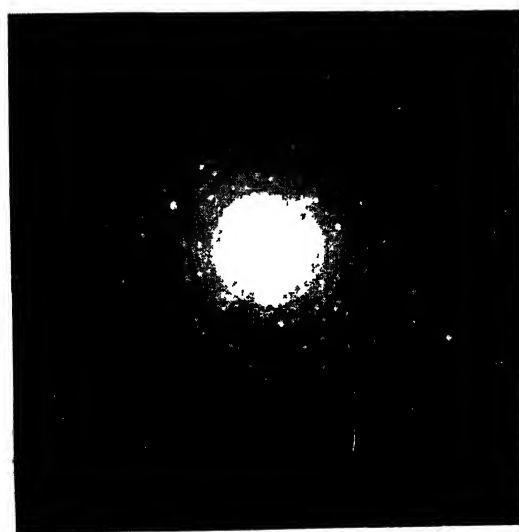
(a)



(b)

Figure 6.36: (a) Bright field TEM micrograph of TBRL2 and (b) corresponding Selected Area Diffraction Pattern (SADP)

(a)



(b)

Figure 6.37: (a) Bright field TEM micrograph of TBRL2 and (b) corresponding Selected Area Diffraction Pattern (SADP)

(a)
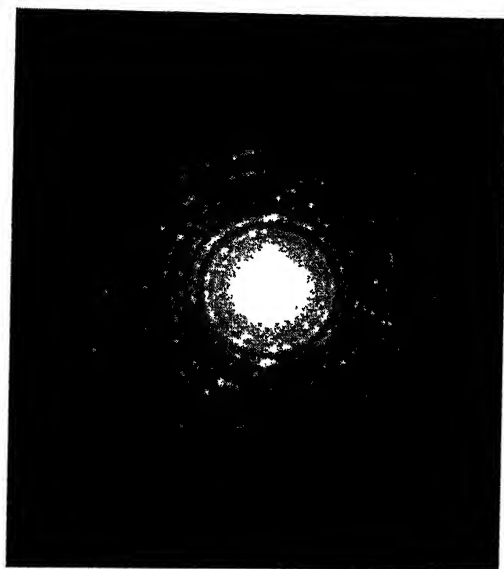


(b)

**Figure 6.38: (a) Bright field TEM micrograph of TBRL3 and (b) corresponding Selected Area Diffraction Pattern (SADP)**

Another bright field TEM image of TBRL3 is shown in Figure 6.39a while the corresponding SADP is shown in Figure 6.39b. Though the image does not show any well defined crystallites but the diffraction pattern clearly shows the polycrystalline character. The SADP gives the clear indication of crystallite size being in nanocrystalline range. In comparison with Figure 6.35, we may infer the crystallite size here is much finer, many be in the range of 20 nm or finer.
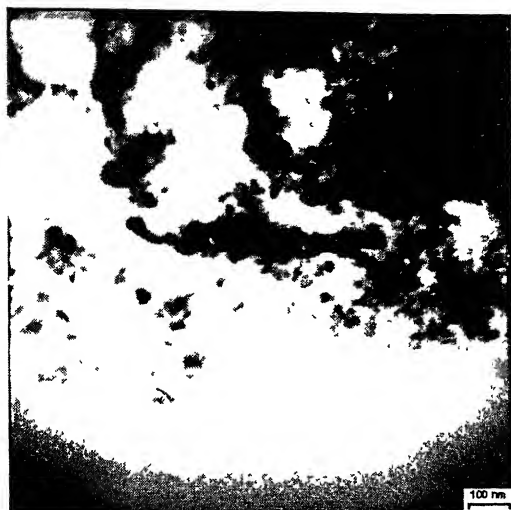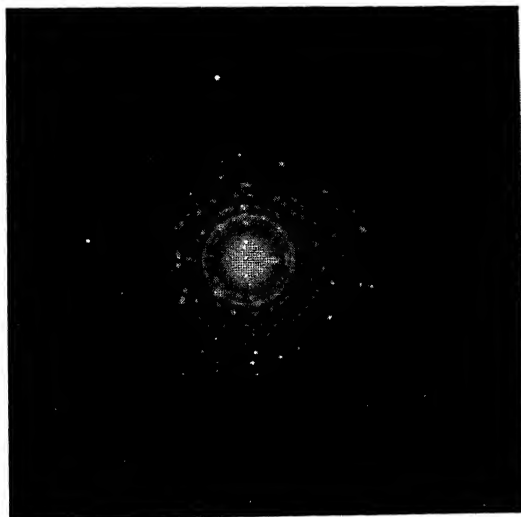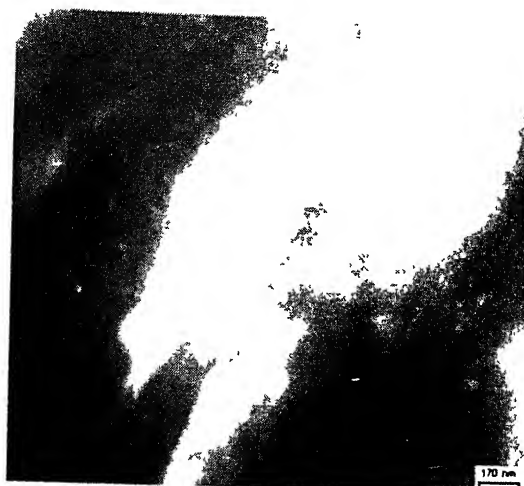
(a)



(b)

Figure 6.39: (a) Bright field TEM micrograph of TBRL3 and (b) corresponding Selected Area Diffraction Pattern (SADP)

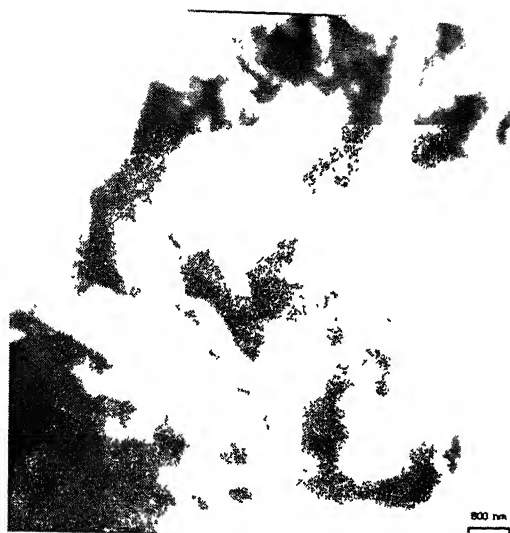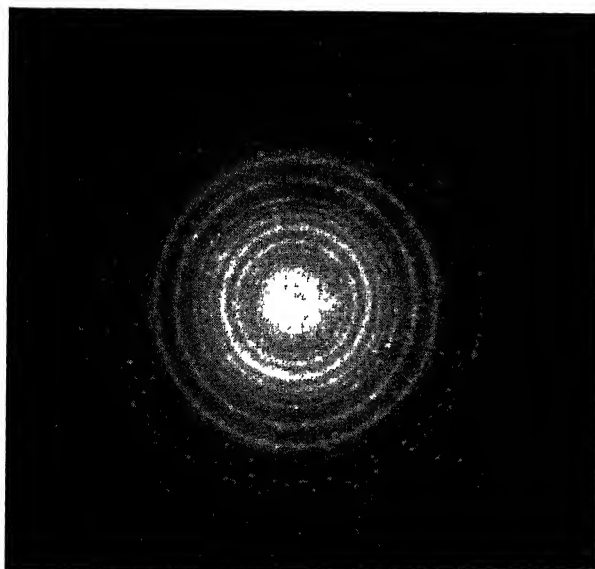## 6.7 MAGNETIC PROPERTIES OF EXPLOSIVE COMPACTED MA NANOCRYSTALLINE 80Ni-15Fe-5Co COMPACTS

Magnetic properties of explosive compacted TBRL2 and TBRL3 samples were determined using Vibrating Sample Magnetometer (VSM). The saturation magnetization ($M_s$), remanence, coercivity and Curie temperatures were determined from the data obtained.

### 6.7.1 Determination of Curie Temperature

Curie temperature is the temperature at which a material changes its behavior from ferromagnetic tom paramagnetic. Figure 6.36 shows the temperature dependence of magnetization for TBRL2 sample. It can be seen that magnetization remains more or less constant till it reaches Curie temperature. The observed value of Curie temperature was found to be approximately $625^0$C (898 K).

The temperature dependence of magnetization for TBRL3 is shown in Figure 6.37. It can be observed that the curve for TBRL3 shows the same behavior as that of TBRL2. The Curie temperature for TBRL3 was found to be $626^0$C (899 K) which is almost same as that of TBRL3. The Curie temperature of Ni is affected by various factors including the prior mechanical and thermal treatment of the specimen and the nature and amount of impurities present. The Curie point of pure Ni falls between $350^0$C-$360^0$C. Most alloying elements lower the Curie point of Ni but Co and Fe are exceptions, which increase the Curie temperature. The increase in the Curie point appears to be due to the addition of 15 wt% Fe and 5 wt% Co. Another factor that could have resulted in increase in Curie temperature is the nanoscale crystallite size as also reported by E. Jartychet et al for Ni-Fe alloy.

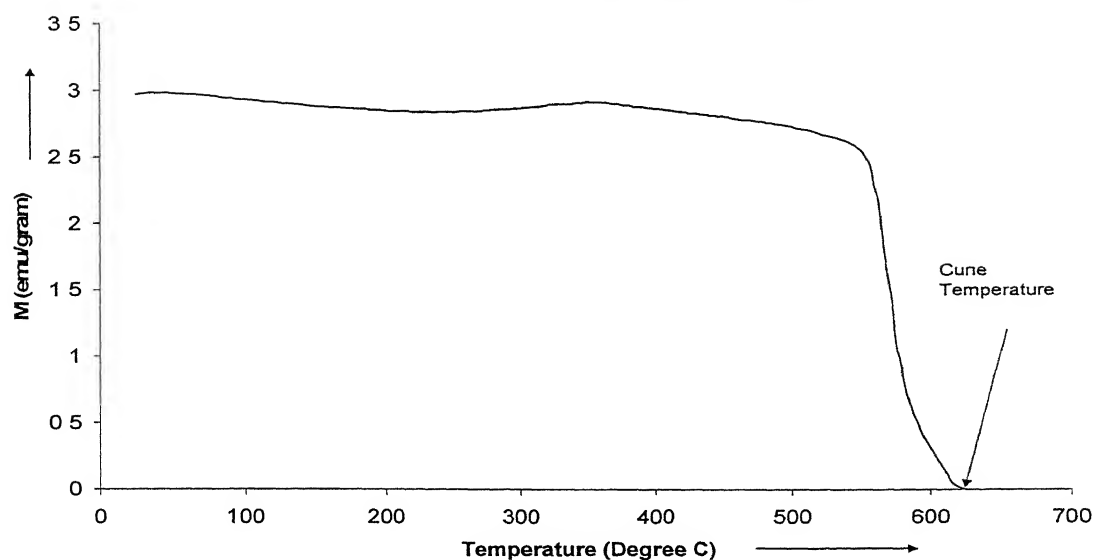**Figure 6.36 Temperature dependence of magnetization of TBRL2**
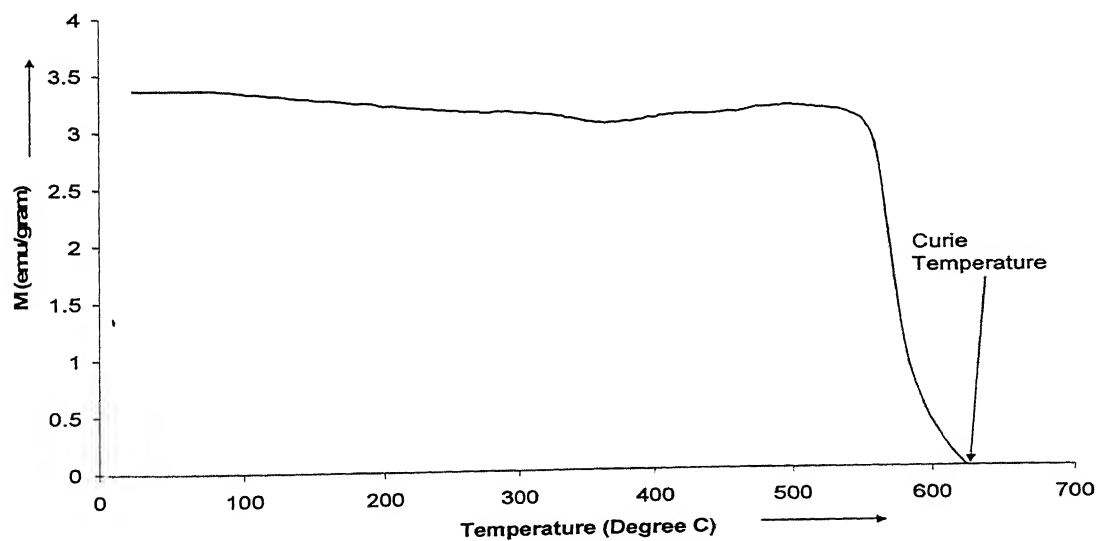


**Figure 6.37 Temperature dependence of magnetization of TBRL3**

146

## 6.7.2 Determination of Saturation Magnetization

Figure 6.38 and 6.39 show the field dependence of magnetization at room temperature for TBRL2 and TBRL3 respectively. It can be seen that in both the cases saturation in magnetization is attained on application of magnetic field greater than 0.8 Tesla. Beyond this point, any increase in the applied magnetic field does not increase magnetization. The value of saturation magnetization was found to be approximately 80 emu/g for both the samples. From the Figures 6.38 and 6.39, it can also be seen that the initial part of the curves, which traces straight line, has steep slope and the point of initial permeability and maximum permeability are coinciding at the same point on the curves. This feature is an indication of high initial permeability of the material. The high saturation magnetization can be attributed to the presence of $FeNi_3$ intermetallic compound as $M_s$ is increased due to the formation of $FeNi_3$. This is attributed to the well known increase of the Fe magnetic moment upon alloying with alloying with Ni while the Ni moment is almost constant.

## 6.7.3 Determination of Remanence and Coercivity

The hysteresis curve for TBRL2 and TBRL3 are shown in Figures 6.40 and 6.41 respectively. With the help of hysteresis curves, the remanence and coercivity of TBRL2 and TBRL3 were determined. The remanence and coercivity values for TBRL2 were found to be 0.95 emu/g and 0.0002 Tesla respectively. In case of TBRL3 the remanence and coercivity were found to be 0.80 emu/g and 0.0001 Tesla respectively. It can be seen from the Figures 6.40 and 6.41 that the area of the hysteresis loop is very small and lines are almost tracing back the same path. It can be deduced from this feature that the energy product for TBRL2 and TBRL3 is very small, thus core loss will be very small or negligible. Hence it can be predicted safely that if material is placed in changing magnetic field, hysteresis loss would be negligible in amount.
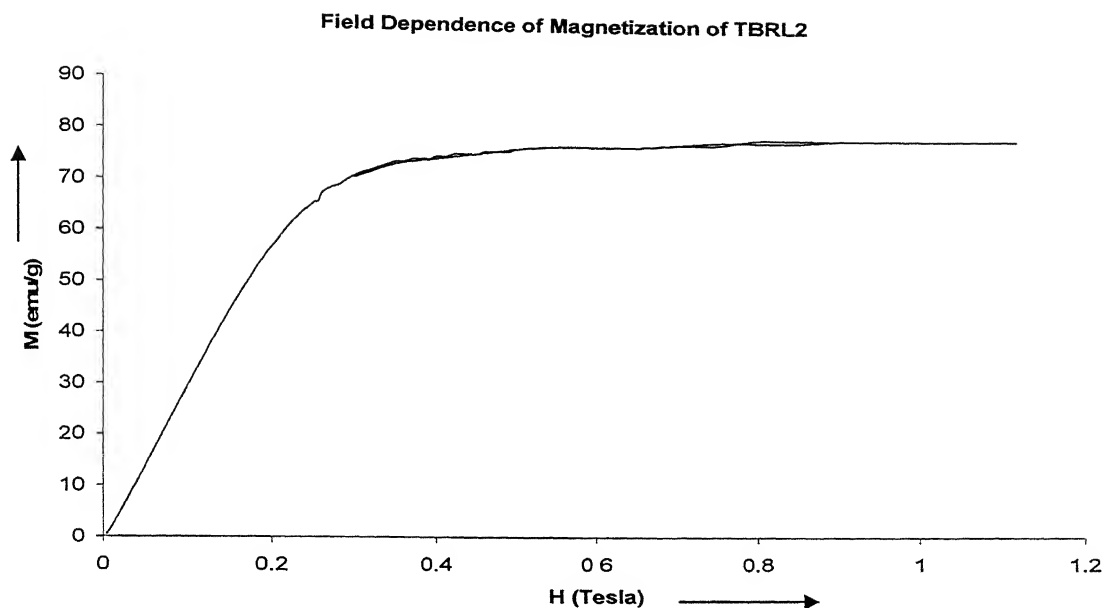
**Figure 6.38 Field dependence of magnetization of explosive compacted TBRL2**



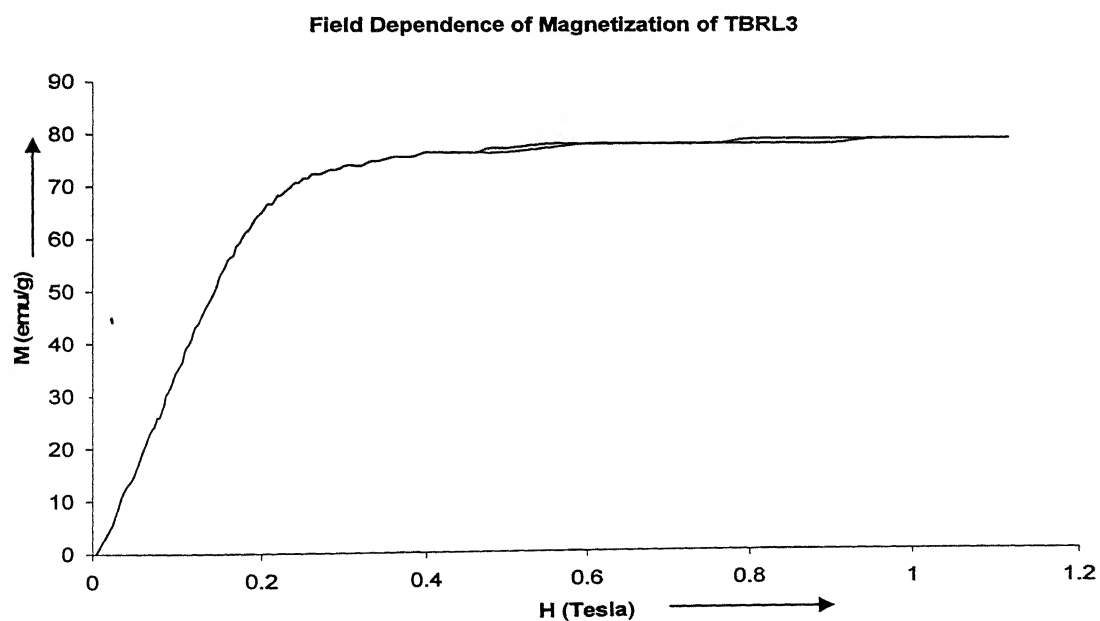**Figure 6.39 Field dependence of magnetization of explosive compacted TBRL3**

**M-H Curve of TBRL2**
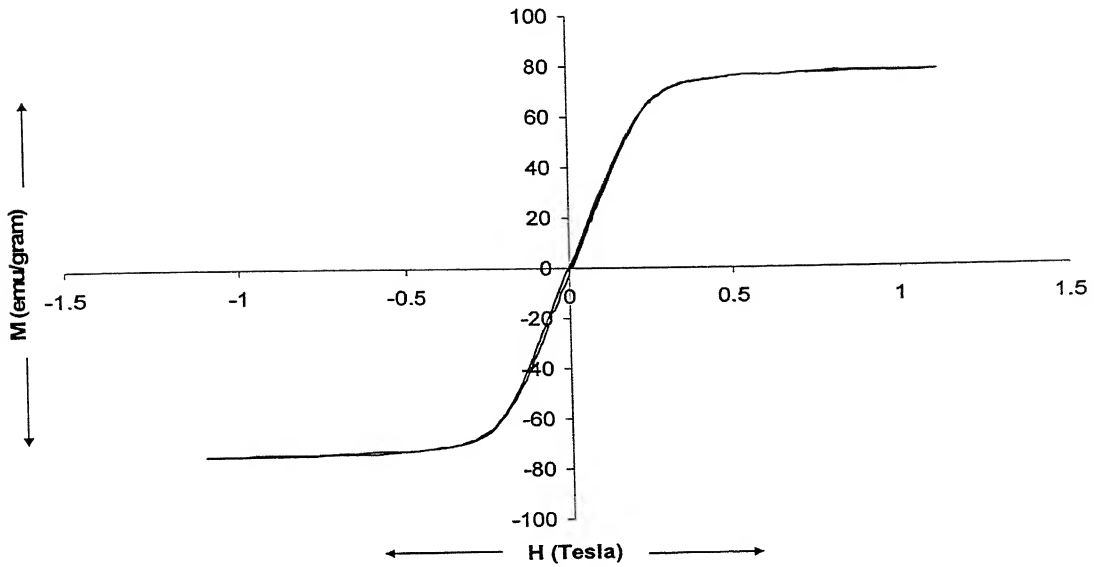


Figure 6.40 Hysteresis curve of explosive compacted TBRL2

**M-H curve of TBRL3**
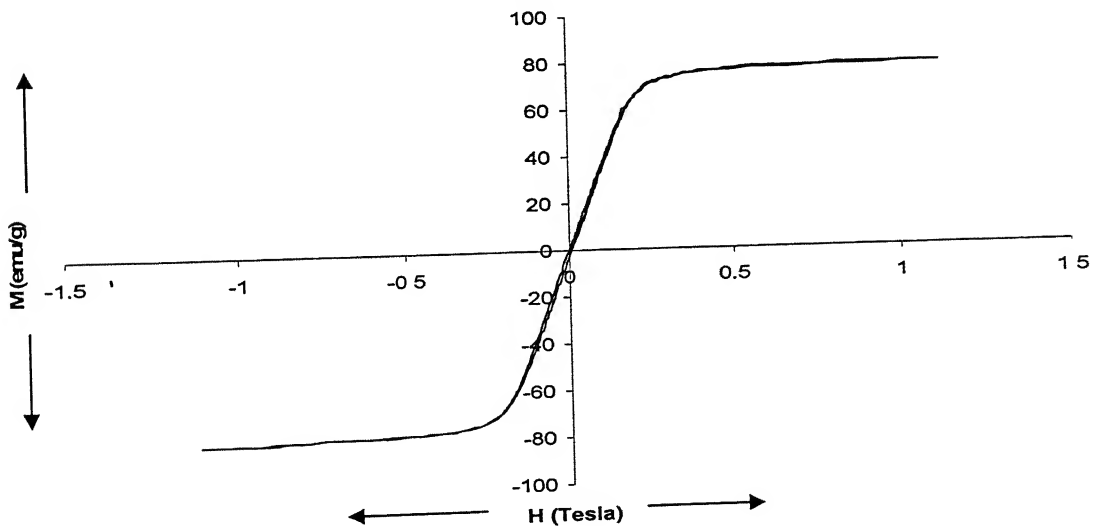


Figure 6.41 Hysteresis curve of explosive compacted TBRL3

The primary requirements for a good soft magnetic materials are high initial permeability, high saturation magnetization, low coercivity and low core loss. The values of different magnetic properties of TBRL2 and TBRL3 are shown in Table 6.9. The present study shows that improved magnetic properties as compared to nanocrystalline 80Ni-20Fe and pure Ni have been found. The Curie temperature ($T_c = 625^0C$) has been found to be improved as compared to pure Ni ($T_c = 350^0C$) [ASM Materials Handbook] and nanocrystalline 80Ni-20Fe ($T_c = 525^0C$) [Shyam Kumar 2002]. From the above analysis and the values of various magnetic properties stated in Table 6.9, it can be concluded that the explosive compacted MA nanocrystalline 80Ni-15Fe-5Co shows high Curie temperature, high saturation magnetization, high initial permeability, low coercivity, low remanence and low core loss which make it an excellent soft magnetic material for use in applications such as communication equipments and applications requiring reversal of direction of magnetization.

**Table 6.9 Values of different magnetic properties of TBRL2 and TBRL3**

| Sample Designation | Saturation Magnetization (emu/g) | Remanence (emu/g) | Coercivity (Tesla) | Curie Temperature (degree C) | Field Strength of Saturation Magnetization (Tesla) |
|---|---|---|---|---|---|
| TBRL2 | 80 | 0.95 | 0.0002 | 625 | 0.8 |
| TBRL3 | 80 | 0.80 | 0.0001 | 626 | 0.8 |

The following conclusions can be drawn on the basis of the results and discussion:

1. The MA nanocrystalline 80Ni-15Fe-5Co powder was successfully produced by High Energy Ball Milling of Nickel, Iron and Cobalt powders.

2. Phase identification, using XRD technique, shows that $FeNi_3$, $FeNi$, $FeCo$, and $Co_3Fe_7$ are the predominant phases present in the system.

3. The crystallite size decreases with milling time. The rate of decrease of crystallite size is very rapid between 15 min. - 12 hr milling time. After 125 hr of milling time, the crystallite size was stabilized and no decrease in size was observed. At 125 hr of milling time, the crystallite size was found to be 9 nm.

4. The grain growth kinetics for shorter period of time at low temperature annealing ($500^0C$) for 125 hr milled MA nanocrystalline 80Ni-15Fe-5Co powder shows that during the first 10 min. the grain size increases rapidly and the crystallite size increases to 40 nm from 9 nm. Beyond this period of time, the grain growth becomes sluggish and a level off trend has been observed.

5. It has been possible to form bulk samples of 125 hr milled MA nanocrystalline 80Ni-15Fe-5Co powder via explosive compaction technique. A very high bulk density of 90% of the theoretical density was obtained in the explosive compacted samples.

6. The nanocrystalline nature in the explosive compacted compacts was retained. After explosive compaction, the crystallite size was found to be 15 nm.

7.  Superior magnetic properties were obtained such as high Curie temperature, high saturation magnetization, high initial permeability, almost zero coercivity and negligible remanence.

8.  The present study shows that MA nanocrystalline 80Ni-15Fe-5Co powder obtained by Powder Metallurgy route based on mechanical alloying and explosive compaction can be used to as an excellent soft magnetic material.

# 7. SUGGESTIONS FOR FUTURE WORK

The following are being suggested for future work in this area:

1. A more extensive study of the explosive compaction behavior of the MA nanocrystalline 80Ni-15Fe-5Co powder is required with respect to the effect of the amount and type of charge on the resulting density in the compact.

2. The isothermal annealing of the MA nanocrystalline 80Ni-15Fe-5Co powder at various temperatures and times should be studied in order to find out the complete grain growth behavior of such materials.

3. Compaction of MA nanocrystalline 80Ni-15Fe-5Co powder by other methods such as Spark Plasma Sintering should be tried.

4. The effect of the amount of cobalt on the resulting magnetic properties of the Ni-Fe-Co system should be investigated.

# *References*

**Andrievski 2001:** Andrievski, R.A. and Glezer, A.M. (2001) Scripta Mater., 44, 1621-1624.

**Ansara 1996:** Ansara, I., 'Phase diagrams and thermodynamics', in "The iron-nickel alloys" (eds.G.Beranger et al.), 1996, Lavoisier, NY, p.149-150.

**Baibich 1988:** Baibich, M.N. et al, Phys. Rev. Lett., 61(1988), 2472-2475.

**Bas et al 2003:** Bas, J.A., Calero, J.A. and Dougan, M.J., J.Magn.Magn.Mater, 254-255(2003), 391-398.

**Beck and Siegel 1992:** Beck, D.D. and Siegel, R.W., J.Mater.Res., vol.7(1992), p.2840.

**Bhaduri and Bhaduri 1998:** Bhaduri, S. and Bhaduri, S.B., JOM, 50(1) (1998), 44.

**Bhushan 1995:** Bhushan, B., Handbook of Micro/Nano Tribology (ed. B. Bhushan), CRC Press, New York, NY, (1995).

**Binnig et al. 1986:** Binnig,G., Quate, C.F. and Gerber, C., Phys.Rev.Lett.56(1986), 930.

**Birringer 1989:** Birringer, R., Mater. Sci. and Engg., A117(1989), 33-43.

**Brundle et al. 2002:** Brundle et al (2002) Encyclopedia of Materials Characterization, Ed. Brundle, Evans and Wilson, Butterworth-Heinemann.

**Collingon 1999:** Collingon, J.S., 'Physical Vapor Deposition' in"Non Equilibrium Processing of Materials", Capter 9, Ed. C.Suryanarayana, Pergamon, 1999.

**Couderchon et al. 1996:** Couderchon, G. and Porteseil, J.L., 'Some properties of nickel rich commercial Fe-Ni Alloys', in "The iron-nickel alloys", (eds. G. Beranger et al.), 1996, Lavoisier, NY, p.29-58.

**Dogan et al. 1994:** Dogan, C.P., Rawers, J.C., Givier, R.D. and Korth, G., Nanostr. Mater, 4(1994), 631.

**Eifert 2000:** Eifert, H., Kupp, D.and Gunther, B., Powder Metall., vol. 43, No. 4, (2000), 310-313.

**Erb 1995:** Erb, U., NanoStructured Mater., 6(1995), 533.

**Gilman and Benjamin 1983:** Gilman, P.S. and Benjamin, J.S., Ann. Rev. Mater. Sci., 13(1983), 279.

**Glade and Thadani 1995:** Glade, S.C. and Thadani, N.N., Metall. Mater.Trans., 26A(1995), 2656.

**Gleiter 1989:** Gleiter, H. (1989) Progress in Materials Science, vol.33, pp.223-315.

**Gleiter 1991:** Gleiter, H., J.Appl.Cryst., 24(1991), 79-90.

**Gleiter 1995:** Gleiter, H., Z.Metalkd. 86(1995)2, 78-83.

**Gleiter 1998:** Gleiter, H., Prog.Mater.Sci., 33(1998), 223.

**Gleiter 2000:** Gleiter, H., Acta Mater., 48(2000), 1-29.

**Gleiter 1993:** Gleiter, H., in "Mechanical Properties and Deformation Behavior of Materials having Ultrafine Microstructure", ed. M.Nastasi and M.Parkin-*, NATO Adv. Study Inst. Series E, Applied Science, Vol. 233, Kluwer, Dordrecht, 1993, p.3.

**Goodhew et al. 1988:** Goodhew, P.J. and Humphrey, F.J., in "Electron Microscopy and Analysis", 1988, pp. 99-104, Taylor and Francis, London, second ed.

**Grossard 1969:** Grossard, A.C., Thin Solid films, 57(1979), 3.

**Groza 1999:** Groza, J.R., Chapter 13, Non-Equilibrium Processing of Materials,

Pergamon, (1999), Editor C.Suryanarayana.

**Hansma 1996:** Hansma, H.G, J. Vac. Sci. Technol., B14(1996), 1390 .

**Haubold et al. 1989:** Haubold, T., Birringer, R., Lengler, B. and Gleiter, H, Physics Letters A, Vol.135, No.8, (1989), 9. .

**Herr et al. 1990:** Herr, U., Jing, J., Gonser, U., & Gleiter, H., Solid State Commun. , 76(1990), 192.

**Higgins 1996:** Higgins, S.R. and Hamers, R.J, J. Vac. Sci. Technol. B14. (1996),1360 .

**Hofler et al. 1993:** Hofler, H.J. et al, Mater Sci.Eng. A116(1993), p.169-177.

**Hofler 1993:** Hofler, H.J., Averback, R.S., Hahn, H. and Gleiter, H. (1993) J.Appl. Phys., 74, 3832-3839.

**Horita et al. 1996:** Horita et al , J.Mater.Res, 11(1996), 1880.

**Ingvarsson 2002:** Ingvarsson, S. et al., J.Magn.Magn.Mater., 251(2002), 202-206.

**Inoue et al 1994:** Inoue, A. Nakazato, N., Kawamura, Y. and Masumoto, T., Mater.Sci. & Eng. A, (1994) A179/180,654.

**Ishihara 1999:** Ishihara, K.N., 'Thermodynamics and Kinetics of Metastable phase formation' in "Non-Equilibrium Processing of Materials", Pergamon, (1999), Ed.C.Suryanarayana, p.5-18.

**Jo and Yoon 1989**: Jo, K.H. and Yoon, K.H., Mater. Res. Bullet., 24(1989), 1.

**Jung 1999:** Jung, K.B. et al, Appl.Surf.Sci., 138-139(1999), 111-116.

**Karimpoor et al. 2002:** Karimpoor, A.A., Erb, U., Aust, K.T., Wang, Z. and Palumbo, G., Mater. Sci. Forum, vol. 386-388(2002), 415-420.

**Kear 1993:** Kear, B.H. and McCandlish, L.E., NanoStructured Mater. , 3(1993), 19.

**Koch 1997:** Koch, C.C., NanoStructured Mater. , 9(1997), 13.

**Kondo 1990:** Kondo, K.I., and Sawai. S, J. Am. Ceram. Soc., 73(1990), 1983.

**Korth and Williamson 1995:** Korth, G.E. and Williamson, R.L., Metall. Mater. Trans., 26A(1995), 2571.

**Krill et al. 1995:** Krill et al., Materials Science Forum, 179-181(1995), 443.

**Krstic 1993:** Krstic, V., Erb, U., and Palumbo, G., Scripta Metall. Mater., 29(1993), 1501.

**Liu 1998:** Liu, X.D., Mater. Trans., JIM, vol.39(1998), No.8, p. 783-784.

**Lu et al 1995:** Lu et al, Acta Metall.Mater. , 43(1995), 2641.

**Lu 1996:** Lu, K., Mater. Sci. Eng., R16(1996), 161.

**Ma 2000:** Ma, E., Powder Metallurgy, vol. 43(2000), no.4, p.306-309.

**Ma and He 1996:** Ma, E. and He, L., J.Mater.Res, vol.11(1996), no.1, p.72-79.

**Ma and He 2000:** Ma, E. and He, L. J.Mater.Res, vol.15(2000), no.4, p.904-911.

**Manual:** Manual for Vibrating Sample Magnetometer, Model 155.

**McCandlish et al. 1994:** McCandlish, L.E., Kevorkian, V., Jia, K. and Fischer, T.E. in "Advances in Powder metallurgy and Particulate Materials-1994", vol.5, compiled by Lall, C. and Neupaver, A.J. (Metal Powder Industries federation, Princeton NJ), (1994), p.329.

**McHenry et al. 2000:** McHenry, M.E. and Laughlin, D.E., Acta Mater. , 48(2000), 223-238.

**Nieh et al. 1991:** Nieh, T.G. and Wadsworth, J., Scr. Metall. Mater., 25(1991), 955-958.

**Nihara 1999:** Nihara, K., J.Ceram.Soc.Japan, 99(1999), 974 .

**Palumbo et al. 1990:** Palumbo, G., Erb, U. and Aust, K.T., Scripta Metall. Mater.,

24(1990), 2347-2350.

**Ping et al. 1995**: Ping, D.H., Li, D.X. and Ye, H.Q., J. Mater. Sci. Lett., 14(1995), 1536.

**Rangnathan et al. 2001**: Ranganathan, S., Divakar, R. and Raghunathan, V.S., Scripta Mater., 44(2001), 1169-1174.

**Roco 2001**: Roco, M.C., J. Nanoparticle Research, 3 (5-6) (2001), pp. 353-360.

**Roco 2002**: Roco, M.C., JOM, September 2002, 22-23.

**Roco et al. 2003**: Roco, M.C., Williams, R.S and Alivisatos, P., (2003) (on website www.nano.gov).

**Rofgha et al. 1991**: Rofgha, R., Langer, R., Ei-Sherik, A.M., Erb, U., Palumbo, G., and Aust, K.T., Scripta. Metall. Mater., 25(1991), 2867.

**Rofgha et al. 1993**: Rofgha, R., Erb, U., Ostrander, D., Palumbo, G. and Aust, K.T., Nanostructured Mater., 2(1993), 1.

**Rosenberg 1968**: Rosenberg, S.J., in "Nickel and Its Alloys", National Bureau of Standards Monograph 106(1968), p. 51-54.

**Roy et al. 1982**: Roy, R.A. and Roy, R., Abstracts, Materials Research Society Annual Meeting, Boston, Massachusetts, (1982), p.37.

**Roy and Roy 1984**: Roy, R.A. and Roy, R., Mater.Res.Bull, 19(1984), 169.

**Sattler et al. 1994**: Sattler, K., Raina, G., Ge, M., Venkteswaran, N., Xhie, J., Liao, Y.X. and Siegel, R.W., J. Appl. Phys., 76(1)(1994), 546-551.

**Schumacher et al. 1989**: Schumacher, S., Birringer, R., Strauss, R. and Gleiter, H., Acta Metall.,37(1989), 2485-2488.

**Shyam Kumar 2002**: Shyam Kumar, M.Tech. Thesis titled "Processing and Properties of Mechanically Alloyed Nanocrystalline Nickel-Iron" submitted to Dept. of MME, I.I.T. Knapur, India, 2002.

**Siegel 1990**: Siegel, R.W., MRS Bulletin, 15(10), (1990), 60.

**Siegel 1993**: Siegel, R.W., Mater.Sc.and Engg. , A168(1993),189-197.

**Siegel 1994**: Siegel, R.W., Nanostruct. Mater., 4(1994), 121.

**Siegel 1992**: Siegel. R.W. and Thomas, G.J., Ultra microscopy, 40(1992), 376.

**Suryanarayana 1995**: Suryanarayana, C., International Mater. Review, 40, 2, (1995), 41-64.

**Suryanarayana 1999**: Suryanarayana, C., 'Mechanical Alloying' in "Non-Equilibrium Processing of Materials", Pergamon, 1999, Editor C.Suryanarayana, p.49-88.

**Suryanarayana 2001**: Suryanarayana, C., Progress in Materials Science, 46(2001), 1-184.

**Suryanarayana and Froes 1989**: Suryanarayana, C. and Froes, F.H. (1989) "Nanocrystalline Metals: A Review", in "Physical Chemistry of Powder Metals Production and Processing", (ed. W.Murray Small), TMS, p.282-285.

**Suryanarayana and Koch 1999**: Suryanarayana, C. and Koch, C.C. 'Nanostructured Materials' in "Non-Equilibrium Processing of Materials", Chapter 12, Pergamon, 1999, editor   C.Suryanarayana.

**Suryanarayana 1997**: Suryanarayana, C., Korth, G.E. and Froes, F.H., Metall. Mater. Trans., 28A(1997), 293.

**Suwa et al 1985**: Suwa, Y., Roy, R. and Komarneni, S., J. Am. Ceram. Soc., 68(1985), C-238 .

**Suwa 1986**: Suwa, Y., Roy, R. and Komarneni, S. (1986) J.Mater. Sci. Lett. 5, 21.

**Suwa et al. 1986**: Suwa, Y., Roy, R. and Komarneni, S. (1986) Mater. Sci. Engg. 83,

151.

**Swygenhoven 2001:** Swygenhoven, H.V.,Caro, A. and Farkas, D., Scripta Mater., 44(2001), 1513-1516.

**Tiers 1996:** Tiers, J.F.,'Example Applications', in "The iron-nickel alloys", (eds. G.Beranger et al.), 1996, Lavoisier, NY, p.289.

**Voorthuysen 2002:** Voorthuysen, E.H.M. et al (2002), J.Magn.Magn.Mater, "in press" available at www.sciencedirect.com.

**Wakai et al. 1986:** Wakai, K., Sakaguchi, S. and Matsumo,Y., Adv.Ceram.Mater., 1(1986), 259.

**Wiesendanger 1994:** Wiesendanger, R., Scanning Probe Microscopy and Spectroscopy: Methods and Applications, (1994), Cambridge University Press, Cambridge,U.K.

**Williamson and Berry 1986:** Williamson, R.L. and Berry, R.A., in Shock Waves in Condensed Matter, editor Y.M. Gupta, Plenum, New York, NY, 1986, pp. 341-346.

**Wunderlich et al. (1990):** Wunderlich, W., Ishida, Y. and Maurer, R., Scripta Metall. Mater., vol. 24(1990), 403-408.

**Yoshizawa, Y. 2001:** Yoshizawa, Y., Scripta. Mater., 44(2001), 1321-1325.

**Yoshizawa et al. 1988:** Yoshizawa, Y., Oguma, S. and Yamauchi, K.J., J. Appl. Phys., 64(1988), 6044.

**Liu 1998:** Liu, Xue-Dong, Mat. Trans., JIM, 1998, vol.39, no.8, p.783-784.

**Yulin and Liaw 2001:** Yulin Lu and Peter K. Liaw, JOM, March (2001), 31-35.

**Zhou et al. 2002:** Zhou, B., Zhang, Y.W., Liao, C.S. and Yan, C.H., J. Magn. Magn. Mater., 247(2002), 70-76.

**Table 1: Intensity, Interplaner Spacing and khl values of various oxides**

| Oxide | Intensity of Peak, I | Interplaner Spacing, $dA^0$ | hkl |
|---|---|---|---|
| NiO | 100 | 2.10 | 012 |
| | 60 | 2.41 | 101 |
| | 35 | 1.48 | 104 |
| $Ni_2O_3$ | 100 | 2.80 | 002 |
| | 100 | 1.77 | 112 |
| | 100 | 1.62 | 202 |
| CoO | 100 | 2.13 | 200 |
| | 75 | 2.46 | 111 |
| | 50 | 1.51 | 220 |
| $Co_2O_3$ | 100 | 2.87 | 002 |
| | 100 | 2.33 | 110 |
| | 100 | 1.78 | 112 |
| $Co_3O_4$ | 100 | 2.44 | 311 |
| | 45 | 1.43 | 440 |
| | 40 | 2.86 | 220 |
| FeO | 100 | 1.52 | 104 |
| | 100 | 1.51 | 110 |
| | 100 | 0.96 | 116 |
| $Fe_2O_3$ | 100 | 2.52 | 311 |
| | 53 | 1.48 | 220 |
| | 34 | 2.95 | 440 |
| $Fe_3O_4$ | 100 | 2.53 | 311 |
| | 85 | 1.61 | 333 |
| | 85 | 1.48 | 440 |

A 145115

A145115